

Role of noncollective excitations in low-energy heavy-ion fusion reaction and quasi-elastic scattering

Department of Physics, Faculty of Science, Tohoku university

Shusaku Yusa

December 28, 2012

Contents

1	Introduction	3
2	Nuclear excitations	10
2.1	Collective excitations	10
2.2	Noncollective excitations	16
3	Coupled-channels method	19
3.1	Coupled-channels equations	19
3.2	Iso-centrifugal approximation	21
3.3	Sudden tunneling limit	24
3.4	Barrier distribution method	26
3.5	Constant coupling approximation	30
3.6	Coupling to collective states	30
3.6.1	Vibrational coupling	30
3.6.2	Rotational coupling	35
3.6.3	Adiabatic potential renormalization	37
3.7	Full order coupling	39
4	Random matrix theory	41
4.1	Introduction	41
4.2	Gaussian orthogonal ensemble(GOE)	42
4.3	Properties of GOE	43
4.4	Fluctuation measures of GOE	44
4.5	Random matrix theory for deep inelastic collision	46
5	Noncollective excitations in $^{16}\text{O} + ^{208}\text{Pb}$ reaction	49
5.1	Current status of $^{16}\text{O} + ^{208}\text{Pb}$ reaction	49
5.2	Results	51
5.2.1	Single phonon calculation	51
5.2.2	Double phonon calculation	54
5.2.3	Anharmonicity of octupole phonon state in ^{208}Pb	54

5.2.4	Q-value distribution	57
5.2.5	Mass-number dependence of the effect of noncollective excitations	57
6	Noncollective excitations in $^{20}\text{Ne} + ^{90,92}\text{Zr}$ reaction	61
6.1	Quasi-elastic scattering for $^{20}\text{Ne} + ^{90,92}\text{Zr}$ systems	61
6.2	Random matrix model	62
6.3	Level density and strength distribution	64
6.4	Test of random matrix model with $^{16}\text{O} + ^{208}\text{Pb}$ reaction	66
6.5	Application to $^{20}\text{Ne} + ^{90,92}\text{Zr}$ systems	66
6.5.1	Parameters	66
6.5.2	Results	69
6.6	Prediction for $^{24}\text{Mg} + ^{90,92}\text{Zr}$ reaction	78
7	Summary and concluding remarks	81
A	Classical expression for fusion cross section and the Wong formula	86
B	Role of noncollective excitations in one-dimensional barrier penetration problem	90
B.1	Random matrix model for one-dimensional coupled-channels equations	90
B.2	Results	91
C	Calculation of gaussian orthogonal ensemble(GOE)	95
D	Interplay of collective and noncollective excitations	97

Chapter 1

Introduction

Nuclear reactions show a variety of behaviors depending on the colliding energy and species of the colliding nuclei. For heavy-ion reactions, a cancellation of an attractive nuclear potential and the repulsive Coulomb potential makes a potential barrier called the Coulomb barrier. In Fig. 1.1, we show an example of the potential for $^{20}\text{Ne} + ^{90}\text{Zr}$ system. In heavy-ion reactions around the Coulomb barrier energy, a quantum tunneling effect is important for discussing the barrier penetration and thus the fusion process. Since a nucleus is a composite system, the internuclear potential can be modified due to the internal excitations of the colliding nuclei, and the fusion probability can be changed. Therefore, heavy-ion reactions around the Coulomb barrier provides us with a good opportunity to investigate an interplay between the reaction process and internal excitations in the colliding nuclei. These internal excitations can be considered as environmental degrees of freedom for the relative motion of the reaction. Thus, low-energy heavy-ion reaction gives an example of the quantum tunneling in the presence of the external environment. The effects of the external environment on a quantum tunneling process was studied in detail by Caldeira and Leggett[1, 2]. They considered a system coupled to a number of harmonic oscillators which act as the environment, and discussed the effect of the energy dissipation to the environmental degrees of freedom on the quantum tunneling rate. In low-energy heavy-ion reactions, a well known example of the coupling effect is the enhancement of subbarrier fusion cross sections, compared to a prediction of a simple potential model[3, 4].

In order to take into account such a coupling effect in the description of low-energy heavy-ion reactions, a coupled-channels method has been employed. This method expresses the wave function as a superposition of various channel wave functions, and is employed not only in nuclear physics but also in quantum chemistry to describe the multi-dimensional tunneling phenomena. In coupled-channels calculations, conventionally, a few low-lying collective excitations of the colliding nuclei, such as a vibrational mode in spherical nuclei or rotational excitations in deformed nuclei, as well as few nucleon-transfer channels have been taken into account. This is because, among the internal excited states, these collective states strongly couple to the relative motion and play an important role. The coupled-channels analyses have been successfully accounted for exper-

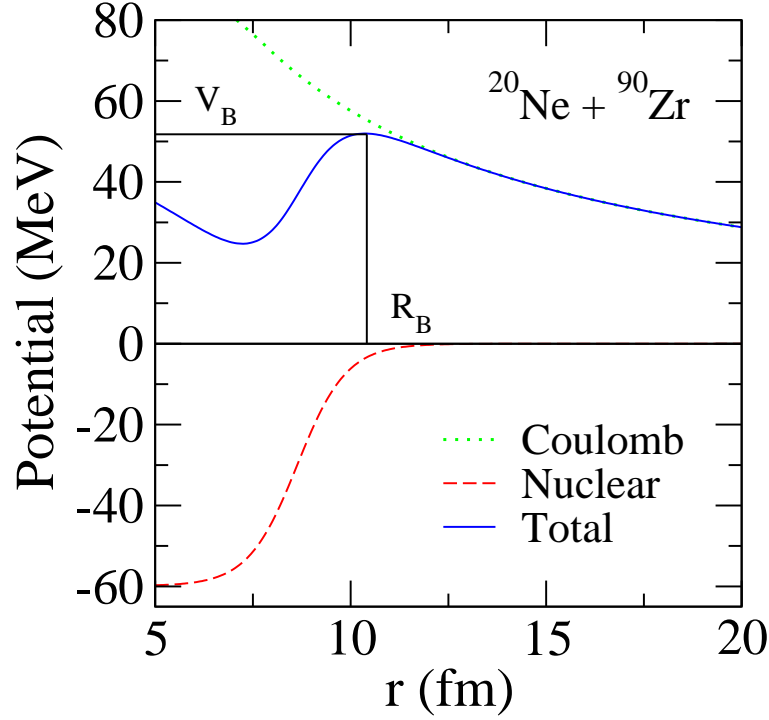


Figure 1.1: The internuclear potential between ^{20}Ne and ^{90}Zr nuclei. The green dotted line and the red dashed line show the Coulomb and the nuclear potentials, respectively. The solid blue line is the total(Coulomb + nuclear) potential. R_B and V_B are the position and the height of the Coulomb barrier, respectively.

imental data for heavy-ion fusion reactions as well as quasi-elastic scattering (a sum of elastic and inelastic scattering and transfer reactions) at backward angles[3]. These two reaction processes are complementary to each other from the point of view of the tunneling of the potential barrier. That is, the fusion process corresponds to the penetration of the barrier, while the backward scattering corresponds to the reflection from the barrier.

In the eigenchannel representation, the channel-coupling effects lead to a distribution of potential barriers[5]. It has been well established that the barrier distribution can be directly extracted from experimental fusion and quasi-elastic cross sections. For fusion reactions, the barrier distribution is defined as the second derivative of the product of center-of-mass energy $E_{c.m.}$ and the fusion cross section σ_{fus} with respect to $E_{c.m.}$, that is, $d^2(E_{c.m}\sigma_{fus})/dE_{c.m.}^2$ [4, 6]. For quasi-elastic scattering, the barrier distribution is defined as the first derivative of the ratio of the quasi-elastic cross section to the Rutherford cross section with respect to the center-of-mass energy at backward angle, that is, $-d(\sigma_{qel}(\theta = \pi)/\sigma_R(\theta = \pi))/dE_{c.m.}$ [7, 8]. It has been well recognized that the fusion and quasi-elastic barrier distributions behave in a similar way, while the quasi-elastic barrier distribution tends to be more smeared[7, 9, 10]. These quantities are known to be considerably sensitive to the channel-coupling effects[3, 4, 11]. They can also serve for the determination of deformation parameters[12].

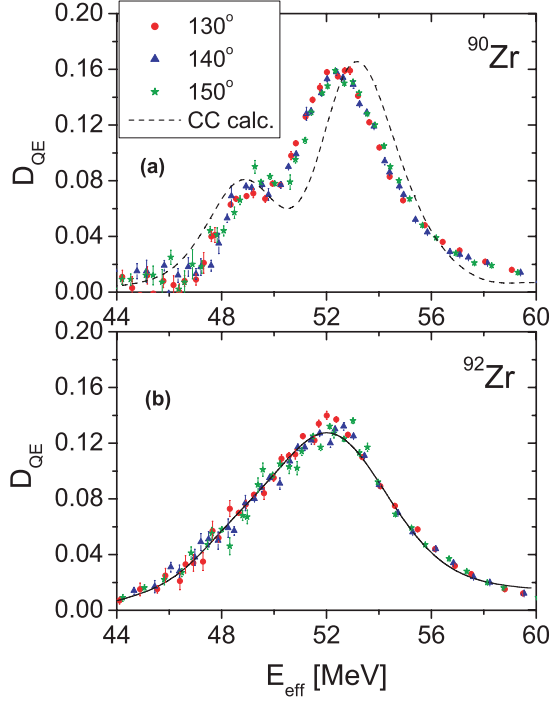


Figure 1.2: Extracted quasi-elastic barrier distribution for $^{20}\text{Ne} + ^{90,92}\text{Zr}$ systems at three scattering angles. The dashed line in Fig. 1.2(a) shows the result of the coupled-channels calculation. The solid line in Fig. 1.2(b) is obtained by smearing the data for $^{20}\text{Ne} + ^{90}\text{Zr}$ system. The figure is taken from Ref.[19].

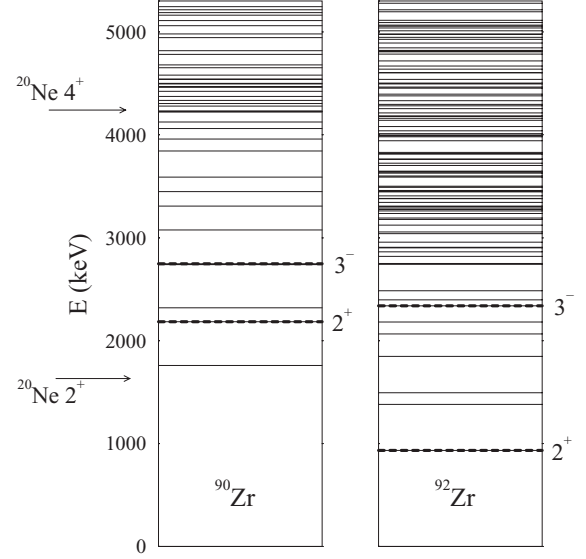


Figure 1.3: Energy spectra for Zr isotopes. The dashed lines represent the collective excitations which are taken into account in the coupled-channels calculation shown in Fig. 1.2. The rotational states of ^{20}Ne are also shown. Taken from Ref. [19].

Although the coupled-channels method has been successfully accounted for various experimental data for heavy-ion fusion reactions, as well as quasi-elastic scattering, there is a long-standing problem of the approach, that is, in order to reproduce experimental fusion data, a significantly larger value of the surface diffuseness of the nuclear potential is required, compared to the value found from fitting to the scattering process[13, 14]. It has been also a long-standing problem that the coupled-channels calculation has not been able to simultaneously reproduce the fusion and quasi-elastic barrier distributions for $^{16}\text{O} + ^{144}\text{Sm}$ system[10].

Furthermore, several recently obtained data cannot be accounted for by the conventional coupled-channels calculations. For example, fusion cross sections at deep subbarrier energies are strongly suppressed, compared to the prediction of the coupled-channels calculations[15, 16, 17, 18]. Another example is the quasi-elastic scattering experiment for $^{20}\text{Ne} + ^{90,92}\text{Zr}$ systems[19]. In this experiment, the quasi-elastic barrier distributions were obtained from measured quasi-elastic cross sections and were analyzed by the coupled-channels calculation. This is shown in Fig. 1.2, which is taken from Ref. [19]. The dots represent the experimental data at three different scattering angles

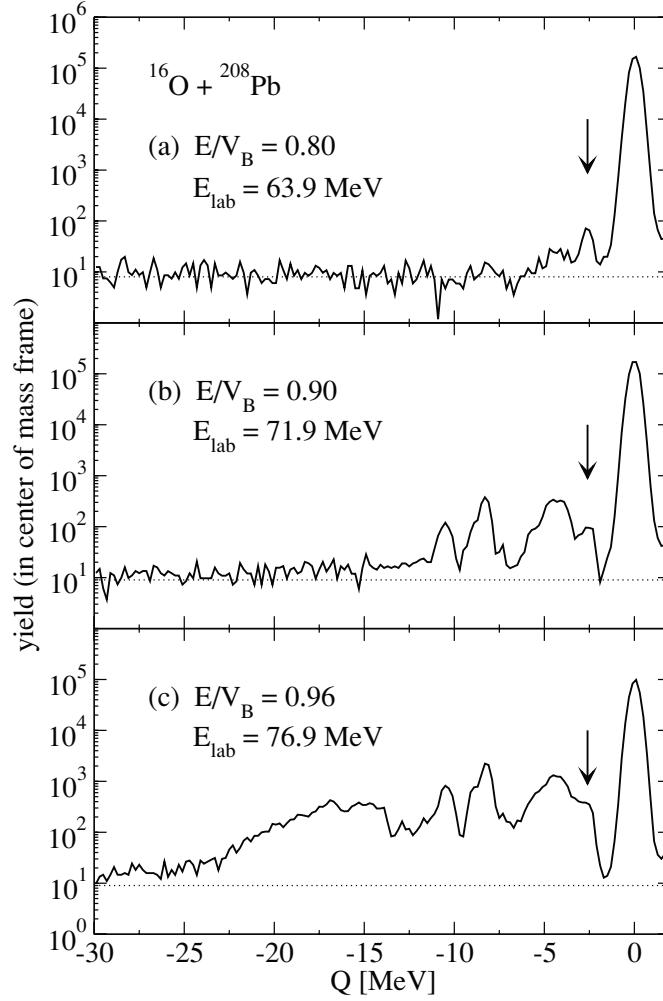


Figure 1.4: Experimental Q-value distribution for $^{16}\text{O} + ^{208}\text{Pb}$ system at three subbarrier energies. The figure is taken from Ref. [25]. The peak indicated by the arrow represents the octupole phonon excitation of ^{208}Pb .

and the dashed line in the upper figure represents the results of the coupled-channels calculation. The difference in the scattering angles of the data is compensated by modifying the CM energy $E_{\text{c.m.}}$ to E_{eff} , which takes into account the effect of the centrifugal potential (see Eq. (3.47)). As one can see, the experimentally obtained barrier distribution behaves in a significantly different way between the two systems, that is, the barrier distribution for $^{20}\text{Ne} + ^{92}\text{Zr}$ is much more smeared than that for $^{20}\text{Ne} + ^{90}\text{Zr}$ system. However, the coupled-channels calculation which takes into account the rotational excitations of ^{20}Ne and the collective vibrational excitations of $^{90,92}\text{Zr}$ yields similar barrier distributions, because the largely deformed ^{20}Ne dominantly determines the barrier structure, while the difference in the vibrational excitations in $^{90,92}\text{Zr}$ plays only a minor role. One of the possible reasons for this problem is the effect of the transfer reactions[20, 21]. However, for these systems, the total transfer cross sections have been found to be almost the same[19]. Therefore, the difference in the barrier distributions has been conjectured to arise from noncollective excitations which are not explicitly taken into account in the coupled-channels analysis. In Fig. 1.3, we show

the energy spectra of $^{90,92}\text{Zr}$ nuclei. Since the ^{90}Zr is a closed shell nucleus with 50 neutrons and ^{92}Zr has two additional neutrons, the number of relatively low-lying noncollective states in ^{92}Zr is much larger than that in ^{90}Zr . In fact, while there are only 12 states in the ^{90}Zr nucleus up to 4 MeV, there are 53 known states in ^{92}Zr nucleus[22]. For 5 MeV, the number of known states is 35 and 87 for ^{90}Zr and ^{92}Zr , respectively. Although the excitation to each noncollective state is weak compared to that to a collective state, excitations to a large number of noncollective states may alter the barrier structure.

Indication of the importance of the noncollective excitations can be seen in the quasi-scattering experiments for $^{16}\text{O} + ^{208}\text{Pb}$ system[23, 24, 25, 26, 27]. In the experiments, the Q-value distribution was measured at several different energies. The experimental data are shown in Fig. 1.4, which is taken from Ref. [25]. V_B in the figure represents the height of the Coulomb barrier. The horizontal axis represents the Q-value, that is, the loss of kinetic energy due to the internal excitations of the colliding nuclei. Thus, the peak at $Q = 0$ represents the elastic scattering and the contribution from a negative Q-value represents the inelastic scattering. The arrow in the figure indicates the peak for the first 3^- state in ^{208}Pb which is considered to be a collective state. The distribution at larger Q-value can be considered as the contribution from the noncollective excited states, since in such a high excitation energy region, a large number of noncollective excited states exist in the energy spectrum of ^{208}Pb . While the elastic scattering is dominant at the lowest incident energy, the experimental data indicate that the contribution from the noncollective excitations increases as the incident energy increases. For this system, precise fusion cross sections were measured around the Coulomb barrier energy, and a careful coupled-channels analysis has been performed[28, 29] by including the collective vibrational excitations in ^{208}Pb and a few transfer channels. Since both ^{16}O and ^{208}Pb are double closed shell nuclei, one may think that it is a straightforward task to reproduce the experimental data. However, the coupled-channels calculation overestimates the height of the main peak of the fusion barrier distribution, even if all the relevant collective excitations are taken into account. This fact shows that one has to take into account the effects which are not taken into account in the conventional coupled-channels calculation, such as noncollective excitations.

The aim of this thesis is thus to investigate the role of noncollective excitations in low-energy heavy-ion fusion reactions and quasi-elastic scattering. In the conventional coupled-channels calculations, the effect of noncollective excitations is implicitly taken into account through the optical potential. However, the distribution of eigenbarriers is not altered in this treatment. Thus, by including the noncollective excitations into the coupled-channels method in an explicit way, we discuss the role of noncollective excitations in barrier distributions and Q-value distributions.

The thesis is organized as follows. In chapter 2, a fundamental feature of nuclear excited states is reviewed. Especially, low-lying collective excited states are reviewed in detail based on the liquid drop model. We also mention an interpretation of the collective and the noncollective excited states from a microscopic point of view.

In chapter 3, the theoretical framework for the description of heavy-ion reaction is reviewed. The coupled-channels method is employed throughout this work. After the derivation of the coupled-channels equations in the full angular coupling formalism, the isocentrifugal approximation is introduced to reduce the number of channels in the calculation[30, 31, 32, 33, 34, 35, 36, 37, 38, 39]. A sudden tunneling limit is discussed and the eigenchannel formalism is presented. The barrier distribution method is then introduced both for fusion reaction and quasi-elastic scattering. The constant coupling approximation is also discussed[5]. The effect of collective excitations on subbarrier fusion cross sections and the barrier distribution is presented through typical calculations for the vibrational coupling and the rotational coupling. The effect of high-lying collective states is also discussed. Inclusion of high-lying states does not significantly alter the shape of the barrier distribution but produces an adiabatic potential renormalization[40]. At the end of chapter 3, the computational method of the coupling matrix elements in the full order coupling is presented[41].

In order to take into account the coupling to noncollective states in the coupled-channels calculation, one needs to know the transition strength to those states. For some nuclei, such information is experimentally obtained. For example, almost all of the excited states of ^{208}Pb up to 7 MeV have been identified (the spin, parity, excitation energy, and deformation parameter) from high precision proton inelastic scattering experiments[42, 43]. However, in general, such information is not necessarily available. For such systems, one has to resort to a theoretical or phenomenological model to estimate the transition strength to the noncollective states. For this purpose, a model for heavy-ion reactions based on the random matrix theory is employed in this work. This model was originally introduced for the study of heavy-ion deep inelastic collisions in the 1970's by Weidenmüller and his collaborators[44, 45, 46, 47, 48, 49, 50]. Chapter 4 is devoted to the random matrix theory, which is the basis of this model. Fundamental feature of this theory and the relation to the nuclear spectrum is reviewed.

As mentioned above, the information on the noncollective excited states is obtained for ^{208}Pb nucleus from high precision proton inelastic scattering experiments. Using this information, in chapter 5, we investigate the role of the noncollective excitations of ^{208}Pb in the reaction of $^{16}\text{O} + ^{208}\text{Pb}$ system[51]. Since the coupled-channels calculation has not successfully reproduced the fusion barrier distribution for this system[28], we shall see whether the noncollective excitations can improve the agreement of the coupled-channels calculation with the experimental data. Together with the noncollective excitations, the effect of anharmonicity is also investigated, as the first excited state of ^{208}Pb , which is the octupole phonon state at 2.615 MeV, has been found to have a finite quadrupole moment[52, 53, 54]. The energy dependence of the Q-value distribution is also investigated including the noncollective excitations. Although the agreement of the calculation with the experimental data is not improved for the fusion barrier distribution, the energy dependence of the calculated Q-value distribution agrees with that of the experimental Q-value distribution in a qualitative way. At the end of this chapter, we investigate the dependence of the

effect of the noncollective excitations on the mass number of the projectile nucleus. We show the fusion calculations for $^{32}\text{S} + ^{208}\text{Pb}$ and $^{40}\text{Ca} + ^{208}\text{Pb}$ systems and show that the noncollective effect increases as the mass number of the projectile increases.

In chapter 6, we investigate the role of noncollective excitations in $^{20}\text{Ne} + ^{90,92}\text{Zr}$ systems. For $^{90,92}\text{Zr}$ nuclei, the information on the noncollective excited states is not sufficiently obtained in contrast to ^{208}Pb nucleus. Thus, one cannot use the same approach as in the calculation for $^{16}\text{O} + ^{208}\text{Pb}$ reaction to describe the coupling to the noncollective excited states. Therefore, we employ the random matrix model for the description of the noncollective excitations. To see the applicability of the random matrix model, we first apply the model to $^{16}\text{O} + ^{208}\text{Pb}$ reaction, and compare with the more reliable calculation which uses the experimentally obtained information on the noncollective states of ^{208}Pb . The obtained results show that the random matrix model can reproduce the results based on the experimental information. We then apply the model to the $^{20}\text{Ne} + ^{90,92}\text{Zr}$ systems. Using the same parameters in the random matrix model between the two systems, we show that the noncollective excitations smear the peak structure of the quasi-elastic barrier distribution for $^{20}\text{Ne} + ^{92}\text{Zr}$ system leading to a much better agreement with the data. On the other hand, for $^{20}\text{Ne} + ^{90}\text{Zr}$ system, the noncollective excitations do not change the structure of the barrier distribution in a significant way and the agreement with the data is not destroyed by the noncollective excitations. This difference between the two systems comes from the difference in the spectra of $^{90,92}\text{Zr}$ nuclei, thus we successfully achieve the simultaneous description of the quasi-elastic barrier distributions for the $^{20}\text{Ne} + ^{90,92}\text{Zr}$ systems. We also apply the random matrix model to other systems which use ^{90}Zr or ^{92}Zr as a target, and verify that the inclusion of the noncollective excitations of $^{90,92}\text{Zr}$ does not lead to an inconsistency with the experimental data for these systems. At the end of this chapter, we apply the model to $^{24}\text{Mg} + ^{90,92}\text{Zr}$ systems. Since the ^{24}Mg is a prolately deformed nucleus with a large deformation parameter, one can expect that the barrier distribution for the $^{24}\text{Mg} + ^{90,92}\text{Zr}$ systems exhibits a behavior similar to the $^{20}\text{Ne} + ^{90,92}\text{Zr}$ systems. Our results show that this is the case.

Finally the summary of the thesis is given in chapter 7.

Chapter 2

Nuclear excitations

In this chapter, a fundamental feature of nuclear excited states is reviewed. One can classify the nuclear excitations into two classes, that is, collective excitations and noncollective excitations. Properties and differences of these two kinds of excitations are presented.

2.1 Collective excitations

Collective excitations are understood as a collective motion of nucleons composing a nucleus. There are two kinds of collective excitations, that is, low-lying collective excitations and giant resonances. In this section, we review the low-lying collective excitations since they play an important role in the low-energy heavy-ion reactions. On the other hand, the giant resonances appear in the energy region of ten to several tens of MeV as a broad resonance. The effect of these high-lying excited states can be compensated by renormalizing the potential, which will be discussed in the next chapter.

The most remarkable feature of the collective excitations is a large electromagnetic transition strength, compared to a single-particle excitation. Let us consider an electric quadrupole transition from a state with spin $I + 2$ to a state with spin I (E2 transition). The transition probability is given by[55]

$$T = \frac{4\pi}{75} \frac{1}{\hbar} \left(\frac{E_\gamma}{\hbar c} \right)^5 B(E2, I + 2 \rightarrow I). \quad (2.1)$$

Here, $E_\gamma = E_i - E_f$ is the energy difference of the initial and the final states and $B(E2, I + 2 \rightarrow I)$ is called the reduced transition probability. In general, for a transition from a state $|i\rangle$ with spin I_i to a state $|f\rangle$ with spin I_f , the reduced transition probability is given by

$$B(E\lambda, I_i \rightarrow I_f) = \frac{1}{2I_i + 1} |\langle f || Q_\lambda || i \rangle|^2, \quad (2.2)$$

where, Q_λ is an electric multipole operator with a multipolarity λ (the E2 transition corresponds to $\lambda = 2$). In order to evaluate the magnitude of $B(E\lambda)$ -values, the Weisskopf unit is often used[56]

which is give by

$$B_W(E\lambda) = \frac{e^2}{4\pi} \left(\frac{3}{\lambda + 3} \right)^2 R^{2\lambda}, \quad (2.3)$$

where $R = 1.2A^{1/3}$ (fm) is the radius of the nucleus. This formula is obtained by assuming a transition of a nucleon between single-particle levels and a constant nucleon wave function extending inside the radius of R . Thus the comparison with this value provides an idea on how collective the state is. If one considers a transition from a 2^+ state to a 0^+ state, then the reduced transition probability is given by

$$B_W(E2) = \frac{e^2}{4\pi} \left(\frac{3}{5} \right)^2 R^4 = 30A^{4/3} e^2 \text{fm}^4. \quad (2.4)$$

Experimentally obtained $B(E2)$ values from the first 2^+ state to the ground state are plotted in Fig.2.1 for various even-even nuclei in the Weisskopf unit[57]. One can notice that all the values are greater than one, and quite large for nuclei in the region of $140 \lesssim A \lesssim 180$ and $A \gtrsim 230$. Nuclei in these region are known to be deformed, and thus the first 2^+ state is a rotational state. Reflecting the collective character of these states, the transition probabilities have a large value.

A characteristic feature of the collective states is also found from their appearance in nuclear spectrum. Typical nuclear spectra for vibrational and rotational levels are shown in Figs. 2.2 and 2.3, respectively. In Fig.2.2, the first 2^+ state and the triplet states of $0^+, 2^+, 4^+$ appear in ^{106}Pd and ^{114}Cd in nearly equi-distance. In Fig.2.3, states with even spin ($I = 0, 2, 4, \dots$) regularly appear according to the $E_I \propto I(I + 1)$ law. In the following, we explain how the regularity of these states arises from the vibrational or rotational properties of the nuclei.

Let us first consider a surface vibration of even-even spherical nuclei in a liquid drop model[55]. One can expand the distance $R(\theta, \phi)$ from the center-of-mass of the nucleus to a surface point at angle (θ, ϕ) direction by spherical harmonics as

$$R(\theta, \phi) = R_0 \left\{ 1 + \sum_{\lambda, \mu} \alpha_{\lambda\mu}^* Y_{\lambda\mu}(\theta, \phi) \right\}, \quad (2.5)$$

where $\alpha_{\lambda\mu}$ is the expansion coefficient. In the liquid drop model, the surface vibration is described by regarding the expansion coefficients $\alpha_{\lambda\mu}$ as dynamical variables. The Hamiltonian for this model is given by

$$H = \sum_{\lambda, \mu} \left(\frac{1}{2} B_\lambda |\dot{\alpha}_{\lambda\mu}|^2 + \frac{1}{2} C_\lambda |\alpha_{\lambda\mu}|^2 \right). \quad (2.6)$$

Here, the dot means the differentiation with respect to time. The first term represents the kinetic energy of the vibrational motion and the second term represents the potential energy associated with the deviation of the nuclear shape from sphere. Since this is a Hamiltonian for a harmonic

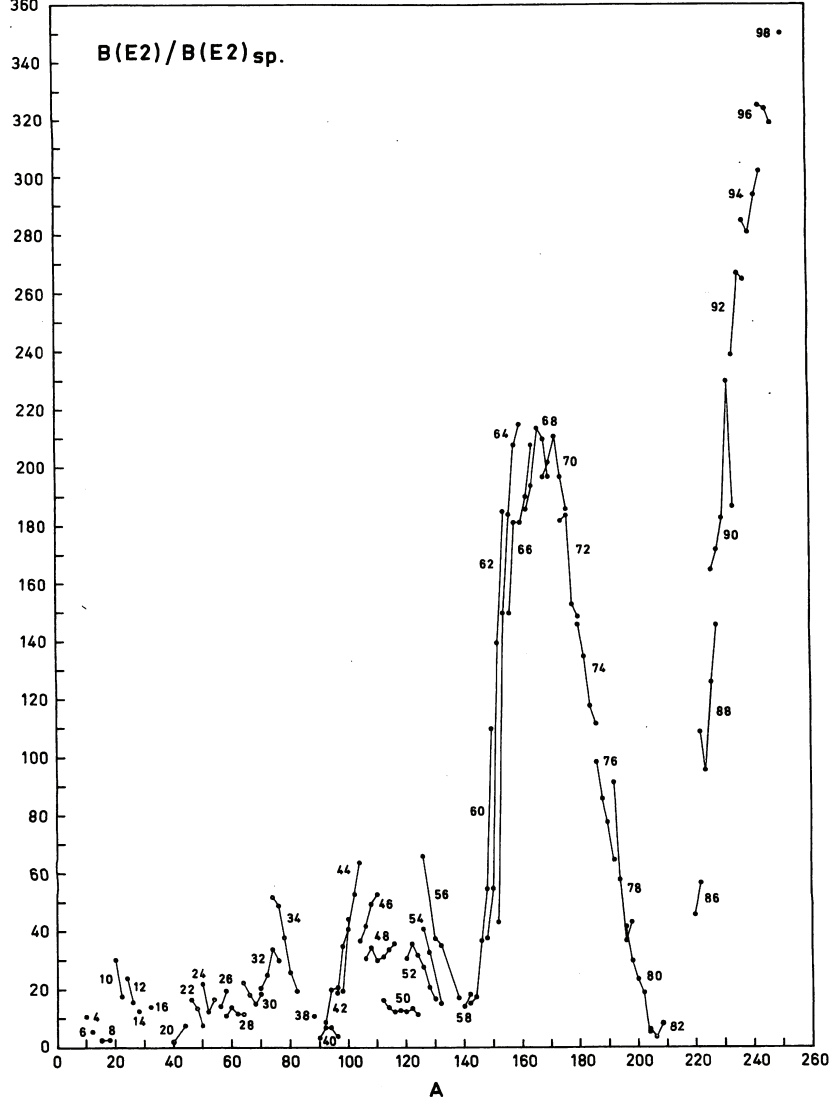


Figure 2.1: $B(E2)$ value for various even-even nuclei. The $B(E2)$ values are measured in the Weisskopf unit. Taken from Ref. [57].

oscillator, it can be quantized in the usual manner and reads

$$H = \sum_{\lambda, \mu} \frac{1}{2} \hbar \omega_{\lambda} \left(b_{\lambda\mu}^{\dagger} b_{\lambda\mu} + \frac{1}{2} \right), \quad (2.7)$$

where $\omega_{\lambda} = \sqrt{C_{\lambda}/B_{\lambda}}$ and $b_{\lambda\mu}^{\dagger}$ and $b_{\lambda\mu}$ are the creation and annihilation operators of a phonon with angular momentum λ, μ . They satisfy the following commutation relations

$$[b_{\lambda\mu}, b_{\lambda'\mu'}^{\dagger}] = \delta_{\lambda\lambda'} \delta_{\mu\mu'}, \quad (2.8)$$

$$[b_{\lambda\mu}, b_{\lambda'\mu'}] = 0, \quad (2.9)$$

$$[b_{\lambda\mu}^{\dagger}, b_{\lambda'\mu'}^{\dagger}] = 0. \quad (2.10)$$

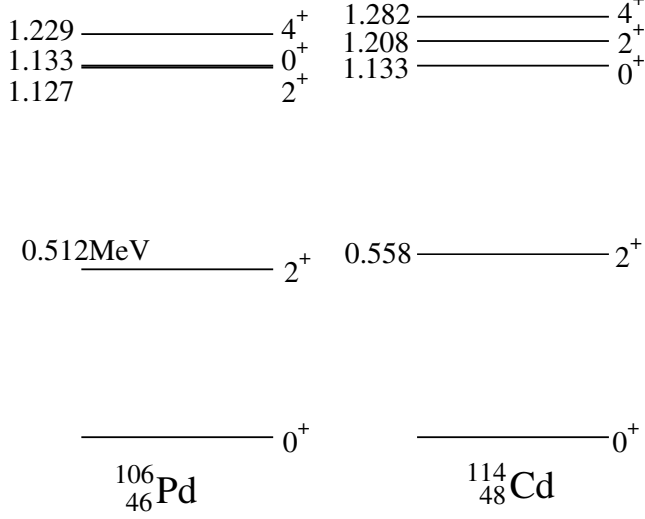


Figure 2.2: Vibrational levels.

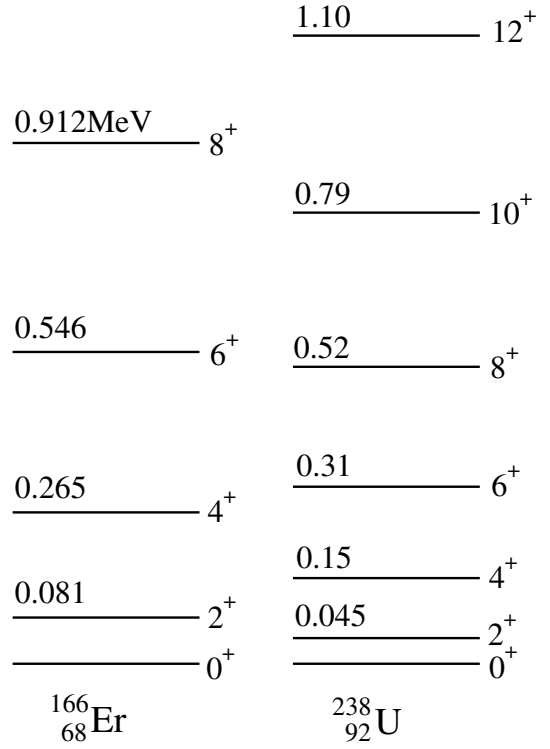


Figure 2.3: Rotational levels.

The first excited state is obtained by creating a phonon in the vacuum $|0\rangle$

$$b_{\lambda\mu}^\dagger |0\rangle. \quad (2.11)$$

The energy of this state is $\hbar\omega_\lambda$ and the spin and the parity are given by λ and $(-1)^\lambda$, respectively. For $\lambda = 2$, the spin-parity of the first excited state is 2^+ for even-even nuclei, in which the ground state has 0^+ . The second excited states are then obtained by creating a phonon on the first excited state. Again, let us consider the case of $\lambda = 2$. The second excited state with angular momentum I, M is given by

$$\frac{1}{\sqrt{2}} \sum_{\mu_1, \mu_2} \langle 2\mu_1 2\mu_2 | IM \rangle b_{2\mu_1}^\dagger b_{2\mu_2}^\dagger |0\rangle. \quad (2.12)$$

From (2.10) and a property of Clebsch-Gordan coefficients

$$\langle 2\mu_1 2\mu_2 | IM \rangle = (-1)^{-I} \langle 2\mu_2 2\mu_1 | IM \rangle, \quad (2.13)$$

one can show that only the states with $I = 0, 2, 4$ are realizable and all of the three states are degenerated with the energy $2\hbar\omega_2$. From this consideration, the excited states shown in Fig.2.2 are understood as the quadrupole phonon states, while the triplet of the double phonon states are split up a little. This split of the spectra indicates the deviation from a pure harmonic oscillator.

In the collective model, one can relate the $B(E\lambda)$ to the deformation parameter. As we will see

in Sec. 3.6.1, the electric multipole operator is calculated as

$$Q_{\lambda\mu} = \frac{3Ze}{4\pi} R^\lambda \alpha_{\lambda\mu} \quad (2.14)$$

for a sharp-cut density and $\alpha_{\lambda\mu}$ is related to the deformation parameter β_λ as

$$\alpha_{\lambda\mu} = \frac{\beta_\lambda}{\sqrt{2\lambda+1}} \left(b_{\lambda\mu}^\dagger + (-1)^\mu b_{\lambda\mu} \right). \quad (2.15)$$

The reduced transition probability from $I_i = 0$ to $I_f = \lambda$ then becomes

$$\begin{aligned} B(E\lambda, 0 \rightarrow \lambda) &= |\langle \lambda || Q_\lambda || 0 \rangle|^2 \\ &= (2\lambda+1) |\langle \lambda 0 | Q_{\lambda 0} | 0 0 \rangle|^2 \\ &= \left(\frac{3e}{4\pi} Z R^\lambda \beta_\lambda \right)^2. \end{aligned} \quad (2.16)$$

Thus, one can estimate the deformation parameter from the $B(E\lambda)$, and vice versa.

Next, let us consider a nucleus whose ground state is deformed. Since the quadrupole ($\lambda = 2$) degree of freedom is the most important in many cases, we consider the quadrupole deformation. Instead of using the original variables $\alpha_{\lambda\mu}$, it is possible to choose the three Euler angles Ω and variables $a_{\lambda\mu}$ defined in the body-fixed frame by

$$a_{\lambda\mu} = \sum_{\mu'} D_{\mu\mu'}^\lambda(\Omega) \alpha_{\lambda\mu'}. \quad (2.17)$$

as independent variables. Here, $D_{\mu\mu'}^\lambda$ is the Wigner's D-matrix. Among five $a_{2\mu}$, one can adopt a_{20} and a_{22} as the independent variables by setting the coordinate axes to coincide with the principal axes of the deformed nucleus. Using a_{20} and a_{22} , the potential energy is given by

$$V(a_{20}, a_{22}) = \frac{1}{2} C_{20} (a_{20} - a_{20}^0)^2 + C_{22} (a_{22} - a_{22}^0)^2. \quad (2.18)$$

This means that the potential energy is minimum at the finite deformation parameters a_{20}^0 and a_{22}^0 . Instead of using a_{20}^0 and a_{22}^0 , it is a convention to use β and γ defined by

$$a_{20} = \beta \cos \gamma \quad (2.19)$$

$$a_{22} = \frac{1}{\sqrt{2}} \beta \sin \gamma. \quad (2.20)$$

Using these variables, the kinetic term of the Hamiltonian is written as

$$T = T_{\text{rot}} + T_{\text{vib}} \quad (2.21)$$

$$T_{\text{rot}} = \frac{1}{2} \sum_{k=1}^3 \mathcal{J}_k \omega_k^2 \quad (2.22)$$

$$T_{\text{vib}} = \frac{1}{2} B_2 (\dot{\beta}^2 + \beta^2 \dot{\gamma}^2). \quad (2.23)$$

Here, \mathcal{J}_k is the moment of inertia and is given by

$$\mathcal{J}_k(\beta, \gamma) = 4B_2\beta^2 \sin^2\left(\gamma - \frac{2\pi}{3}k\right). \quad (2.24)$$

ω_k is the angular velocity and is given by the time derivative of the Euler angles. T_{rot} and T_{vib} describe the rotational and the vibrational motions, respectively, and they are coupled through \mathcal{J}_k with each other. Using the angular momentum operators around the body-fixed axes $\hat{I}_k (k = 1, 2, 3)$, the quantized T_{rot} is given by

$$T_{\text{rot}} = \frac{\hat{I}_1^2}{2\mathcal{J}_1} + \frac{\hat{I}_2^2}{2\mathcal{J}_2} + \frac{\hat{I}_3^2}{2\mathcal{J}_3}. \quad (2.25)$$

Let us assume the axial symmetry for the ground state, that is, the potential is minimum at $\beta = \beta_0$ and $\gamma_0 = 0$. In this case, by expanding around the potential minimum, $T_{\text{rot}} - \hat{I}_3^2/2\mathcal{J}_3$ is given by

$$T_{\text{rot}} - \frac{\hat{I}_3^2}{2\mathcal{J}_3} = \frac{\hat{\mathbf{I}}^2 - \hat{I}_3^2}{2\mathcal{J}_0} \quad (2.26)$$

to the zeroth order. Here, $\mathcal{J}_0 = \mathcal{J}_1(\beta_0, 0) = \mathcal{J}_2(\beta_0, 0)$, and the coupling of the vibration and the rotation for this term disappears in this order. Although the remaining term $\frac{\hat{I}_3^2}{2\mathcal{J}_3}$ still couples the vibration and the rotation, the eigenvalues of \hat{I}^2 and \hat{I}_3 are the good quantum numbers because the Hamiltonian, \hat{I}^2 , and \hat{I}_3 commute with each other. For states with the eigenvalue of \hat{I}_3 being zero (for the ground state band and the β -band), the vibration and the rotation decouples. In this case, one can separately solve the vibrational motion and the rotational motion, and the energy eigenvalues are given by

$$E_{n_\beta n_\gamma}(I) = E_{n_\beta n_\gamma}^0 + \frac{\hbar^2}{2\mathcal{J}_0} I(I+1) \quad (2.27)$$

$$I = 0, 2, 4, \dots$$

The states with odd angular momentum ($I = 1, 3, 5, \dots$) are excluded due to the reflection symme-

try around the 1 axis. $E_{n_\beta n_\gamma}^0$ is the energy of the vibrational motion, and is given by

$$E_{n_\beta n_\gamma}^0 = \hbar\omega_\beta \left(n_\beta + \frac{1}{2} \right) + \hbar\omega_\gamma (2n_\gamma + 1) \quad (2.28)$$

$$n_\beta = 0, 1, 2, \dots, \quad n_\gamma = 0, 1, 2, \dots,$$

where $\omega_\beta = \sqrt{C_{20}/B_2}$, $\omega_\gamma = \sqrt{C_{22}/B_2}$. For each (n_β, n_γ) , the spectrum exhibits a band structure obeying $\frac{\hbar^2}{2\mathcal{J}_0} I(I+1)$, ($I = 0, 2, 4, \dots$), and especially for $(n_\beta = 0, n_\gamma = 0)$, the band is called the ground state band. Fig. 2.3 shows the examples of the ground state band.

2.2 Noncollective excitations

As we have seen, the liquid drop model accounts for the collective excitations of a nucleus. On the other hand, the independent particle picture also accounts for various properties of nuclei such as the appearance of the magic numbers. In this picture, nucleons move in a mean field potential produced by themselves. Each nucleon fills a single-particle orbit according to the Pauli principle, and the excited states are obtained by exciting nucleons below the fermi level to levels above the fermi level. Based on this picture, the Tamm-Dancoff method (TDA) describes the nuclear excited states by a superposition of many 1-particle-1-hole(1p-1h) states, that is, the state $|\nu\rangle$ is expanded as

$$|\nu\rangle = \sum_{ph} C_{ph}^\nu a_p^\dagger a_h |\text{HF}\rangle, \quad (2.29)$$

where $|\text{HF}\rangle$ is the ground state in the mean field approximation[55]. a_p^\dagger creates a nucleon above the fermi level(particle state) and a_h annihilates a nucleon below the fermi level(hole state). C_{ph}^ν is the expansion coefficient. By substituting the expansion into the Schrödinger equation, one can obtain the secular equation which determines the coefficient C_{ph}^ν . However, the TDA has a drawback that the correlations due to the residual interaction are not taken into account in the ground state, although they are included in the excited states. The random phase approximation(RPA) overcomes this drawback by introducing the correlations into the ground state. In the RPA, the ground state $|\text{RPA}\rangle$ and the excited states $|\nu\rangle$ are given by

$$Q_\nu |\text{RPA}\rangle = 0 \quad (2.30)$$

$$|\nu\rangle = Q_\nu^\dagger |\text{RPA}\rangle \quad (2.31)$$

where the operator Q_ν^\dagger is defined by

$$Q_\nu^\dagger = \sum_{ph} X_{ph}^\nu a_p^\dagger a_h - \sum_{ph} Y_{ph}^\nu a_h^\dagger a_p. \quad (2.32)$$

In addition to the terms $\sum_{ph} X_{ph}^\nu a_p^\dagger a_h$ which are also present in the TDA, there are other terms $\sum_{ph} Y_{ph}^\nu a_h^\dagger a_p$ which introduce the correlations into the ground state. The coefficients X^ν and Y^ν are determined by the following RPA equation

$$\begin{pmatrix} A & B \\ B^* & A^* \end{pmatrix} \begin{pmatrix} X^\nu \\ Y^\nu \end{pmatrix} = E_\nu \begin{pmatrix} 1 & 0 \\ 0 & -1 \end{pmatrix} \begin{pmatrix} X^\nu \\ Y^\nu \end{pmatrix}, \quad (2.33)$$

where E_ν is the energy eigenvalue. The matrices A and B are given by

$$A_{ph,p'h'} = (\epsilon_p - \epsilon_h) \delta_{pp'} \delta_{hh'} + \bar{v}_{ph'h p'} \quad (2.34)$$

$$B_{ph,p'h'} = \bar{v}_{pp'hh'}, \quad (2.35)$$

where \bar{v} is the nucleon-nucleon interaction, and ϵ_n is the energy of the single-particle state $a_n^\dagger|HF\rangle$. In this description, the collective excitations appear as the states in which the coefficients X_{ph}^ν for many p-h pairs have the same sign, that is, many p-h pairs coherently add up to make the collective states. On the other hand, there appear a large number of noncollective(single-particle) states where $X_{ph} \approx 1$ for a particular p-h pair. If one calculates the strength distribution in RPA, large strengths are found for the low-lying collective states as well as the giant resonances, while the single-particle excited states have smaller strengths.

In Fig. 2.4, we show the energy spectrum for ^{208}Pb nucleus [42], and in Table 2.1, the reduced transition probabilities of the first ten excited states of ^{208}Pb are shown with its excitation energy and the spin-parity. These are shown in the Weisskopf unit and are evaluated from the deformation parameter obtained in the analysis of the high precision proton inelastic scattering experiment[42]. One can see that some excited states, such as 3^- state at 2.615 MeV, have a large $B(E\lambda)$ -value and thus can be considered as the collective phonon states. On the other hand, the excited states with small $B(E\lambda)$ -value are considered to be the noncollective excited states. As the excitation energy increases, the number of the noncollective excited states increases exponentially. We have indicated the 3^- state at 2.615 MeV by the red line in the figure. For this octupole phonon state, candidates for the double phonon multiplet have been identified[58, 59, 60, 61, 62] and are also indicated by the red lines around 5.2 MeV. The spectra of noncollective states do not show the regularity as in the case of collective states. However, some statistical quantities, such as the nearest neighboring spacing of levels(NNS) obey a certain distribution. This is discussed in chapter 4.

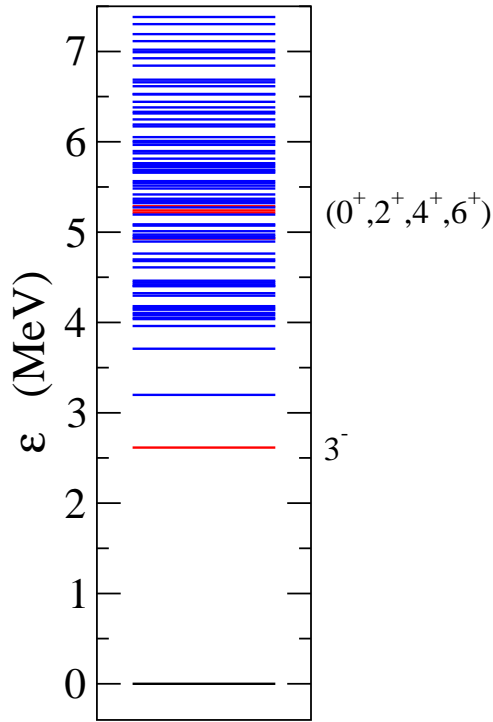


Figure 2.4: Energy spectrum of ^{208}Pb nucleus. The single- and the double- octupole phonon states are shown by the red lines and other excited states are shown by the blue lines. The data is taken from [42].

ϵ (MeV)	λ^π	$B(E\lambda)/B_W(E\lambda)$	
2.615	3^-	286.71	*
3.198	5^-	115.20	*
3.709	5^-	39.59	
3.961	5^-	11.10	
4.037	7^-	77.27	
4.054	3^-	3.26	
4.085	2^+	45.00	*
4.106	3^-	1.93	
4.141	2^+	0.86	
4.159	2^+	0.66	

Table 2.1: Reduced transition probabilities of the first ten excited states of ^{208}Pb evaluated from the deformation parameters [42]. They are shown in the Weisskopf unit. The stars (*) indicate those states that are considered to be collective phonon states.

Chapter 3

Coupled-channels method

In this chapter, a theoretical framework which we employ in this thesis for the description of heavy-ion reactions, that is, the coupled-channels method is detailed. After introducing the concept of barrier distribution for fusion and quasi-elastic scattering, the effects of collective excitations on the barrier distributions are presented.

3.1 Coupled-channels equations

The coupled-channels method describes the coupling of the relative motion to the intrinsic degrees of freedom of the colliding nuclei, that is, the excitations during the scattering process. The coupled-channels method assumes the following Hamiltonian

$$H = -\frac{\hbar^2}{2\mu}\nabla^2 + V_0(r) + H_0(\xi) + V_{\text{coup}}(\mathbf{r}, \xi), \quad (3.1)$$

where \mathbf{r} is the coordinate for the relative motion between the projectile and the target nuclei, and μ is the reduced mass. $H_0(\xi)$ is the intrinsic Hamiltonian, and ξ represents the internal degrees of freedom. $V_0(r)$ is the optical potential for the relative motion. This includes an imaginary part to represent the loss of flux from the considered model space. $V_{\text{coup}}(\mathbf{r}, \xi)$ is the coupling Hamiltonian between the relative motion and the intrinsic degrees of freedom. We expand $V_{\text{coup}}(\mathbf{r}, \xi)$ in terms of spherical harmonics as

$$V_{\text{coup}}(\mathbf{r}, \xi) = \sum_{\lambda>0} f_{\lambda}(r) Y_{\lambda}(\hat{\mathbf{r}}) \cdot T_{\lambda}(\xi), \quad (3.2)$$

where, the dot represents a scalar product. The monopole term ($\lambda = 0$) in the interaction is assumed to be contained in $V_0(r)$ and not included in V_{coup} . Although one can assume more general expansion $V_{\text{coup}}(\mathbf{r}, \xi) = \sum_{\alpha} \sum_{\lambda>0} f_{\lambda}^{\alpha}(r) Y_{\lambda}(\hat{\mathbf{r}}) \cdot T_{\lambda}^{\alpha}(\xi)$, it does not alter the following discussion. Thus, we adopt the expansion (3.2) here for simplicity. Let ϵ_{nl} and $\phi_{nl}(\xi)$ be the eigenvalues and the eigenfunctions

of $H_0(\xi)$ with the spin I , respectively, that is,

$$H_0(\xi)\phi_{nI}(\xi) = \epsilon_{nI}\phi_{nI}(\xi). \quad (3.3)$$

Here, n represents any quantum number besides the angular momentum. Since the total angular momentum and its z component are good quantum numbers, we consider a wave function whose total angular momentum is J and its z component is M , and denote it by $\Psi_{JM}(\mathbf{r}, \xi)$. We construct a basis to expand the total wave function $\Psi_{JM}(\mathbf{r}, \xi)$ as

$$[Y_\ell(\hat{\mathbf{r}})\phi_{nI}(\xi)]^{(JM)} = \sum_{m_\ell, m_I} \langle \ell m_\ell I m_I | JM \rangle Y_{\ell m_\ell}(\hat{\mathbf{r}}) \phi_{nI m_I}(\xi). \quad (3.4)$$

Using this basis, $\Psi_{JM}(\mathbf{r}, \xi)$ is expanded as

$$\Psi_{JM}(\mathbf{r}, \xi) = \sum_{n, \ell, I} \frac{u_{n\ell I}^J(r)}{r} [Y_\ell(\hat{\mathbf{r}})\phi_{nI}(\xi)]^{(JM)}. \quad (3.5)$$

By substituting this expansion to the Schrödinger equation for $\Psi_{JM}(\mathbf{r}, \xi)$

$$H\Psi_{JM}(\mathbf{r}, \xi) = E\Psi_{JM}(\mathbf{r}, \xi) \quad (3.6)$$

and taking an inner product with $[Y_\ell(\hat{\mathbf{r}})\phi_{nI}(\xi)]^{(JM)}$ on the both hand sides, one obtains the following coupled-channels equations

$$\left[-\frac{\hbar^2}{2\mu} \frac{d^2}{dr^2} + \frac{\ell(\ell+1)\hbar^2}{2\mu r^2} + V_0(r) - E + \epsilon_{nI} \right] u_{n\ell I}^J(r) + \sum_{n', \ell', I'} V_{n\ell I, n' \ell' I'}^J(r) u_{n' \ell' I'}^J(r) = 0. \quad (3.7)$$

Here,

$$V_{n\ell I, n' \ell' I'}^J(r) = \langle [Y_\ell \phi_{nI}]^{(JM)} | V_{\text{coup}}(\mathbf{r}, \xi) | [Y_{\ell'} \phi_{n' I'}]^{(JM)} \rangle \quad (3.8)$$

$$= \sum_{\lambda} f_{\lambda}(r) (-1)^{\ell-\ell'} \sqrt{\frac{(2\ell'+1)(2\lambda+1)}{4\pi}} \langle \ell' 0 \lambda 0 | \ell 0 \rangle W(J \ell' I \lambda; I' \ell) \langle \phi_{nI} || T_{\lambda} || \phi_{n' I'} \rangle \quad (3.9)$$

is a coupling matrix element which induces the excitations during the collision. In this expression, $W(abcd; ef)$ represents the Racah coefficient and the reduced matrix element is defined by

$$\langle j' m' | T_{kq} | j m \rangle = \frac{1}{\sqrt{2j'+1}} \langle j m k q | j' m' \rangle \langle j' || T_k || j \rangle. \quad (3.10)$$

We impose the following boundary condition

$$u_{n\ell I}^J(r) \rightarrow H_{\ell_i}^{(-)}(k_{n_i I_i} r) \delta_{n, n_i} \delta_{\ell, \ell_i} \delta_{I, I_i} - \sqrt{\frac{k_{n_i I_i}}{k_{nI}}} S_{n\ell I, n_i \ell_i I_i}^J H_{\ell}^{(+)}(k_{nI} r), \quad (3.11)$$

for $r \rightarrow \infty$, together with the regularity at the origin. Here, $k_{nI} = \sqrt{2\mu(E - \epsilon_{nI})/\hbar^2}$ is the wave number for the channel (n, I) , and the index i represents the entrance channel. $S_{n\ell I, n_i \ell_i I_i}^J$ is the nuclear S -matrix, and $H_\ell^{(-)}(k_{nI}r)$ and $H_\ell^{(+)}(k_{nI}r)$ are the incoming and the outgoing Coulomb wave functions, respectively. For each intrinsic channel with (n, I) , one has to consider subchannels with different ℓ whose coupling with I yields J . Compared to the number of intrinsic states considered, the dimension of the coupled-channels equations is large.

3.2 Iso-centrifugal approximation

One can reduce the dimension of the coupled-channels equations by introducing the iso-centrifugal approximation [30, 31, 32, 33, 34, 35, 36, 37, 38, 39]. In this approximation, the orbital angular momentum ℓ is replaced by the total angular momentum J , that is,

$$\frac{\ell(\ell+1)\hbar^2}{2\mu r^2} \approx \frac{J(J+1)\hbar^2}{2\mu r^2}. \quad (3.12)$$

This procedure corresponds to neglecting the change of the orbital angular momentum during the collision. If one defines $\bar{u}_{nI}^J(r)$ as

$$\bar{u}_{nI}^J(r) = (-1)^I \sum_{\ell} \langle J0I0|\ell 0 \rangle u_{n\ell I}^J(r), \quad (3.13)$$

the coupled-channels equations for $\bar{u}_{nI}^J(r)$ then read,

$$\left[-\frac{\hbar^2}{2\mu} \frac{d^2}{dr^2} + \frac{J(J+1)\hbar^2}{2\mu r^2} + V_0(r) - E + \epsilon_{nI} \right] \bar{u}_{nI}^J(r) \quad (3.14)$$

$$= - \sum_{n', I'} \sum_{\lambda} \sqrt{\frac{2\lambda+1}{4\pi}} f_{\lambda}(r) \langle \phi_{nI0} | T_{\lambda 0} | \phi_{n'I'0} \rangle \bar{u}_{n'I'}^J(r). \quad (3.15)$$

In deriving this expression, the following formula is used[63]

$$\sum_f \sqrt{(2e+1)(2f+1)} W(abcd; ef) \langle b0d0|f0 \rangle \langle a0f0|c0 \rangle = \langle a0b0|e0 \rangle \langle e0d0|c0 \rangle. \quad (3.16)$$

The coupled-channels equations (3.15) have the same form as that for a spin-zero system whose coupling Hamiltonian is given by

$$V_{\text{coup}}(r, \xi) = \sum_{\lambda>0} f_{\lambda}(r) Y_{\lambda}(\hat{\mathbf{r}} = 0) \cdot T_{\lambda}(\xi) = \sum_{\lambda>0} \sqrt{\frac{2\lambda+1}{4\pi}} f_{\lambda}(r) T_{\lambda 0}(\xi). \quad (3.17)$$

This states that the iso-centrifugal approximation corresponds to considering a scattering in the rotating frame where the z axis points at each instant along the separation vector, which is schematically represented in Fig.3.1. Notice that the direction of the z -axis is time-dependent in this picture.

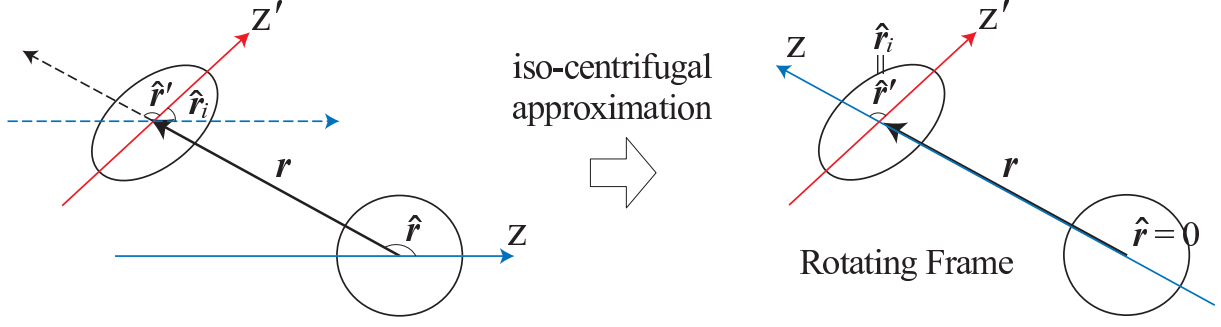


Figure 3.1: The angles in the original coordinate systems(left), and those in the iso-centrifugal approximations(right).

In solving the reduced coupled-channels equations, we impose the following boundary condition

$$\tilde{u}_{nI}^J(r) \rightarrow H_J^{(-)}(k_{nI}r)\delta_{I,I_i}\delta_{n,n_i} - \sqrt{\frac{k_{nI}I_i}{k_{nI}}} S_{nI,n_iI_i}^J H_J^{(+)}(k_{nI}r) \quad \text{as } r \rightarrow \infty. \quad (3.18)$$

The fusion cross sections are identified with the absorption cross sections and are calculated from the obtained S -matrix as

$$\sigma_{\text{fus}}(E) = \frac{\pi}{k_{nI}^2} \sum_J (2J+1) \left(1 - \sum_{n,I} |S_{nI,n_iI_i}^J|^2 \right). \quad (3.19)$$

On the other hand, the differential cross sections for the channel (n, I) are given by

$$\frac{d\sigma_{nI}}{d\Omega} = \frac{k_{nI}}{k_{nI_i}} |f_{nI,n_iI_i}(\theta)|^2 \quad (3.20)$$

with the scattering amplitude

$$f_{nI,n_iI_i}(\theta) = \frac{1}{2i\sqrt{k_{nI}k_{nI_i}}} \sum_J e^{i[\sigma_J(E) + \sigma_J(E - \epsilon_{nI})]} (2J+1) P_J(\cos\theta) (S_{nI,n_iI_i}^J - \delta_{n,n_i}\delta_{I,I_i}) + f_C(\theta)\delta_{n,n_i}\delta_{I,I_i}, \quad (3.21)$$

where $\sigma_J(E)$ and $f_C(\theta)$ are the Coulomb phase shift and the Coulomb scattering amplitude, respectively. The quasi-elastic scattering cross section is then defined by the sum of the elastic and the inelastic cross sections, that is,

$$\frac{d\sigma_{\text{qel}}}{d\Omega} = \sum_{n,I} \frac{d\sigma_{nI}}{d\Omega}. \quad (3.22)$$

The iso-centrifugal approximation has been found to be a good approximation for heavy-ion reactions [34]. In order to see the validity of this approximation, we consider the fusion reaction of $^{24}\text{Mg} + ^{90}\text{Zr}$ system. We take into account rotational excitations of ^{24}Mg up to the 4^+ state with the excitation energy $\epsilon_2 = 1.37$ MeV and the deformation parameter $\beta_2 = 0.505$. In this case, for $J \geq 4$, the dimension of the coupled-channels equations in the full angular coupling scheme amounts to 9

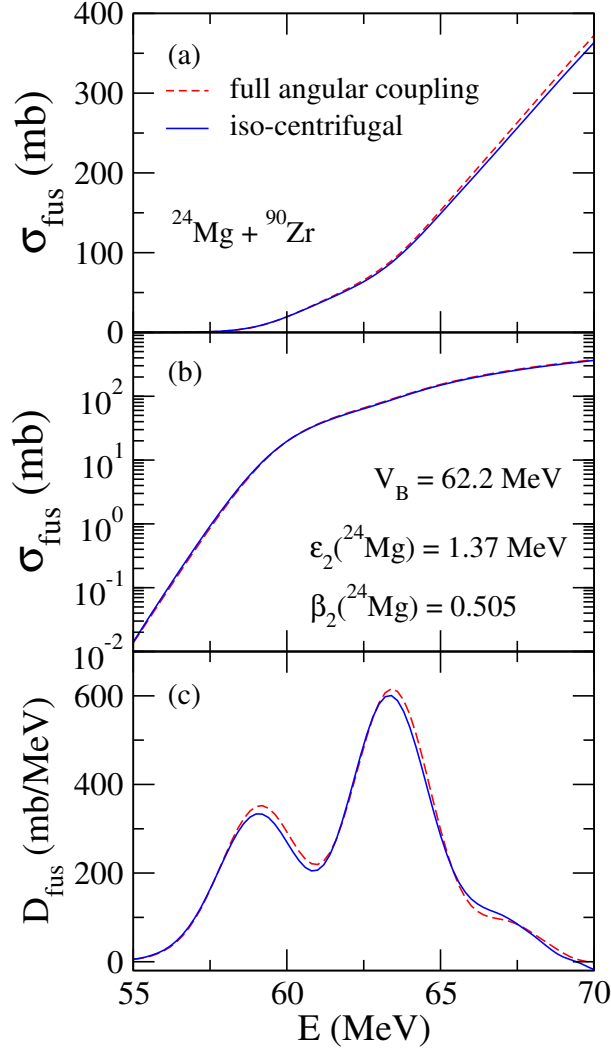


Figure 3.2: Fusion cross sections and fusion barrier distribution for $^{24}\text{Mg} + ^{90}\text{Zr}$ system. Fig. 3.2(a) and 3.2(b) show the fusion cross section in the linear and logarithmic scales, respectively and Fig. 3.2(c) represents the fusion barrier distribution. The red dashed lines represent the result in the full angular coupling while the blue solid lines represent the result in the iso-centrifugal approximation.

$[(I, \ell) = (0, J), (2, J), (4, J), (2, J \pm 2), (4, J), (4, J \pm 2), (4, J \pm 4)]$, while it reduces to 3 $[I = 0, 2, 4]$ in the iso-centrifugal approximation. If one takes into account two more rotational states up to the 8^+ state, the number of the coupled-channels equations in the full angular coupling becomes 25.

In Fig.3.2, we show the result of numerical calculation. The solid blue lines and the red dashed lines show the result with and without the iso-centrifugal approximation, respectively. Fig.3.2(a) and (b) show the fusion cross section in the linear and logarithmic scales, respectively and Fig.3.2(c) represents the fusion barrier distribution defined in Sec.3.4. Although one can observe some discrepancy between the two calculations for fusion cross sections above the barrier and the fusion barrier distribution, the difference is rather small. This comparison shows the validity of the iso-centrifugal approximation.

3.3 Sudden tunneling limit

We have now obtained the coupled-channels equations to be solved. In the following, we shall see the consequence of the channel coupling. First we consider the case where the excitation energies are neglected. We assume that only a single mode with λ in the coupling Hamiltonian is involved for simplicity. In this case, one can diagonalize the coupling matrix with a coordinate independent matrix and decouple the coupled-channels equations. The approximation neglecting the excitation energies is referred to as the sudden tunneling approximation and corresponds to assuming that the tunneling process occurs much faster than the internal motion of the colliding nuclei. Here, we show that the coupled-channels equations are decoupled in this limit and the concept of the barrier distributions naturally appears.

The coupled-channels equations in the sudden tunneling limit are given by

$$\left[-\frac{\hbar^2}{2\mu} \frac{d^2}{dr^2} + \frac{J(J+1)\hbar^2}{2\mu r^2} + V_0(r) - E \right] u_n^J(r) = - \sum_{n'} \sqrt{\frac{2\lambda+1}{4\pi}} f_\lambda(r) \langle \phi_n | T_{\lambda 0} | \phi_{n'} \rangle u_{n'}^J(r), \quad (3.23)$$

where, the label of the intrinsic spin I are omitted for simplicity. One can diagonalize the coupling matrix

$$V_{nm}(r) = \sqrt{\frac{2\lambda+1}{4\pi}} f_\lambda(r) \langle \phi_n | T_{\lambda 0} | \phi_m \rangle \quad (3.24)$$

with a coordinate independent matrix U which diagonalizes the matrix $\langle \phi_n | T_{\lambda 0} | \phi_m \rangle$, that is,

$$U^\dagger V U = \text{diag} \{ \lambda_1(r), \lambda_2(r), \dots, \lambda_N(r) \}. \quad (3.25)$$

Here, N stands for the dimension of the coupled-channels equations. Each eigenvalue of V is given by the product of the eigenvalue of the matrix $\sqrt{\frac{2\lambda+1}{4\pi}} \langle \phi_n | T_{\lambda 0} | \phi_m \rangle$ and $f_\lambda(r)$. The coupled-channels equations are then transformed to

$$\left[-\frac{\hbar^2}{2\mu} \frac{d^2}{dr^2} + \frac{J(J+1)\hbar^2}{2\mu r^2} + V_0(r) + \lambda_\alpha(r) - E \right] v_\alpha^J(r) = 0. \quad (3.26)$$

Here, $v_\alpha^J(r) = U^\dagger u^J(r)$, or $v_\alpha^J(r) = \sum_n U_{n\alpha}^*(r) u_n^J(r)$. We call the channel α in this representation an eigenchannel and the potential barrier given by $V(r) + \lambda_\alpha(r)$ an eigenbarrier. The boundary condition for $v_\alpha(r)$ now reads

$$v_\alpha^J(r) \rightarrow \sum_n U_{n\alpha}^* \{ H_J^{(-)}(k_{n_i} r) \delta_{n, n_i} - S_{nn_i}^J H_J^{(+)}(k_n r) \} \quad (3.27)$$

$$= U_{n_i\alpha}^* \{ H_J^{(-)}(k_{n_i} r) - \tilde{S}_{\alpha n_i}^J H_J^{(+)}(k_n r) \} \quad (3.28)$$

for $r \rightarrow \infty$. Here, we have removed a factor $\sqrt{\frac{k_{n_i}}{k_n}}$ because it equals to unity in the sudden tunneling limit, and $\tilde{S}_{\alpha n_i}^J$ is defined by

$$\tilde{S}_{\alpha n_i}^J = \sum_n \frac{U_{n\alpha}^*}{U_{n_i\alpha}^*} S_{nn_i}^J. \quad (3.29)$$

By taking an absolute square of the both hand sides of $U_{n_i\alpha}^* \tilde{S}_{\alpha n_i}^J = \sum_n U_{n\alpha}^* S_{nn_i}^J$ and summing over α , one can show

$$\sum_n |S_{nn_i}^J|^2 = \sum_\alpha |U_{n_i\alpha}|^2 |\tilde{S}_{\alpha n_i}^J|^2. \quad (3.30)$$

Substitution of the above relation to Eq. (3.19) gives

$$\sigma_{\text{fus}}(E) = \sum_\alpha w_\alpha \sigma_{\text{fus}}^{(\alpha)}(E) \quad (3.31)$$

with the weight factor $w_\alpha = |U_{n_i\alpha}|^2$ and the fusion cross section for eigenchannel α

$$\sigma_{\text{fus}}^{(\alpha)}(E) = \frac{\pi}{k_0^2} \sum_J (2J+1) \left(1 - |\tilde{S}_{\alpha n_i}^J|^2\right), \quad (3.32)$$

where $k_0 = \sqrt{\frac{2\mu E}{\hbar^2}}$. Similarly, one can show

$$S_{nn_i}^J = \sum_\alpha U_{n_i\alpha}^* U_{n\alpha} \tilde{S}_{\alpha n_i}^J, \quad (3.33)$$

and correspondingly, the scattering amplitude is now written as

$$f_n(\theta) = \sum_\alpha U_{n_i\alpha}^* U_{n\alpha} \tilde{f}_\alpha(\theta) \quad (3.34)$$

with

$$\tilde{f}_\alpha(\theta) = \frac{1}{2ik_0} \sum_J e^{2i\sigma_J} (2J+1) P_J(\cos\theta) (S_{\alpha n_i}^J - 1) + f_C(\theta). \quad (3.35)$$

The quasi-elastic scattering cross sections are represented as

$$\frac{d\sigma_{\text{qel}}}{d\Omega} = \sum_\alpha w_\alpha \frac{d\sigma_{\text{el}}^{(\alpha)}}{d\Omega} = \sum_\alpha w_\alpha |\tilde{f}_\alpha(\theta)|^2. \quad (3.36)$$

From these expressions, one can see that both the fusion cross sections and the quasi-elastic cross sections are given by the weighted sum of the cross sections over the eigenchannels in the sudden tunneling limit. Some eigenchannels have the barrier lower than the original Coulomb barrier,

and the others have higher ones. This leads to the concept of the barrier distribution for the fusion reaction and the quasi-elastic scattering. In the following section, we explain how the barrier distribution is extracted from experimental fusion and quasi-elastic cross sections.

3.4 Barrier distribution method

In order to get further understanding of the experimental data for heavy-ion reactions, Rowley, Satchler, and Stelson introduced a method to extract distribution of barriers directly from the experimental fusion cross sections[6]. To illustrate the method, let us consider the classical expression for the fusion cross section. It is given by

$$\sigma_{\text{fus}}^{\text{cl}}(E) = \pi R_B^2 \left(1 - \frac{V_B}{E}\right) \theta(E - V_B), \quad (3.37)$$

where V_B is the Coulomb barrier height and R_B is the barrier radius, that is $V(r = R_B) = V_B$. $\theta(x)$ is the step function. For a derivation of this equation, see Appendix A. From this expression, one can immediately get the classical barrier penetrability by

$$\frac{1}{\pi R_B^2} \frac{d(E\sigma_{\text{fus}}^{\text{cl}})}{dE} = \theta(E - V_B), \quad (3.38)$$

and the derivative of the penetrability gives a delta function which has a peak at $E = V_B$. In quantum mechanics, the quantum tunneling effect smears the delta function. For example, if one approximates the potential barrier by a parabolic potential, $V(r) \approx V_B - \frac{1}{2}\mu\Omega^2(r - R_B)^2$, the fusion cross sections are given by the following Wong formula[64]

$$\sigma_{\text{fus}}(E) = \frac{\hbar\Omega R_B^2}{2E} \ln \{1 + \exp [(2\pi/\hbar\Omega)(E - V_B)]\}, \quad (3.39)$$

and the second derivative of $E\sigma_{\text{fus}}$ gives

$$\frac{1}{\pi R_B^2} \frac{d^2(E\sigma_{\text{fus}})}{dE^2} = \frac{2\pi}{\hbar\Omega} \frac{e^x}{(1 + e^x)^2}, \quad (3.40)$$

where $x = (2\pi/\hbar\Omega)(E - V_B)$. This quantity is called the fusion barrier distribution and has a peak at $E = V_B$. We show in Fig. 3.3 the fusion cross sections and the fusion barrier distribution of the Wong formula for $^{20}\text{Ne} + ^{90}\text{Zr}$ system. The height, position, and curvature of the Coulomb barrier are $V_B = 52.0$ MeV, $R_B = 10.4$ fm, and $\hbar\Omega = 4.05$ MeV, respectively. For comparison, the classical fusion cross sections are also shown by the dotted line. The width of the barrier distribution is related to the curvature of the parabola, that is, the full width half maxima(FWHM) is given by $0.56\hbar\Omega$. For the detail, see appendix A.

In the previous section, we have seen that the fusion cross sections are give by the weighted sum of the fusion cross sections over the eigenchannels in the sudden tunneling limit. By taking

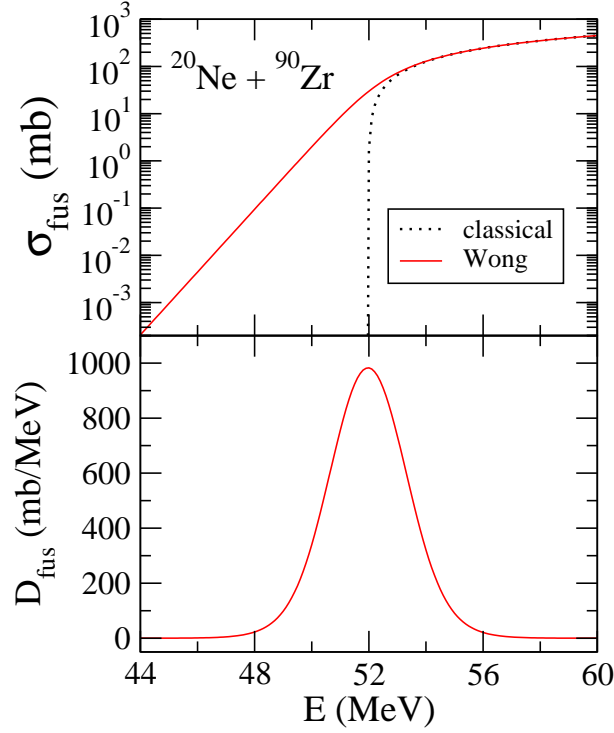


Figure 3.3: The upper panel: Fusion cross sections for $^{20}\text{Ne} + ^{90}\text{Zr}$ system from the Wong formula (the red solid line). The black dotted line is the classical fusion cross sections. The lower panel: Corresponding fusion barrier distribution defined by Eq. (3.40).

the second derivative of the product of E and the both hand sides of Eq. (3.31), we get

$$D_{\text{fus}}(E) = \frac{1}{\pi R_b^2} \frac{d^2(E\sigma_{\text{fus}})}{dE^2} = \sum_{\alpha} w_{\alpha} \frac{1}{\pi R_b^2} \frac{d^2(E\sigma_{\text{fus}}^{(\alpha)})}{dE^2}. \quad (3.41)$$

Each term in the sum has a peak at the position of the eigenbarrier, and the $D_{\text{fus}}(E)$ is given by the weighted sum of them. Thus, the $D_{\text{fus}}(E)$ represents a distribution of eigenbarriers and is called fusion barrier distribution. Rowley *et al.* proposed that one can extract the fusion barrier distribution from measured fusion cross sections $\sigma_{\text{fus}}(E)$ [6]. Compared to the fusion cross sections themselves, the fusion barrier distribution more clearly indicates the effect of the coupling. In fact, it can serve for the determination of deformation parameters[12]. Note that although the fusion cross section contains the contributions from all partial waves, the differentiation of it gives the penetrability of the potential for s-wave as can be seen from Eq. (3.38).

In the actual calculation of the fusion barrier distribution from the fusion cross sections, one replaces the differentiation with finite difference, that is, the value of the barrier distribution at

energy $(E_1 + 2E_2 + E_3)/4$ is calculated as

$$\frac{d^2(E\sigma_{\text{fus}})}{dE^2} = 2 \left(\frac{(E\sigma_{\text{fus}})_3 - (E\sigma_{\text{fus}})_2}{E_3 - E_2} - \frac{(E\sigma_{\text{fus}})_2 - (E\sigma_{\text{fus}})_1}{E_2 - E_1} \right) \left(\frac{1}{E_3 - E_1} \right), \quad (3.42)$$

where $(E\sigma_{\text{fus}})_i$ are evaluated at energies E_i . If one uses equal energy intervals $\Delta E = (E_2 - E_1) = (E_3 - E_2)$, this reduces to

$$\frac{d^2(E\sigma_{\text{fus}})}{dE^2} = \left(\frac{(E\sigma_{\text{fus}})_3 - 2(E\sigma_{\text{fus}})_2 + (E\sigma_{\text{fus}})_1}{\Delta E^2} \right). \quad (3.43)$$

The error δ_c is estimated as[3]

$$\delta_c \approx \left(\frac{E}{\Delta E^2} \right) \sqrt{(\delta\sigma_{\text{fus}})_1^2 + 4(\delta\sigma_{\text{fus}})_2^2 + (\delta\sigma_{\text{fus}})_3^2}. \quad (3.44)$$

The value of ΔE is usually taken about 2 MeV in the center-of-mass frame. For calculations presented in this thesis, $\Delta E = 2$ MeV is always adopted.

A similar concept has been also applied to the quasi-elastic scattering [7, 8]. As in the case of fusion reaction, let us first consider the classical expression for scattering. In the limit of the strong Coulomb field, the elastic scattering cross section at $\theta = \pi$ is given by

$$\sigma_{\text{el}}^{\text{cl}}(E, \pi) = \sigma_{\text{R}}(E, \pi) \theta(V_{\text{B}} - E), \quad (3.45)$$

where $\sigma_{\text{R}}(E, \theta)$ is the Rutherford cross section. Thus, $\sigma_{\text{el}}^{\text{cl}}(E, \pi)/\sigma_{\text{R}}(E, \pi)$ equals to $\theta(V_{\text{B}} - E)$ and this corresponds to the reflection probability. By differentiating it with respect to energy, one gets

$$D_{\text{qel}}(E, \pi) = - \frac{d(\sigma_{\text{qel}}(E, \pi)/\sigma_{\text{R}}(E, \pi))}{dE} = \delta(E - V_{\text{B}}). \quad (3.46)$$

Since in the sudden tunneling limit, the quasi-elastic cross sections are represented by the weighted sum of the elastic cross sections over the eigenchannels as in the fusion case, $D_{\text{qel}}(E, \pi)$ also gives the distribution of eigenbarriers. Although the discussion here assumed a strong Coulomb field in the scattering, the nuclear effect has to be taken into account for realistic systems. In fact, the elastic cross section deviates from the Rutherford cross section as the incident energy increases (cf. Fig. 1.1). Nevertheless, the quasi-elastic barrier distribution exhibits a similar behavior to the fusion barrier distribution, although the quasi-elastic barrier distribution is usually more smeared[7, 8, 10]. In Fig. 3.4, we show the comparison of the fusion and the quasi-elastic barrier distributions for $^{24}\text{Mg} + ^{90}\text{Zr}$ system. The red solid line represents the fusion barrier distribution and the blue dashed line represents the quasi-elastic barrier distribution. The upper panel is for the calculation without channel coupling and the lower panel is for the calculation which includes the rotational excitations of ^{24}Mg up to 4^+ state. All of the barrier distributions are normalized to unit area in the energy interval between 50 and 75 MeV. One can see that the quasi-elastic barrier distribution of the single-channel calculation exhibits more asymmetric behavior compared to that of the fusion, that

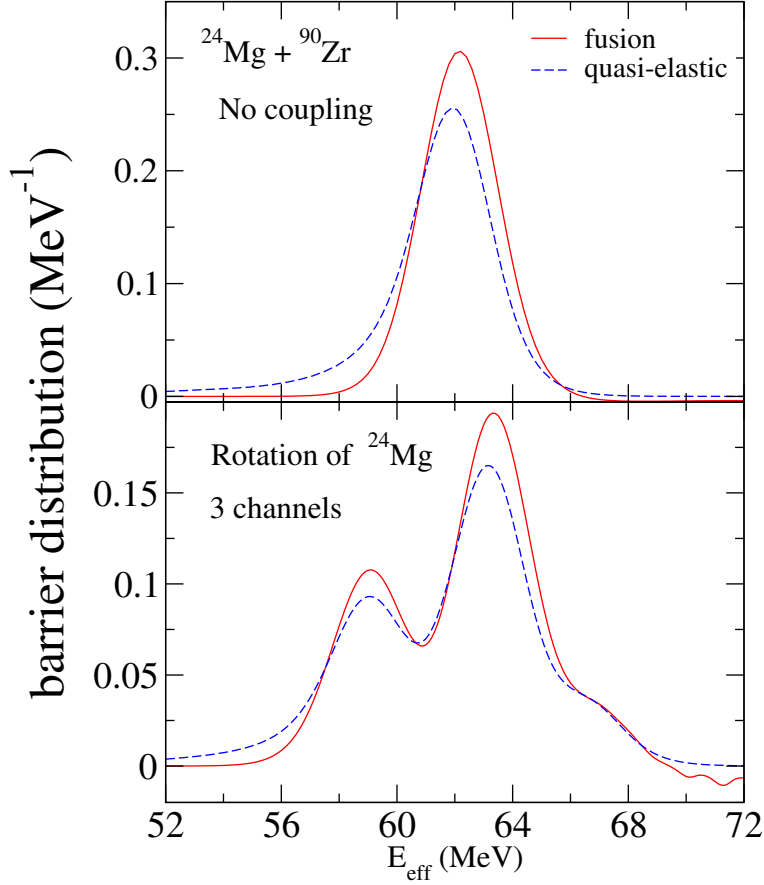


Figure 3.4: Comparison of the fusion(the red solid line) and the quasi-elastic(the blue dashed line) barrier distributions for $^{24}\text{Mg} + ^{90}\text{Zr}$ system. They are normalized to unity if integrated over the energy.

is, it possesses a moderate tail at the lower energy side. However, the behavior of the both barrier distributions is quite similar, while the peaks in the quasi-elastic barrier distribution are somewhat smaller than those of the fusion case. In evaluating the quasi-elastic barrier distribution, we replace the differentiation by finite difference as in the fusion barrier distribution. The energy interval ΔE is taken to be 2 MeV in our calculations in this thesis.

In actual experiments, detection of the scattered particle at $\theta = \pi$ is impossible. However, one can correct the effect of the difference in the detection angles by subtracting the centrifugal energy from the incident energy. Estimating the centrifugal potential at the Coulomb turning point r_c , the effective energy is given by

$$E_{\text{eff}} = E - \frac{\lambda_c^2 \hbar^2}{2\mu r_c^2} = 2E \frac{\sin \frac{\theta}{2}}{1 + \sin \frac{\theta}{2}}, \quad (3.47)$$

where, $\lambda_c = \eta \cot \frac{\theta}{2}$ with η being the Sommerfeld parameter, and r_c is defined by $E = \frac{Z_p Z_T e^2}{r_c} + \frac{\lambda_c^2 \hbar^2}{2\mu r_c^2}$.

While one has to take a second derivative of $E\sigma_{\text{fus}}$ to extract the fusion barrier distribution,

one can get the quasi-elastic barrier distribution by differentiating $\sigma_{\text{qel}}/\sigma_{\text{R}}$ one time. As mentioned above, the scattering angle is classically related to the orbital angular momentum. Therefore, by choosing the scattering at $\theta = \pi$, one can attain the penetrability for s-wave without differentiation.

We have introduced the barrier distribution method based on the eigenchannel representation in the sudden tunneling limit. However, the concept of the barrier distribution has been found to be valid even if the finite excitation energy is taken into account. In that case, the weight factors in the eigenchannel representation become energy dependent and change slowly with the energy[65].

3.5 Constant coupling approximation

In the previous section, we have seen that the eigenchannel representation in the sudden tunneling limit leads to the barrier distribution method. The eigenchannel representation can be introduced also when the coupling matrix is coordinate independent. This approximation is called a constant coupling approximation[5]. In this approximation, the coupled-channels equations read

$$\left[-\frac{\hbar^2}{2\mu} \frac{d^2}{dr^2} + \frac{J(J+1)\hbar^2}{2\mu r^2} + V_0(r) - E \right] u_n^J(r) = - \sum_m \left[\epsilon_n \delta_{n,m} + \sum_\lambda \sqrt{\frac{2\lambda+1}{4\pi}} f_\lambda^0 \langle \phi_n | T_{\lambda 0} | \phi_m \rangle \right] u_m^J(r), \quad (3.48)$$

where, f_λ^0 is a constant. One can diagonalize the matrix

$$V_{nm} = \epsilon_n \delta_{n,m} + \sum_\lambda \sqrt{\frac{2\lambda+1}{4\pi}} f_\lambda^0 \langle \phi_n | T_{\lambda 0} | \phi_m \rangle \quad (3.49)$$

with a coordinate independent matrix as in the case of the sudden tunneling limit, and the fusion and the quasi-elastic cross sections are given by the weighted sum of the cross sections over the eigenchannels.

3.6 Coupling to collective states

In this section, coupling effects to collective excited states are reviewed.

3.6.1 Vibrational coupling

First we consider the vibrational coupling for a projectile nucleus. As seen in chapter 2, in the liquid drop model, the shape of the nuclear surface is parametrized as

$$R = R_P \left(1 + \sum_\lambda \alpha_\lambda \cdot Y_\lambda \right). \quad (3.50)$$

In the following discussion, we consider a particular mode λ . The Hamiltonian for the vibration is given by (2.6). After quantization procedure, the Hamiltonian is represented as

$$H = \sum_{\mu} \frac{1}{2} \hbar \omega_{\lambda} b_{\lambda\mu}^{\dagger} b_{\lambda\mu}, \quad (3.51)$$

where, $\omega_{\lambda} = \sqrt{C_{\lambda}/B_{\lambda}}$, and the zero-point energy is removed. The creation and the annihilation operators $b_{\lambda\mu}^{\dagger}$ and $b_{\lambda\mu}$ are related with $\alpha_{\lambda\mu}$ by

$$\alpha_{\lambda\mu} = \sqrt{\frac{\hbar}{2B_{\lambda}\omega_{\lambda}}} (b_{\lambda\mu}^{\dagger} + (-1)^{\mu} b_{\lambda\mu}). \quad (3.52)$$

The deformation parameter for the vibration with λ is defined by the square root of the amplitude of the zero-point vibration, that is,

$$\beta_{\lambda}^2 = \langle n_{\lambda} = 0 | \sum_{\mu} \alpha_{\lambda\mu}^{\dagger} \alpha_{\lambda\mu} | n_{\lambda} = 0 \rangle \quad (3.53)$$

$$= (2\lambda + 1) \frac{\hbar}{2B_{\lambda}\omega_{\lambda}}. \quad (3.54)$$

Thus, Eq. (3.52) is rewritten as

$$\alpha_{\lambda\mu} = \frac{\beta_{\lambda}}{\sqrt{2\lambda + 1}} (b_{\lambda\mu}^{\dagger} + (-1)^{\mu} b_{\lambda\mu}). \quad (3.55)$$

The nuclear potential between the colliding nuclei is given by a function of the distance between the nuclear surface points on a line connecting the center of each nucleus. For spherical nuclei with the radius R_T and R_P , the distance is given by $r - R_T - R_P$. If one takes into account the coupling of the projectile, the nuclear potential is obtained by replacing $r - R_T - R_P$ by $r - R_T - R_P - R_P \alpha_{\lambda} \cdot Y_{\lambda}$, that is, the nuclear potential $V_N(r)$ is replaced by $V_N(r - R_P \alpha_{\lambda} \cdot Y_{\lambda}(\hat{\mathbf{r}}))$. In order to extract a form factor of the coupling Hamiltonian, let us assume that the β_{λ} is small and expand the potential up to the first order term with respect to β_{λ} (the linear coupling approximation)

$$V_N(r - R_P \alpha_{\lambda} \cdot Y_{\lambda}(\hat{\mathbf{r}})) \approx V_N(r) - R_P \frac{dV_N(r)}{dr} \alpha_{\lambda} \cdot Y_{\lambda}(\hat{\mathbf{r}}). \quad (3.56)$$

The second term gives the nuclear part of the coupling Hamiltonian.

Next we consider the Coulomb part of the coupling Hamiltonian. Let us denote the density of the vibrating projectile by $\rho_P(\mathbf{r})$. Then, the Coulomb potential between the colliding nuclei is given by

$$V_C(\mathbf{r}) = \int d\mathbf{r}' \frac{Z_P Z_T e^2}{|\mathbf{r} - \mathbf{r}'|} \rho_P(\mathbf{r}') \quad (3.57)$$

for \mathbf{r} larger than the range of $\rho_P(\mathbf{r})$. By using the expansion formula

$$\frac{1}{|\mathbf{r} - \mathbf{r}'|} = \sum_{\lambda'\mu'} \frac{4\pi}{2\lambda' + 1} \frac{r_{<}^{\lambda'}}{r_{>}^{\lambda'+1}} Y_{\lambda'\mu'}(\hat{\mathbf{r}}') Y_{\lambda'\mu'}^*(\hat{\mathbf{r}}), \quad (3.58)$$

the potential is represented as

$$V_C(\mathbf{r}) = \frac{Z_P Z_T e^2}{r} + \sum_{\lambda' > 0} \sum_{\mu'} \frac{4\pi Z_T e}{2\lambda' + 1} Q_{\lambda\mu'} Y_{\lambda'\mu'}^*(\hat{\mathbf{r}}) \frac{1}{r^{\lambda'+1}}, \quad (3.59)$$

where, the electric multipole operator is defined as

$$Q_{\lambda\mu} = \int d\mathbf{r} Z_P e \rho_P(\mathbf{r}) r^\lambda Y_{\lambda\mu}(\hat{\mathbf{r}}). \quad (3.60)$$

Assuming a sharp distribution for $\rho_P(\mathbf{r})$, that is,

$$\rho_P(\mathbf{r}) = \rho_0 \theta(R(\theta, \phi) - r), \quad \rho_0 = \frac{3}{4\pi R_P^3}, \quad (3.61)$$

$Q_{\lambda'\mu'}$ is given by

$$Q_{\lambda'\mu'} = \frac{3Z_P e}{4\pi} R_P^\lambda \alpha_{\lambda\mu'} \delta_{\lambda\lambda'} \quad (3.62)$$

up to the first order in $\alpha_{\lambda\mu}$. Thus, the Coulomb potential reads

$$V_C(\mathbf{r}) = \frac{Z_P Z_T e^2}{r} + \frac{3}{2\lambda + 1} Z_P Z_T e^2 \frac{R_P^\lambda}{r^{\lambda+1}} \alpha_\lambda \cdot Y_\lambda(\hat{\mathbf{r}}), \quad (3.63)$$

and the second term gives the Coulomb part of the coupling Hamiltonian.

Combining the nuclear and the Coulomb potentials, the coupling Hamiltonian is given by

$$V_{\text{coup}}(\mathbf{r}, \alpha_{\lambda\mu}) = f_\lambda(r) \alpha_\lambda \cdot Y_\lambda(\hat{\mathbf{r}}) \quad (3.64)$$

with the form factor

$$f_\lambda(r) = -R_P \frac{dV_N(r)}{dr} + \frac{3}{2\lambda + 1} Z_P Z_T e^2 \frac{R_P^\lambda}{r^{\lambda+1}}. \quad (3.65)$$

Under the iso-centrifugal approximation, V_{coup} becomes

$$\begin{aligned} V_{\text{coup}}(\mathbf{r}, \alpha_{\lambda\mu}) &= f_\lambda(r) \alpha_\lambda \cdot Y_\lambda(\hat{\mathbf{r}} = 0) \\ &= \frac{\beta_\lambda}{\sqrt{4\pi}} f_\lambda(r) (b_{\lambda 0}^\dagger + b_{\lambda 0}). \end{aligned} \quad (3.66)$$

At the position of the barrier R_B , it holds that $dV_0/dr = dV_N/dr + dV_C/dV = 0$, that is,

$$-\left. \frac{dV_N}{dV} \right|_{r=R_B} = -\left. \frac{Z_P Z_T e^2}{r^2} \right|_{r=R_B}. \quad (3.67)$$

The form factor $f_\lambda(r)$ is then estimated at $r = R_B$ as

$$f_\lambda(R_B) = -R_P \frac{Z_P Z_T e^2}{R_B^2} + \frac{3}{2\lambda + 1} Z_P Z_T e^2 \frac{R_P^\lambda}{R_B^{\lambda+1}}. \quad (3.68)$$

One can see that the form factor is proportional to the charge product. Therefore, the coupling strength is effectively stronger for systems which have a larger charge product.

Although the coupled-channels equations (3.15) use the basis where the intrinsic spin I is a good quantum number, it is more efficient to work in another basis for the vibrational excitations in the iso-centrifugal approximation[66]. Let us first consider 1-phonon states. They are given by $\{b_{\lambda\mu}^\dagger|0\rangle\}_\mu$ and these states span the $(2\lambda + 1)$ -dimensional subspace. Among them, only a state $b_{\lambda 0}^\dagger|0\rangle$ can be excited from the ground state by V_{coup} given in (3.66). Thus, it is sufficient to take into account only one channel for 1-phonon states.

Next consider 2-phonon states. They are given by $\{[b_\lambda^\dagger b_\lambda^\dagger]^{(IM)}|0\rangle\}_{IM}$. For $\lambda = 2$ case, the possible values of I are 0, 2, and 4, and the states $(0^+, 2^+, 4^+)$ form a triplet with the same excitation energy. The dimension of the subspace spanned by the 2-phonon states is 15. The set $\{[b_\lambda^\dagger b_\lambda^\dagger]^{(IM)}|0\rangle\}_{IM}$ can be unitary transformed to a set $\{b_{\lambda\mu}^\dagger b_{\lambda\mu'}^\dagger|0\rangle\}_{\mu\mu'}$. Among them, in the iso-centrifugal approximation, only the state $b_{\lambda 0}^\dagger b_{\lambda 0}^\dagger|0\rangle$ can be excited from the 1-phonon state $b_{\lambda 0}^\dagger|0\rangle$ by V_{coup} . Thus, it is sufficient to take into account only one channel for 2-phonon states. One can progress this discussion to n -phonon states, and will find that only one channel is necessary to represent n -phonon states in the iso-centrifugal approximation. Therefore, the total basis is given by $\left\{ \frac{1}{\sqrt{n!}} (b_{\lambda 0}^\dagger)^n |0\rangle \right\}_n$. The coupling matrix element between n -phonon channel and m -phonon channel is then given by

$$V_{nm}(r) = \frac{\beta_\lambda}{\sqrt{4\pi}} f_\lambda(r) (\delta_{n,m-1} \sqrt{m} + \delta_{n,m+1} \sqrt{n}), \quad (3.69)$$

and the matrix is given by

$$(V_{nm}) = \frac{\beta_\lambda}{\sqrt{4\pi}} f_\lambda(r) \begin{pmatrix} 0 & 1 & 0 \\ 1 & 0 & \sqrt{2} \\ 0 & \sqrt{2} & 0 \end{pmatrix}, \quad (3.70)$$

if one truncates the space up to the 2-phonon channel.

As an example of the vibrational coupling, we show in Fig. 3.5 the calculation of the fusion reaction for $^{32}\text{S} + ^{90}\text{Zr}$ system. Figs.3.5(a) and 3.5(b) show the fusion cross sections in the linear and logarithmic scales, respectively. Fig.3.5(c) shows the fusion barrier distribution. The black dotted lines show the calculation without coupling, the red solid lines take into account the vibrational

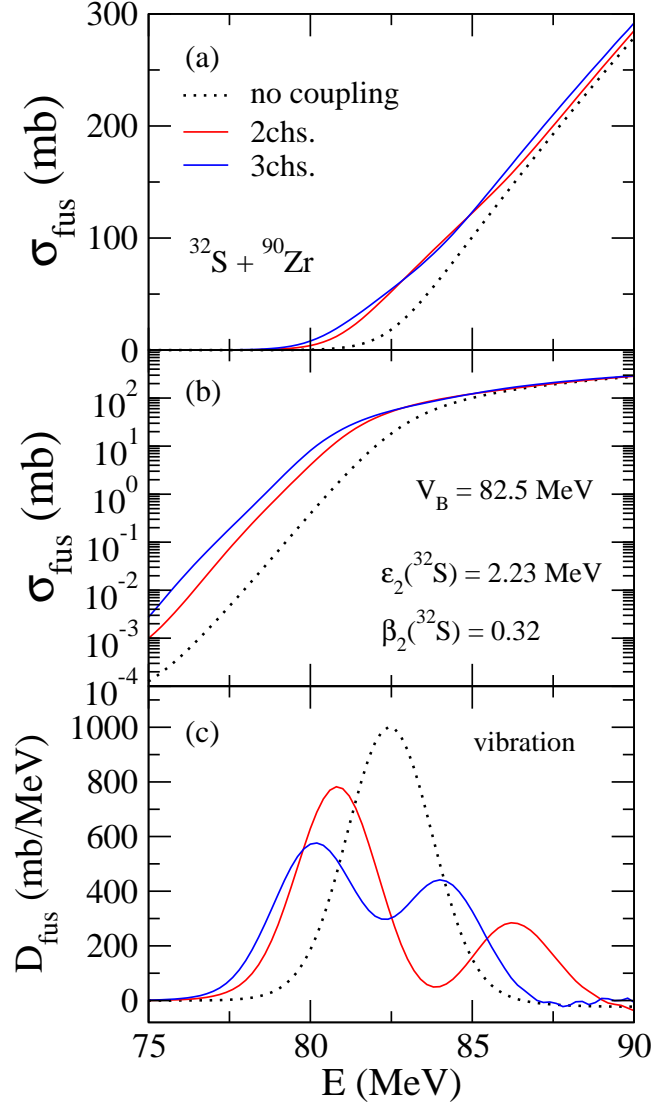


Figure 3.5: Fusion cross sections and fusion barrier distribution for $^{32}\text{S} + ^{90}\text{Zr}$ system. The black dotted lines show the calculation without the channel coupling, the red solid lines take into account the vibrational excitation of ^{32}S up to the 1-phonon state, and the blue solid lines take into account the vibrational excitations up to the 2-phonon state.

quadrupole excitations of ^{32}S up to the one-phonon state, and the blue solid lines includes up to the two-phonon state. The excitation energy and the deformation parameter of the 2^+ state of ^{32}S are $\epsilon_2 = 2.23$ MeV and $\beta_2 = 0.32$, respectively. These calculations include the contribution from all order terms in β_2 in the nuclear coupling (See Sec.3.7). In the absence of the coupling, the barrier distribution shows a single peak at the Coulomb barrier ($V_B = 82.5$ MeV). One can see that by including the coupling, the subbarrier fusion cross sections are enhanced (Fig. 3.5(b)), and the potential barrier distributes in energy. In the case the vibrational coupling, the lower barrier is taller than the higher one.

3.6.2 Rotational coupling

We next consider the rotational excitations of a deformed nucleus. For the deformation, we take into account the quadrupole ($\lambda = 2$) deformation and the hexadecapole ($\lambda = 4$) deformation of the projectile. The nuclear radius is then represented as

$$R(\theta, \phi) = R_P (1 + \alpha_2 \cdot Y_2(\hat{\mathbf{r}}) + \alpha_4 \cdot Y_4(\hat{\mathbf{r}})). \quad (3.71)$$

In the intrinsic system (the body-fixed frame), the radius is expressed as

$$R(\theta', \phi') = R_P (1 + a_2 \cdot Y_2(\hat{\mathbf{r}}') + a_4 \cdot Y_4(\hat{\mathbf{r}}')), \quad (3.72)$$

where, $\hat{\mathbf{r}}' = (\theta', \phi')$ is the angles in the intrinsic system and the relation between $a_{\lambda\mu}$ and $\alpha_{\lambda\mu}$ is given by

$$a_{\lambda\mu} = \sum_{\mu'} D_{\mu\mu'}^{\lambda}(\Omega) \alpha_{\lambda\mu'}. \quad (3.73)$$

Here, $\Omega = (\phi_i, \theta_i, \chi_i)$ is the Euler angle between $\hat{\mathbf{r}}$ and $\hat{\mathbf{r}}'$ (see Fig.3.1). In the axially symmetric case, the nuclear radius is often represented as

$$R(\theta', \phi') = R_P (1 + \beta_2 Y_{20}(\hat{\mathbf{r}}') + \beta_4 Y_{40}(\hat{\mathbf{r}}')). \quad (3.74)$$

For the quadrupole deformation, as we have introduced in section 2, $a_{2\mu}$ are parametrized as

$$a_{20} = \beta_2 \cos \gamma_2 \quad (3.75)$$

$$a_{21} = a_{2-1} = 0 \quad (3.76)$$

$$a_{22} = a_{2-2} = \frac{1}{\sqrt{2}} \beta_2 \sin \gamma_2. \quad (3.77)$$

We have added the suffix 2 to represent the quadrupole degree of freedom, and $\gamma_2 = 0$ and $\gamma_2 = \pi/3$ correspond to axially symmetric deformation with prolate shape and oblate shape, respectively. Since the oblate shape is also represented by negative β_2 with $\gamma_2 = 0$, axially symmetric deformation is described only by β_2 . Similar parametrization is also possible for $a_{4\mu}$ [67]. Due to the reflection symmetry with respect to the $(x - y)$, $(y - z)$, and $(z - x)$ -planes, only a_{40} , a_{42} , and a_{44} are independent variables, and they can be parametrized as follows

$$a_{40} = \beta_4 \left(\sqrt{\frac{7}{12}} \cos \delta_4 + \sqrt{\frac{5}{12}} \sin \delta_4 \cos \gamma_4 \right) \quad (3.78)$$

$$\sqrt{2} a_{42} = -\beta_4 \sin \delta_4 \sin \gamma_4 \quad (3.79)$$

$$\sqrt{2} a_{44} = \beta_4 \left(\sqrt{\frac{5}{12}} \cos \delta_4 - \sqrt{\frac{7}{12}} \sin \delta_4 \cos \gamma_4 \right), \quad (3.80)$$

with $\beta_4 \geq 0$, $0 \leq \delta_4 \leq \pi$, and $0 \leq \gamma_4 \leq \pi/3$. The β_4 represents the magnitude of the hexadecapole deformation, and δ_4 and γ_4 describe the non-axiality. Axial symmetry corresponds to $(\gamma_4 = 0, \delta_4 = \cos^{-1} \sqrt{7/12})$ and $(\gamma_4 = \pi/3, \delta_4 = \pi - \cos^{-1} \sqrt{7/12})$, and the latter is the same shape as the case with negative β_4 and $(\gamma_4 = 0, \delta_4 = \cos^{-1} \sqrt{7/12})$. Thus, by allowing β_4 to be negative, the axially symmetric shape can be described solely by $a_{40} = \beta_4$. The nuclear part of the coupling Hamiltonian for axially symmetric deformation is then given by

$$\begin{aligned} V_{\text{coup}}^{(N)}(\mathbf{r}, \alpha_{\lambda\mu}) &= -R_P \frac{dV_N}{dr} \sum_{\lambda=2,4} \alpha_{\lambda} \cdot Y_{\lambda}(\hat{\mathbf{r}}) = -R_P \frac{dV_N}{dr} \sum_{\lambda=2,4} a_{\lambda} \cdot Y_{\lambda}(\hat{\mathbf{r}}') \\ &= -R_P \frac{dV_N}{dr} \sum_{\lambda=2,4} \beta_{\lambda} Y_{\lambda 0}(\hat{\mathbf{r}}') \end{aligned} \quad (3.81)$$

in the linear coupling approximation.

While the form factor for the Coulomb part of the coupling Hamiltonian has already been obtained in the previous subsection up to the first order in β_{λ} , we consider here the second order terms with respect to $\lambda = 2$, which are included in the actual calculations. The second order term in $Q_{\lambda\mu}$ is calculated as

$$Q_{\lambda\mu}^{(2)} = \frac{3(\lambda+2)}{8\pi} Z_P e R_P^{\lambda} \frac{5}{\sqrt{4\pi(2\lambda+1)}} \langle 2020 | \lambda 0 \rangle [\alpha_2 \alpha_2]^{(\lambda\mu)}, \quad (3.82)$$

and the Coulomb part of the coupling Hamiltonian is then given by

$$\begin{aligned} V_C(\mathbf{r}, \alpha_{\lambda\mu}) &= \sum_{\lambda=2,4} \frac{3}{2\lambda+1} Z_P Z_T e^2 \frac{R_P^{\lambda}}{r^{\lambda+1}} \alpha_{\lambda} \cdot Y_{\lambda}(\hat{\mathbf{r}}) \\ &\quad + \frac{6}{5} \sqrt{\frac{5}{4\pi}} Z_P Z_T e^2 \frac{R_P^2}{r^3} \langle 2020 | 20 \rangle [\alpha_2 \alpha_2]^{(2)} \cdot Y_2(\hat{\mathbf{r}}) \\ &\quad + \frac{5}{3} \frac{1}{\sqrt{4\pi}} Z_P Z_T e^2 \frac{R_P^4}{r^5} \langle 2020 | 40 \rangle [\alpha_2 \alpha_2]^{(4)} \cdot Y_4(\hat{\mathbf{r}}). \end{aligned} \quad (3.83)$$

Combining the nuclear and the Coulomb parts, the total coupling Hamiltonian reads

$$V_{\text{coup}}(\mathbf{r}, \alpha_{\lambda\mu}) = \sum_{\lambda=2,4} \left\{ f_{\lambda}^{(1)}(r) \alpha_{\lambda} \cdot Y_{\lambda}(\hat{\mathbf{r}}) + f_{\lambda}^{(2)}(r) [\alpha_2 \alpha_2]^{(\lambda)} \cdot Y_{\lambda}(\hat{\mathbf{r}}) \right\} \quad (3.84)$$

with

$$f_{\lambda}^{(1)}(r) = -R_P \frac{dV_N}{dr} + Z_P Z_T e^2 \frac{3}{2\lambda+1} \frac{R_P^{\lambda}}{r^{\lambda+1}} \quad (3.85)$$

and

$$f_{\lambda}^{(2)}(r) = \frac{3(\lambda+2)}{2\lambda+1} \frac{5}{\sqrt{4\pi(2\lambda+1)}} Z_P Z_T e^2 \frac{R_P^{\lambda}}{r^{\lambda+1}} \langle 2020 | \lambda 0 \rangle. \quad (3.86)$$

In the iso-centrifugal approximation, this becomes

$$\begin{aligned}
V_{\text{coup}}(\mathbf{r}, \alpha_{\lambda\mu}) = & -R_P \frac{dV_N}{dr} (\beta_2 Y_{20}(\hat{\mathbf{r}}_i) + \beta_4 Y_{40}(\hat{\mathbf{r}}_i)) \\
& + \frac{3}{5} Z_P Z_T e^2 \frac{R_P^2}{r^3} \left\{ \beta_2 + \frac{2}{7} \sqrt{\frac{5}{\pi}} \beta_2^2 \right\} Y_{20}(\hat{\mathbf{r}}_i) \\
& + \frac{3}{9} Z_P Z_T e^2 \frac{R_P^4}{r^5} \left\{ \beta_4 + \frac{9}{7} \frac{1}{\sqrt{\pi}} \beta_2^2 \right\} Y_{40}(\hat{\mathbf{r}}_i),
\end{aligned} \tag{3.87}$$

and the coupling matrix elements are then given by

$$(V_{nm}) = \frac{\beta_2}{\sqrt{4\pi}} f_2^{(1)}(r) \begin{pmatrix} 0 & 1 & 0 \\ 1 & \frac{2\sqrt{5}}{7} & \frac{6}{7} \\ 0 & \frac{6}{7} & \frac{20\sqrt{5}}{77} \end{pmatrix} + \frac{\beta_4}{\sqrt{4\pi}} f_4^{(1)}(r) \begin{pmatrix} 0 & 1 & 0 \\ 1 & \frac{6}{7} & \frac{20\sqrt{5}}{77} \\ 0 & \frac{20\sqrt{5}}{77} & \frac{486}{1001} \end{pmatrix}, \tag{3.88}$$

to the first order in β_λ , if one truncates up to 4^+ state in the rotational band. In Eq.(3.87), $\hat{\mathbf{r}}_i = (\theta_i, \phi_i)$ is a part of the Euler angles which coincides with the angles of the separation vector in the intrinsic frame $\hat{\mathbf{r}} = (\theta', \phi')$ under the iso-centrifugal approximation.

We show in Figs. 3.6 and 3.7 the examples of the rotational coupling for $^{24}\text{Mg} + ^{90}\text{Zr}$ and $^{28}\text{Si} + ^{92}\text{Zr}$ systems. The dotted lines are the single channel calculation, the red solid lines take into account the rotational 2^+ state, and the blue solid lines take into account the 4^+ state in addition to the 2^+ state. For $^{24}\text{Mg} + ^{90}\text{Zr}$ system, the rotational states of ^{24}Mg with the excitation energy $\epsilon_2 = 1.37$ MeV and the deformation parameter $\beta_2 = 0.505$ are included, that is, the rotational excitations associated with a prolate deformation. For $^{28}\text{Si} + ^{92}\text{Zr}$ reaction, the rotational states of ^{28}Si with $\epsilon_2 = 1.78$ MeV and $\beta_2 = -0.407$ are included, that is, the rotational excitations with an oblate deformation. One can see the enhancement of the subbarrier fusion cross sections due to the channel coupling as in the case of the vibrational coupling. For $^{24}\text{Mg} + ^{90}\text{Zr}$ system, the higher peak in the barrier distribution is taller than the lower one, while for $^{28}\text{Si} + ^{92}\text{Zr}$ system, the lower one is taller than the higher one.

3.6.3 Adiabatic potential renormalization

In this section, we consider a coupling to high-lying excited states. The effects of these high-lying states can be compensated by renormalizing the internuclear potential[40]. To understand this, we consider a two-level model where the coupling Hamiltonian is given by

$$(V_{nm} + \epsilon_n \delta_{nm}) = \begin{pmatrix} 0 & f \\ f & \epsilon \end{pmatrix}, \tag{3.89}$$

where f is a constant. The eigenvalues of this matrix are given by

$$\lambda_{\pm} = \frac{1}{2} \left(\epsilon \pm \sqrt{\epsilon^2 + 4f^2} \right), \tag{3.90}$$

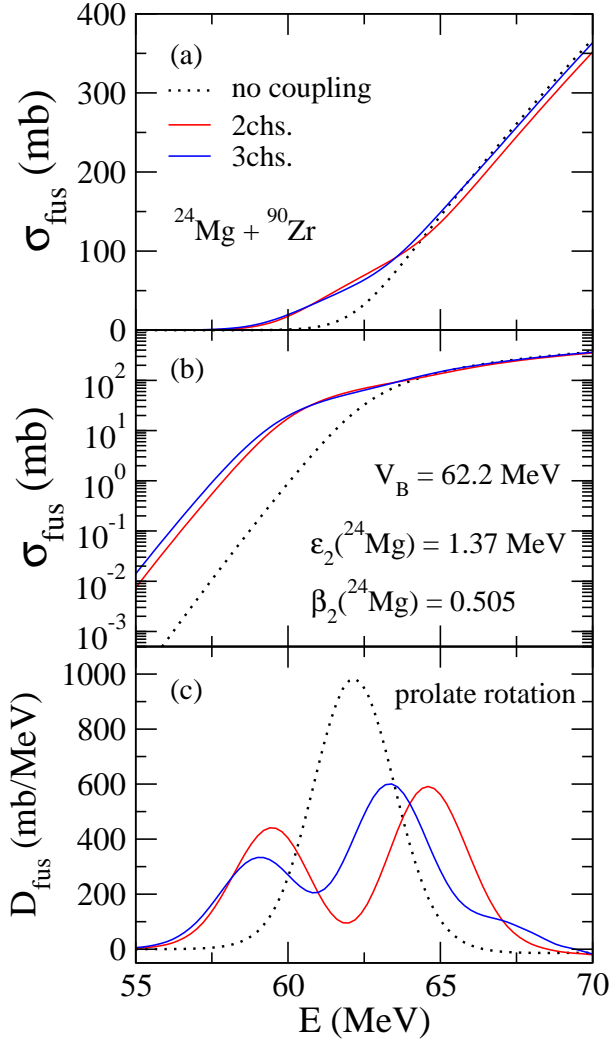


Figure 3.6: Fusion cross sections and fusion barrier distribution for $^{24}\text{Mg} + ^{90}\text{Zr}$ system. The meaning of each line is similar to that in Fig.3.5.

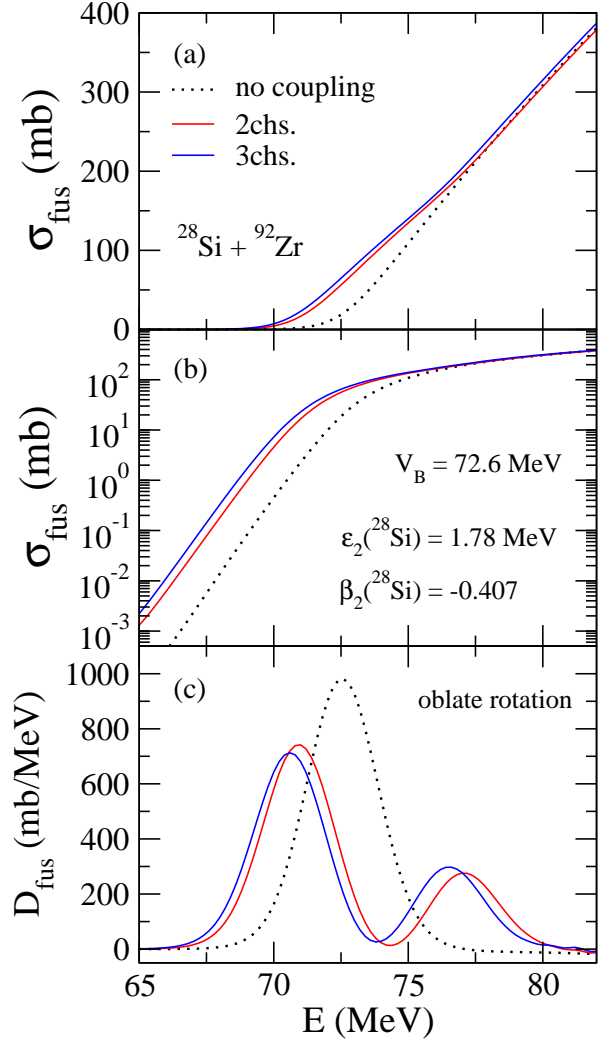


Figure 3.7: Fusion cross sections and fusion barrier distribution for $^{28}\text{Si} + ^{92}\text{Zr}$ system. The meaning of each line is similar to that in Fig.3.5.

and the eigenvectors are given by

$$u_{\pm} = \frac{1}{\sqrt{2}(1+4g^2)^{1/4}} \begin{pmatrix} \sqrt{\sqrt{1+4g^2} \mp 1} \\ \pm \sqrt{\sqrt{1+4g^2} \pm 1} \end{pmatrix}, \quad (3.91)$$

where $g = f/\epsilon$. The weight factor w_{\pm} for the eigenbarriers are given by

$$w_{\pm} = \frac{1}{2} \left(1 \mp \frac{1}{\sqrt{1+4g^2}} \right). \quad (3.92)$$

If ϵ is large, that is, if $g \ll 1$, then $w_{+} \ll 1$ and $w_{-} \approx 1$. Thus, only the lower barrier (the adiabatic potential) is important in this limit. Therefore, the effect of the high-lying states can be effectively taken into account by using the adiabatic potential. This fact is called the adiabatic potential renormalization. As a physical picture, a large excitation energy means that the frequency

of the intrinsic motion is larger than that of the relative motion. In this case, the energy of the whole system is minimized for each separation of the projectile and the target, that is, the reaction proceeds along the valley of the energy surface. This effectively lowers the potential barrier.

In Fig. 3.8, we show the result of the fusion calculation for $^{16}\text{O} + ^{144}\text{Sm}$ system as concrete example of the potential renormalization. For ^{16}O , the first excited state is a 3^- state with high excitation energy of 6.13 MeV. The black solid lines in the figure do not include this octupole phonon state but include only the quadrupole and octupole phonons in ^{144}Sm . On the other hand, the red solid lines include the 3^- state in ^{16}O in addition to the excited states in ^{144}Sm . One can see that the two barrier distributions exhibit similar behavior except for the position of the centroid. In fact, by shifting the red solid lines toward the higher energy side by 2 MeV, one obtains the red dashed lines and it shows almost the same structure as the black one, although the peak height is somewhat enhanced.

3.7 Full order coupling

In the previous sections, the coupling matrices for nuclear coupling are calculated up to the linear order in β_λ for the illustration purpose. However, in the actual calculations, the all order terms are included. This can be done as follows.

In the presence of the coupling, the radius parameter in the potential is replaced as

$$R_0 \rightarrow R_0 + \hat{O}, \quad (3.93)$$

where \hat{O} is given by

$$\hat{O} = \beta_2 R_P Y_{20} + \beta_4 R_P Y_{40} \quad (3.94)$$

for the rotational coupling, and

$$\hat{O} = \frac{R_P}{\sqrt{4\pi}} \beta_\lambda (b_{\lambda 0} + b_{\lambda 0}^\dagger) \quad (3.95)$$

for the vibrational coupling. We first find the eigenvalues and eigenvectors of \hat{O} , that is,

$$\hat{O}|\alpha\rangle = \lambda_\alpha|\alpha\rangle. \quad (3.96)$$

This is equivalent to diagonalize the matrix $O_{nm} = \langle n|\hat{O}|m\rangle$, where $|n\rangle$ is an eigenstate of H_0 . Then the coupling matrix element is calculated as

$$\begin{aligned} V_{nm}^{(N)}(r) &= \langle n|V_N(r, \hat{O})|m\rangle - V_N(r)\delta_{n,m} \\ &= \sum_{\alpha} \langle n|\alpha\rangle\langle\alpha|m\rangle V_N(r, \lambda_\alpha) - V_N(r)\delta_{n,m}. \end{aligned} \quad (3.97)$$

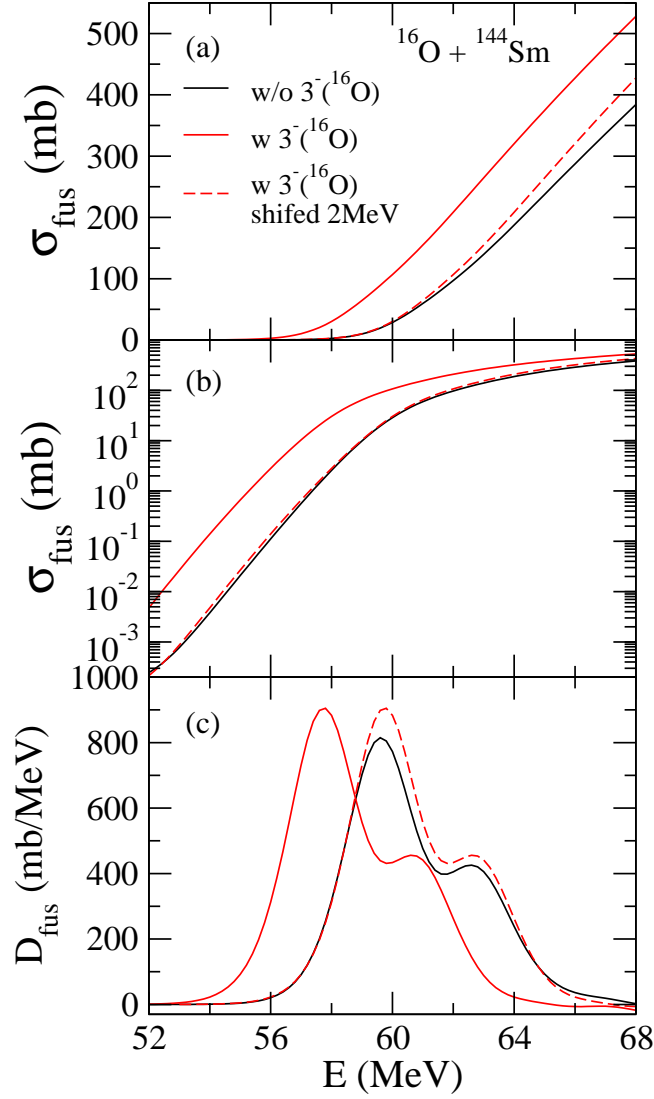


Figure 3.8: The fusion cross sections and the fusion barrier distribution for $^{16}\text{O} + ^{144}\text{Sm}$ system. The black solid lines do not include the octupole phonon state of ^{16}O at 6.13 MeV. The red solid lines include this state, and the red dashed lines are obtained by shifting the red solid lines by 2 MeV toward a higher energy side.

The validity of the linear coupling approximation is discussed in Ref. [68] and it has been clarified that the higher order terms significantly improve the agreement with the data. In this thesis, for quantitative calculations, we work with the full order coupling for collective excitations, unless otherwise we mention.

Chapter 4

Random matrix theory

In the 1960's, Wigner, Mehta, Dyson, Porter, and other people developed statistical studies of nuclear spectra and developed a random matrix theory. In this chapter, fundamental properties of the random matrix theory is presented[69, 70].

4.1 Introduction

In the 1930's, neutron cross sections are measured for heavy even-even nuclei by using slow neutrons[71, 72]. Typical experimental data are shown in Fig. 4.1[56]. It exhibits many narrow resonances whose width is less than 1eV and the energy spacing is about 20eV. Bohr considered that these resonances are incompatible with the independent particle model and proposed a compound nucleus model[73]. Fig.4.2 shows the wooden toy model with which he described the idea of a compound nucleus. This figure shows the situation where a neutron is incident on the assembly of strongly interacting nucleons. Bohr assumed that the energy of the injected neutron is distributed to all nucleons, and the thermal equilibrium is realized which is the compound nucleus state. This idea has been considered to motivate Winger to introduce the random matrix theory (RMT) to nuclear physics.

Afterwards, the random matrix theory is developed by Wigner, Dyson, Mehta, Porter and other people, whose works are compiled in Ref. [74]. The RMT has been used to discuss the statistical properties of spectra of the complex strongly interacting systems. For example, measures of the fluctuation properties of spectra such as the nearest neighboring spacing of levels (NNS) and Δ_3 statistics can be determined by RMT.

In RMT, instead of considering a specific Hamiltonian of a particular system, one considers an ensemble of Hamiltonians which have the same symmetries, assuming some probability distribution for the matrix elements. According to the symmetries to be favored, there are several kinds of ensemble in RMT. In nuclear physics, the gaussian orthogonal ensemble (GOE) is often used corresponding to the time reversal symmetry. Random matrix theory is applied not only to nuclear physics but also to other fields[75, 76]. Relation to the quantum chaos is also discussed[77].

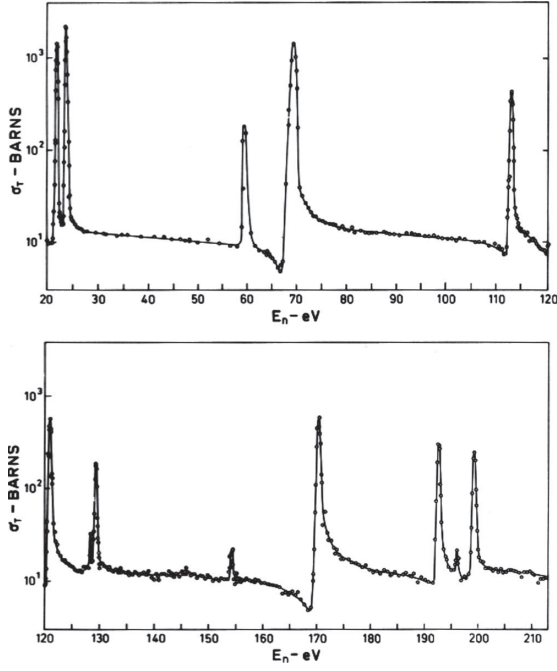


Figure 4.1: Neutron cross sections for ^{232}Th as a function of neutron energy. Taken from Ref. [56].

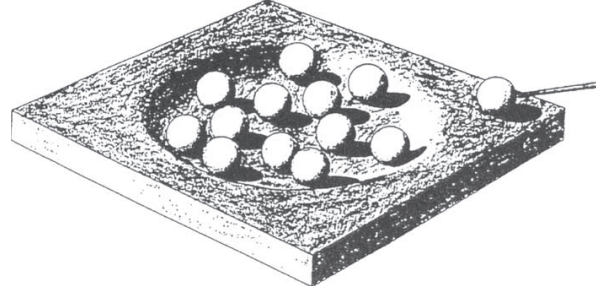


Figure 4.2: Bohr's Wooden toy model of compound nucleus. Taken from Ref. [73].

4.2 Gaussian orthogonal ensemble(GOE)

Hereafter, we consider assembly of levels with the same spin and the same parity. If a Hamiltonian is invariant under time reversal transformation, the Hamiltonian matrix can be chosen to be real. Thus the matrix elements satisfy

$$H_{\mu\nu} = H_{\nu\mu} = H_{\mu\nu}^*. \quad (4.1)$$

The volume element in the matrix space is defined by

$$d[H] = \prod_{\mu \leq \nu} dH_{\mu\nu}. \quad (4.2)$$

By assuming that (i) there is no correlation between the matrix elements not connected by the symmetry and (ii) the ensemble is invariant under the orthogonal transformation, one can obtain the following probability distribution function for the Hamiltonian matrix H

$$P(H)d[H] = N_0 \exp \left\{ -\frac{N}{4\lambda^2} \text{Tr}(H^2) \right\} d[H], \quad (4.3)$$

where N_0 is a normalization constant, λ is a parameter, and N is a dimension of the matrix space. If one applies the GOE to experimental data, λ is determined from the mean level density. From the

symmetry properties, the trace in the exponent satisfies

$$\text{Tr}(H^2) = \sum_{\mu, \nu} H_{\mu\nu} H_{\nu\mu} = \sum_{\mu, \nu} H_{\mu\nu}^2 = \sum_{\mu} H_{\mu\mu}^2 + 2 \sum_{\mu < \nu} H_{\mu\nu}^2 \quad (4.4)$$

and the distribution function is then written as

$$P[H]d[H] = N_0 \prod_{\mu} \exp\left\{-\frac{N}{4\lambda^2} H_{\mu\nu}^2\right\} dH_{\mu\mu} \prod_{\rho < \sigma} \exp\left\{-\frac{N}{2\lambda^2} H_{\rho\sigma}^2\right\} d_{\rho\sigma}. \quad (4.5)$$

From this form, one can deduce the following properties

$$\overline{H_{\mu\nu}} = 0 \quad (4.6)$$

$$\overline{H_{\mu\nu} H_{\rho\sigma}} = \frac{\lambda^2}{N} (\delta_{\mu\rho} \delta_{\nu\sigma} + \delta_{\mu\sigma} \delta_{\nu\rho}), \quad (4.7)$$

where the overline represents an ensemble average. The first equation means that the ensemble average of the matrix element is zero, and the second equation states that there is no correlation between the independent matrix elements. In fact, one can define GOE by a gaussian distribution function satisfying Eqs. (4.6) and (4.7), instead of the explicit distribution function (4.5).

If one adopts the eigenvalues and eigenvectors of the Hamiltonian as independent variables of the distribution function, Eq. (4.5) can be written as

$$P[H]d[H] = N_0 \exp\left\{-\frac{N}{4\lambda^2} \sum_{\mu} E_{\mu}^2\right\} \prod_{\rho < \sigma} |E_{\rho} - E_{\sigma}| \prod_{\nu} dE_{\nu} h(\theta_i) \prod_i d\theta_i, \quad (4.8)$$

where E_{μ} is the eigenvalues of the Hamiltonian, $\theta_i (i = 1, 2, \dots, N(N-1)/2)$ are the parameters characterizing the eigenvectors and, $h(\theta_i)$ is a function only of θ_i . One can see that the distribution function is written as the product of two parts which respectively depend only on the eigenvalues and the eigenvectors, that is, the eigenvalues and eigenvectors are uncorrelated independent variables. The factor $\prod_{\rho < \sigma} |E_{\rho} - E_{\sigma}|$ in this expression represents a level repulsion.

4.3 Properties of GOE

In this section, we review on the fundamental properties of GOE, that is, universality and ergodicity. First, we consider the mean level density in GOE. It is given by

$$\rho(E) = \sum_{\mu} \overline{\delta(E - E_{\mu})}, \quad (4.9)$$

which behaves as

$$\rho(E) = \begin{cases} \frac{N}{\pi\lambda} \sqrt{1 - \left(\frac{E}{2\lambda}\right)^2} & \text{for } |E| \leq 2\lambda \\ 0 & \text{for } |E| > 2\lambda \end{cases} \quad (4.10)$$

in the limit of $N \rightarrow \infty$. This is a half circle and this behavior is called the Wigner's half circle law. Since the actual nuclear level density exponentially increases according to the excitation energy, this behavior is not a physical one. However, this fact is not a problem because in using GOE, we are not interested in the global properties of the spectrum but in the local properties like the distribution of level spacing. Local property means the property in the energy scale which can be ignored compared to 4λ (diameter of the half circle) in the limit of $N \rightarrow \infty$. In this energy scale, the fluctuation properties of the spectrum is universal. That is, even if the ensemble does not have a gaussian functional form but has another cutoff, the local fluctuation measures are the same as that of GOE as long as the ensemble is orthogonally invariant and the spectrum appears in a finite range, while the overall shape of the spectrum is different. Thus, in the limit of $N \rightarrow \infty$, the local fluctuation measures are separated from global properties of the spectrum and are universal[78].

Next we discuss about ergodicity. In GOE, the fluctuation measures are obtained by taking an ensemble average of certain quantities. However, one may wonder whether it is meaningful to compare such quantities with the data obtained from physical system which is governed by a specific Hamiltonian. The ergodicity of GOE gives an answer to this question. Experimentally obtained spectral data can be used for the calculation of quantities such as the distribution of nearest neighbouring spacing by averaging over the spectrum. We denote an average of a quantity O over the spectrum by $\langle O \rangle$. If $\overline{O} = \langle O \rangle$ holds for all members of the ensemble and for all quantities O describing local fluctuation, one can meaningfully compare the results from GOE and the data. Although this relation has not been proved, a weaker claim

$$\overline{(\overline{O} - \langle O \rangle)^2} = 0 \quad (4.11)$$

has been proved, that is, for almost all members of the ensemble, an averages of O over the ensemble and that over the spectrum are the same. This property is call ergodicity.

4.4 Fluctuation measures of GOE

We introduce three famous fluctuation measures of GOE. At first, we introduce the distribution of nearest neighbouring spacing (NNS) of levels. Although the distribution function cannot be written in a closed form, it is nicely approximated by a Wigner distribution

$$P(s) = \frac{\pi}{2} s e^{-\frac{\pi}{4} s^2}, \quad (4.12)$$

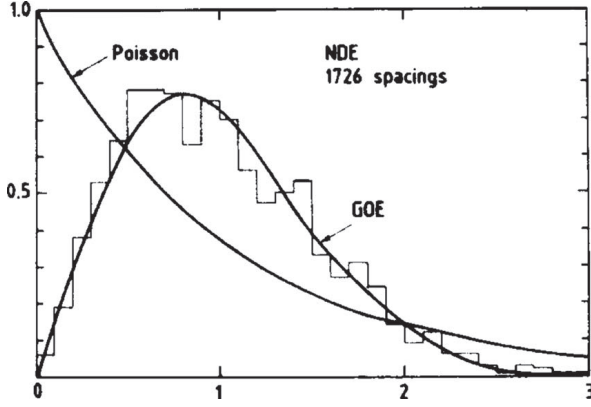


Figure 4.3: Comparison of NNS distribution for GOE and Nuclear Data Ensemble (NDE). Taken from Ref. [84]. A Poisson distribution is also shown.

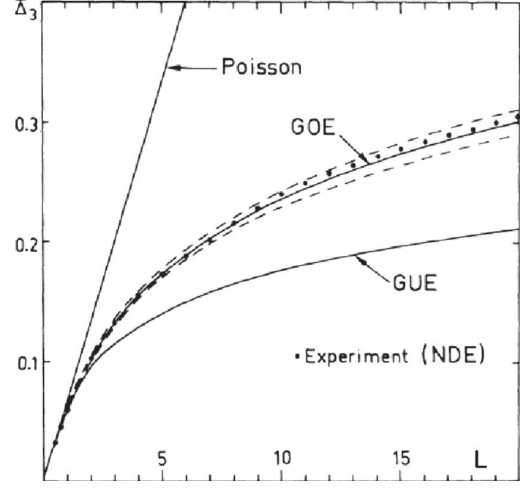


Figure 4.4: Comparison of Δ_3 statistics for GOE and NDE. The Δ_3 statistics for GUE (Gaussian Unitary ensemble) and Poisson distribution are also shown. Taken from Ref. [85].

where, the parameter s is the level spacing divided by the mean level spacing. For small s , $P(s)$ is proportional to s , and this indicates a level repulsion. If there is no correlation among levels, the distribution is given by a Poisson distribution which has a peak at $s = 0$. The level repulsion of GOE represents strong correlation among levels. In Fig.4.3, we show the comparison of NNS distribution from GOE and experimental data. The data is obtained by compiling the data from neutron resonances and proton resonances, and is called Nuclear Data Ensemble (NDE)[84]. A Poisson distribution is also shown. One can see that the distribution of GOE reproduces that of NDE well.

Next we introduce the Δ_3 statistics which represents the correlation of level spacing. We define the following function

$$N(E) = \int_{-\infty}^E dE' \sum_{\mu} \delta(E' - E_{\mu}). \quad (4.13)$$

This represents a number of levels below the energy E . Using $N(E)$, the Δ_3 statistics is defined by

$$\Delta_3(L) = \min_{a,b} \frac{1}{L} \left\langle \int_{E_0}^{E_0+L} dE' \overline{[N(E') - a - bE']^2} \right\rangle, \quad (4.14)$$

where, $\langle \rangle$ represents an average with respect to E_0 . $\Delta_3(E)$ behaves logarithmic increase for large L

$$\Delta_3(E) \approx \frac{1}{\pi^2} (\ln L - 0.0678). \quad (4.15)$$

Comparison of this quantity from GOE and NDE is given in Fig.4.4. In the figure, the Δ_3 statistics

from the gaussian unitary ensemble (GUE) and the Poisson distribution are also shown. One can see that the GOE reproduces the data.

Finally, we introduce a Porter-Thomas distribution which corresponds to the distribution of eigenvectors. Let ψ be the projection of an eigenvector of a Hamiltonian in GOE on to some axis in Hilbert space. The quantity $y = \psi^2 / \overline{\psi^2}$ obeys the, Porter-Thomas distribution given by

$$P(y) = \frac{1}{\sqrt{2\pi y}} e^{-\frac{y}{2}}. \quad (4.16)$$

This distribution is compared with, for instance, the transition probability to a final state of nuclear levels or the width of the decay to a final state, because these quantities are proportional to the absolute square of the matrix elements containing the wave function.

4.5 Random matrix theory for deep inelastic collision

In the previous sections, we have reviewed general aspects of RMT. In this section, we review the application of RMT to deep inelastic collision by Agassi, Ko, and Weidenmüller in the 1970's[44, 45, 46, 47, 48, 49, 50]. A similar model is employed in Ref. [86] for the study of dissipation in collective motion of a quantum many-body system.

In the 1970's, heavy-ion reactions in the energy region of a few million electron volt per nucleon had revealed a new form of reaction not classified either to a direct reaction or to a compound nucleus reaction. It exhibits large dissipation of the kinetic energy into the energy of intrinsic excitations and is called deep inelastic collision (DIC). Classical models employing a friction force has been used for the description of DIC. Weidenmüller and his collaborators developed a random matrix model aiming to describe DIC in a more microscopic point of view. They took advantage of the complex nature of the highly excited states relevant to DIC, that is, they imposed a statistical random matrix assumption for the coupling matrix which couples the relative motion and the intrinsic excitations. Based on RMT, they assumed the following condition for the second moment of the coupling matrix elements between the intrinsic states $|nIM\rangle$

$$\begin{aligned} & \overline{\langle nIM | V_{\text{coup}}(\mathbf{r}) | n'I'M' \rangle \langle n''I''M'' | V_{\text{coup}}(\mathbf{r}') | n'''I'''M''' \rangle} \\ &= \{ \delta_{nn''} \delta_{n'n'''} \delta_{II''} \delta_{I'I'''} + \delta_{nn'''} \delta_{n'n''} \delta_{II'''} \delta_{I'I''} \} \sum_{\lambda} \sum_{\mu, \mu'} \frac{4\pi}{2\lambda + 1} Y_{\lambda\mu}(\hat{\mathbf{r}}) Y_{\lambda\mu'}^*(\hat{\mathbf{r}}') \\ & \times (-1)^{M'-M''} (-1)^{I+\lambda+I'} \sqrt{(2I+1)(2I'+1)} \begin{pmatrix} I & \lambda & I' \\ M & \mu & -M' \end{pmatrix} \begin{pmatrix} I' & \lambda & I \\ -M'' & \mu' & M''' \end{pmatrix} \\ & \times \alpha_{\lambda}(n, n'; I, I'; r, r'). \end{aligned} \quad (4.17)$$

Here, the form factor α_λ is parameterized as

$$\alpha_\lambda(n, n'; I, I'; r, r') = \frac{w_\lambda}{\sqrt{\rho(n, I)\rho(n', I')}} e^{-\frac{(\epsilon_n - \epsilon_{n'})^2}{2\Delta^2}} e^{-\frac{(r - r')^2}{2\sigma^2}} f\left(\frac{r + r'}{2}\right), \quad (4.18)$$

where $\rho(n, I)$ is a level density with spin I at excitation energy ϵ_n and f is a some function. The derivation of Eq. (4.17) is explained in Sec. 6.2. We only mention here that the level density appears in the denominator of the form factor reflecting the complexity of the excited states. As the excitation energy increases, the wave function of the excited states becomes more and more complex and exhibits oscillatory behavior. As a consequence, the overlap of the wave functions decreases as the excitation energy increases. This feature is represented by the level density in the form factor. This model was justified in Ref. [46] based on shell-model consideration, from which the values of the parameters in the model were also estimated.

Instead of solving the coupled-channels equations quantum mechanically, Weidenmüller *et al.* reduced the coupled-channels equations to classical transport equations. They first applied the model to one-dimensional problem [48] and then applied to realistic systems[49, 50]. In Figs. 4.5 and 4.6, their results are shown. Fig. 4.5 shows a comparison of differential cross sections for light fragments emitted in a ^{84}Kr -induced reaction at various energies. The solid lines show the data and the dashed lines show their calculation[50]. Fig. 4.6 shows the differential cross section for $^{209}\text{Bi} + ^{136}\text{Xe}$ reaction for various atomic number of the fragments. The dots represent the data and the dashed lines show their calculation[50]. Their calculations qualitatively reproduce the data and they concluded that the essential part of DIC is well described by their model. We will employ their model for the study of the role of noncollective excitations in heavy-ion reactions in chapter 7.

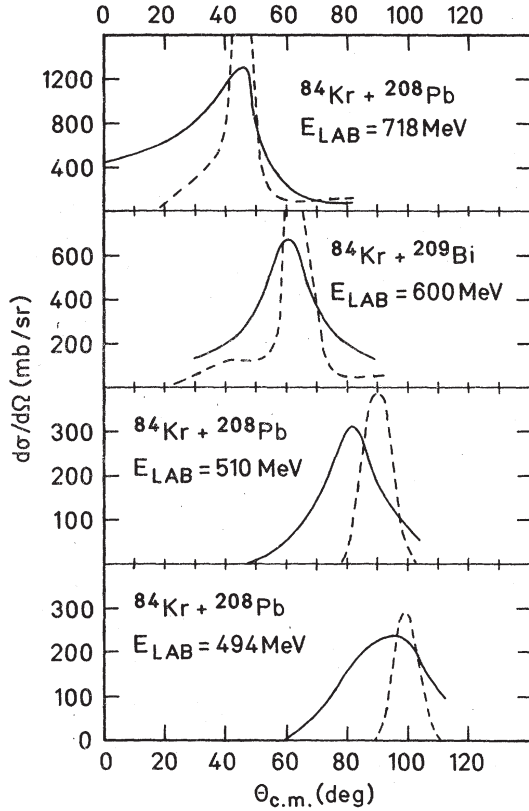


Figure 4.5: Differential cross sections for the light fragments emitted in ^{84}Kr -induced reactions. The solid lines show the experimental data and the dashed lines show the results of the Weidenmüller's calculation based on RMT. Taken from Ref. [50].

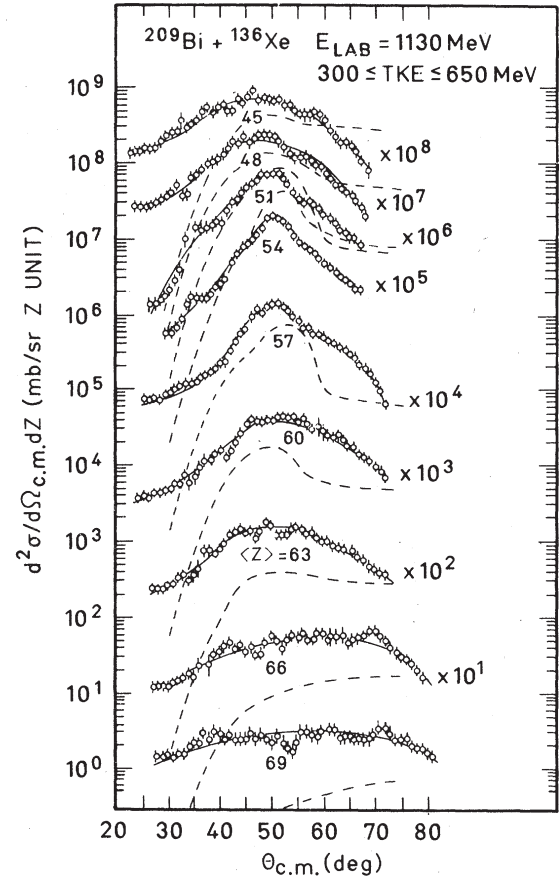


Figure 4.6: Angular distribution of fragments in the reaction of $^{136}\text{Xe} + ^{209}\text{Bi}$, integrated over the energy of fragments as indicated. $\langle Z \rangle$ is an atomic number of fragments. The dots show the data and the dashed lines show the results of the calculation. Taken from Ref. [50]

Chapter 5

Noncollective excitations in $^{16}\text{O} + ^{208}\text{Pb}$ reaction

In this chapter, we discuss the role of noncollective excitation of ^{208}Pb in $^{16}\text{O} + ^{208}\text{Pb}$ reaction at energies around the Coulomb barrier[51]. This system has been extensively studied both experimentally and theoretically. Using the information on the noncollective excited states in ^{208}Pb , we describe the noncollective excitations in the $^{16}\text{O} + ^{208}\text{Pb}$ reaction and investigate their effects on the reaction observables.

5.1 Current status of $^{16}\text{O} + ^{208}\text{Pb}$ reaction

The $^{16}\text{O} + ^{208}\text{Pb}$ system has been studied both from the theoretical and experimental sides. The fusion cross sections for this system have been measured at subbarrier and above barrier energies[28], as well as at deep subbarrier energies[17]. The coupled-channels analysis has also been performed. Although a careful analysis has been performed by taking into account vibrational excitations in ^{16}O and ^{208}Pb nuclei, the experimental fusion barrier distribution has not been well reproduced theoretically. In Fig. 5.1, we show the barrier distributions for $^{16}\text{O} + ^{208}\text{Pb}$ system given in Ref. [28]. The calculated barrier distributions are compared with the experimental data. In these calculations, phonon excitations of ^{208}Pb are taken into account, including also the anharmonicity of the phonon excitations (see the solid lines). In Fig. 5.1(b), the excitation energy of the 3^- state and the coupling strength for the 2-phonon states are reduced. As one can see, the coupled-channels calculation overestimates the height of the main peak in the barrier distribution. Not only fusion experiments, but also the experiments for quasi-elastic scattering have been performed and the quasi-elastic barrier distribution has been extracted[23, 24, 25, 26]. In addition, the energy dependence of the Q-value distribution is obtained at subbarrier energies. The experimental data of Ref. [25] for the Q-value distribution has already been shown in Fig. 1.4. The experimental data show that the contribution from the inelastic scattering of higher excitation energy (Q-value) becomes more and more important as the incident energy increases, while at the lowest incident energy, the contribution from the

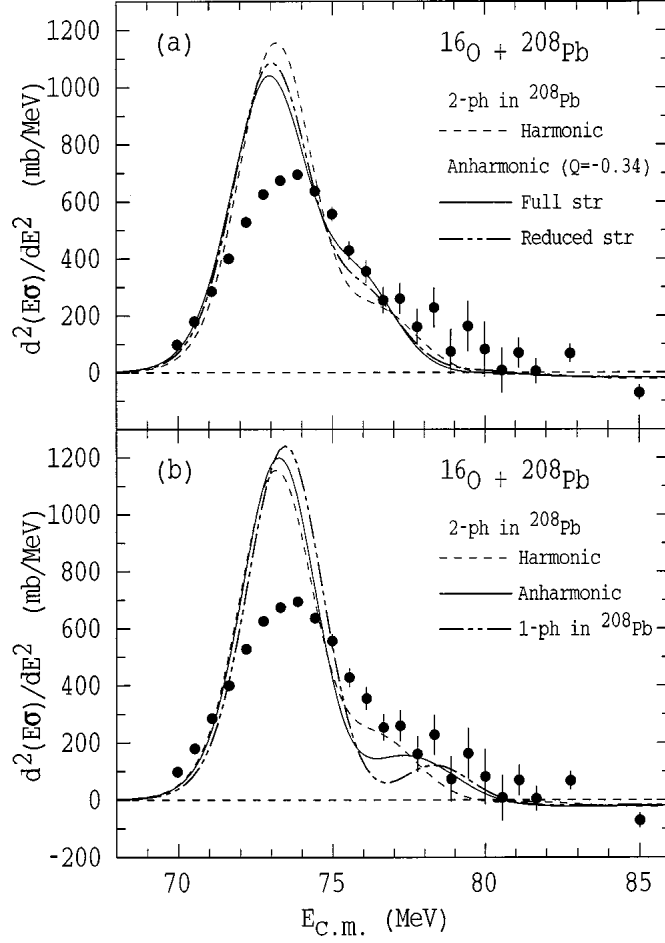


Figure 5.1: Fusion barrier distribution for $^{16}\text{O} + ^{208}\text{Pb}$ system. Taken from Ref. [28]. The dots represent the experimental data, and lines are the results of the coupled-channels calculation. These calculation includes phonon excitations of ^{208}Pb . Anharmonicity of the phonon excitations is taken into account in the solid lines. The solid line in the figure (b) assumes the smaller excitation energy than the physical value and the reduced coupling strength for 2-phonon states from the harmonic limit.

elastic channel is dominant. As can be seen from the spectrum of ^{208}Pb shown in Fig. 2.4, these higher-lying excitations are noncollective excitations. Since the conventional coupled-channels calculations take into account only the low-lying collective excitations, they do not yield the Q-value spectra at higher excitation energies, and thus the behavior of the experimental Q-value distribution cannot be accounted for by the conventional calculations.

For ^{208}Pb nucleus, the information on the excited states has been obtained from high precision proton inelastic scattering experiments[42, 43] up to rather high excitation energies. In fact, the excitation energy, spin, parity and deformation parameter are identified with a DWBA analysis for almost all excited states up to 7.5 MeV. We can use these information to describe the noncollective excitations in $^{16}\text{O} + ^{208}\text{Pb}$ reaction. By taking into account the noncollective excitations in $^{16}\text{O} + ^{208}\text{Pb}$ fusion and quasi-elastic scattering, we investigate in this chapter whether the noncollective excitations can improve the agreement of the barrier distribution with the experimental data. We

also calculate the energy dependence of the Q-value distribution and see whether the tendency of the experimental data can be reproduced.

5.2 Results

We now numerically solve the coupled-channels equations for the $^{16}\text{O} + ^{208}\text{Pb}$ reaction. For the coupling to the collective excitations, we take into account the vibrational 3^- state at 2.615 MeV, 5^- state at 3.198 MeV, and 2^+ state at 4.085 MeV in ^{208}Pb (see Table 2.1) as well as the 3^- state at 6.13 MeV in ^{16}O . The deformation parameters are estimated from the measured electromagnetic transition probabilities, that is, $\beta_3(^{208}\text{Pb}) = 0.122$, $\beta_5(^{208}\text{Pb}) = 0.058$, $\beta_2(^{208}\text{Pb}) = 0.058$, and $\beta_3(^{16}\text{O}) = 0.733$, together with a radius parameter of $r_0 = 1.2$ fm. In addition to these collective vibrational states, we also include 70 noncollective states in ^{208}Pb below 7.382 MeV (see Fig. 2.4), whose excitation energies, multipolarities, and deformation parameters are taken from the high-resolution proton inelastic scattering measurements in Ref. [42]. We take into account the mutual excitations of the ^{208}Pb and the ^{16}O nuclei.

For the nuclear potential, we use the same geometry as that in Ref. [25], where the parameters were obtained by fitting the coupled-channels calculations to the experimental quasi-elastic scattering cross sections. This potential has a surface diffuseness parameter of $a = 0.671$ fm and uses the radius parameter of $R = 8.39$ fm. Since our calculation takes into account the 3^- state in ^{16}O , that was not included in Ref. [25], we modify the potential depth from 853 MeV to 550 MeV in order to compensate the adiabatic potential renormalization (see section 3.6.3) [40]. For the form factors of the noncollective couplings, for simplicity we take the same geometry as that for the collective couplings. For the noncollective excitations, we include only the couplings from the ground state, and neglect the couplings among the noncollective excitations as well as the couplings between the collective and the noncollective states.

5.2.1 Single phonon calculation

We first show the results for the calculation that takes into account only the single octupole phonon state in the ^{208}Pb together with the other collective and the noncollective states. In this case, the number of channels amounts to 146 in the isocentrifugal approximation.

Figures 5.2(a) and 5.2(b) show the fusion cross sections thus obtained. They are plotted both on the linear scale (Fig. 5.2(a)) and on the logarithmic scale (Fig. 5.2(b)). The corresponding barrier distributions, $D_{\text{fus}} = d^2(E\sigma_{\text{fus}})/dE^2$, are plotted in Fig. 5.2(c). The experimental data are taken from Refs. [28, 17]. The dashed lines are obtained by taking into account only the collective excitations of ^{208}Pb and ^{16}O , while the dot-dashed lines take into account also the noncollective excitations of ^{208}Pb . One immediately sees that the main peak in the barrier distribution is shifted in energy due to the noncollective excitations towards low energy and consequently the fusion cross sections

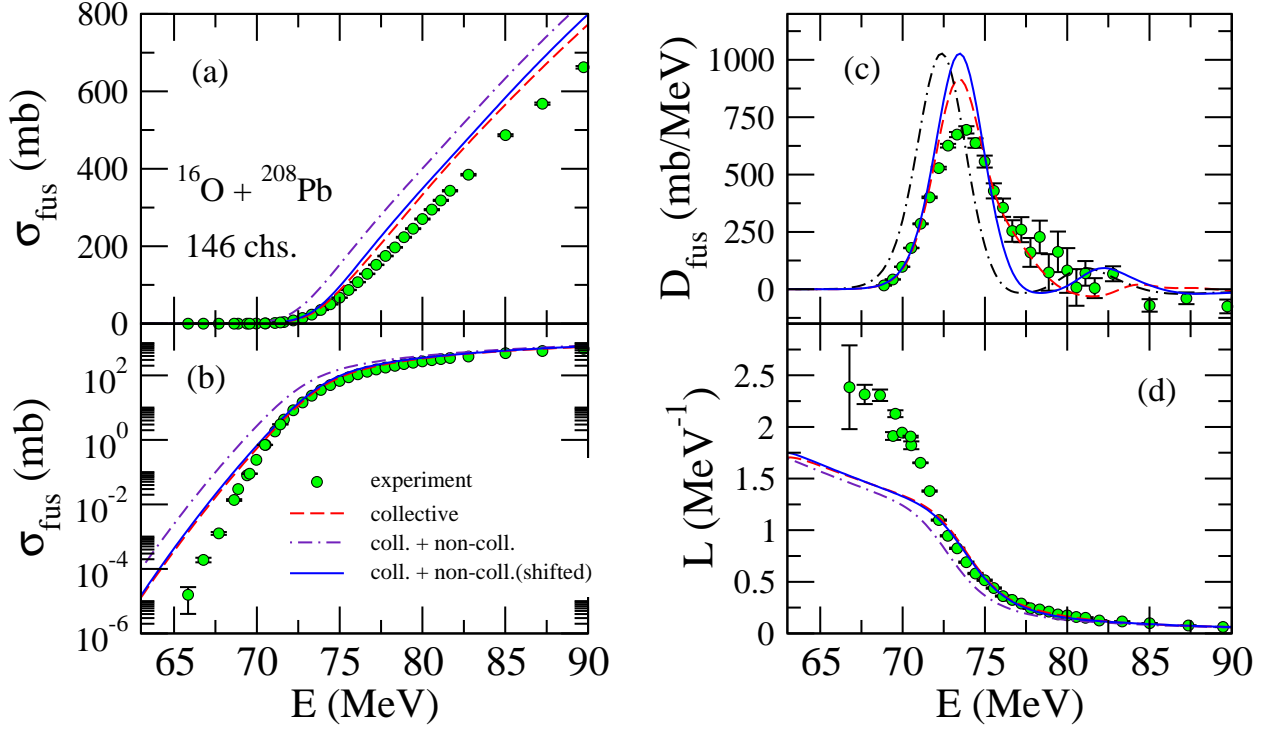


Figure 5.2: The fusion cross sections (Fig. 5.2(a) and 5.2(b)), the fusion barrier distribution, $D_{\text{fus}} = d^2(E\sigma_{\text{fus}})/dE^2$, (Fig. 5.2(c)), and the logarithmic slope, $L(E) = d[\ln(E\sigma_{\text{fus}})]/dE$, (Fig. 5.2(d)), for the $^{16}\text{O} + ^{208}\text{Pb}$ reaction. The fusion cross sections are plotted both on the linear and logarithmic scales in Figs. 5.2(a) and 5.2(b), respectively. The dashed lines are obtained by taking into account only the collective excitations of ^{16}O and ^{208}Pb , while the dot-dashed lines take into account the noncollective excitations of ^{208}Pb in addition to the collective excitations. The solid lines are the same as the dot-dashed lines, but shifted in energy. The experimental data are taken from Refs. [28, 17].

are enhanced. This can be understood in terms of the adiabatic potential renormalization because the excitation energies for the noncollective excitations are relatively large. One can also see that the noncollective excitations do not alter much the energy dependence of the fusion cross sections, as can be seen more clearly by shifting the dot-dashed lines in energy as shown in Fig. 5.2 by the solid lines. As a consequence, the noncollective excitations hardly modify the behavior of the logarithmic slope, $L(E) = d[\ln(E\sigma_{\text{fus}})]/dE$ (see Fig. 5.2(d)). That is, the calculations with only the collective excitations do not account for the observed large logarithmic slope at deep subbarrier energies. This remains the same even if the noncollective excitations are taken into account. This indicates that the deep sub-barrier hindrance of fusion cross sections cannot be explained simply with the noncollective excitations in each of the colliding nuclei, and some other mechanism, such as noncollective excitations of the one-body system after the touching of the colliding nuclei, has to be considered [87].

As mentioned in Sec. I, it is known that the calculation with only collective excitations does not reproduce well the experimental barrier distribution for this system [28]. That is, the coupled-channels calculation yields a too high main peak in the barrier distribution. We find that the non-

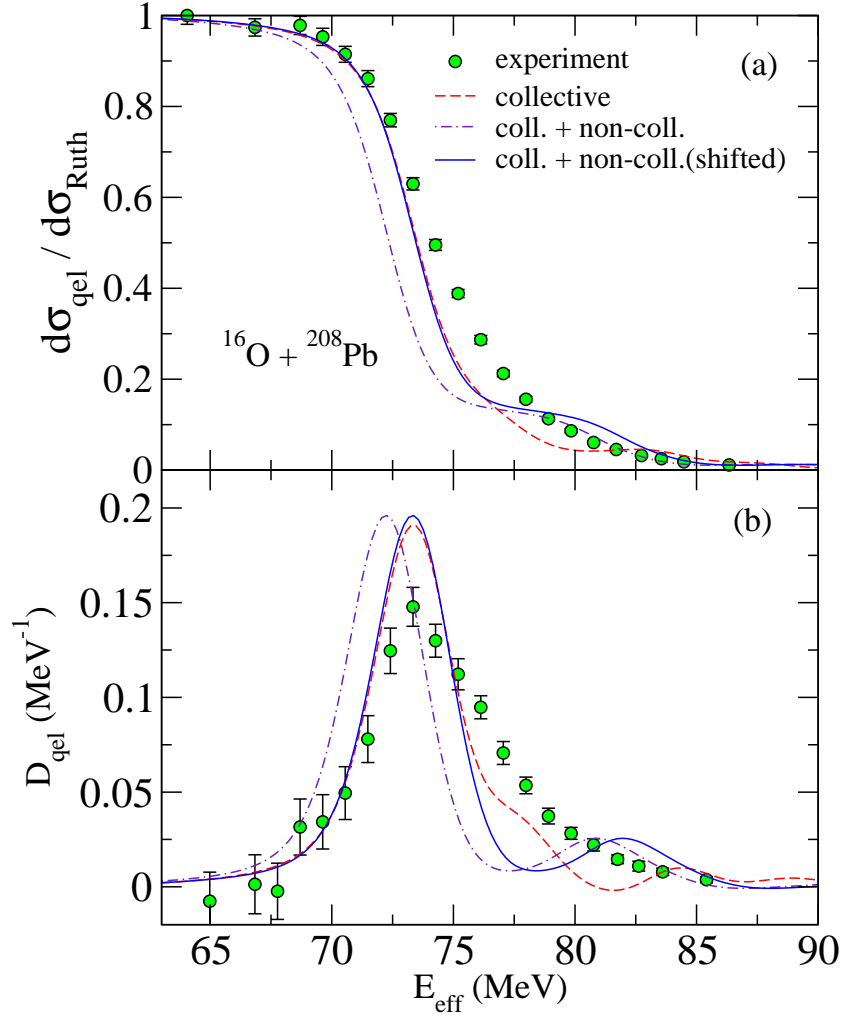


Figure 5.3: Quasi-elastic scattering cross sections (Fig. 5.3(a)) and the quasi-elastic barrier distribution (Fig. 5.3(b)) for the $^{16}\text{O} + ^{208}\text{Pb}$ system. The meaning of each line is the same as in Fig. 5.2. The experimental data are taken from Ref. [23].

collective excitations are not helpful in this respect, as shown in Fig. 5.2(c). The noncollective excitations rather smear the barrier distribution at energies around 78 MeV [88], and the agreement is somewhat worsened. Clearly, one needs other mechanisms in order to reproduce the experimental barrier distribution for this system. In this connection, in the next subsection, we will investigate the effect of double octupole phonon excitations in ^{208}Pb .

Figure 5.3 shows the quasi-elastic scattering cross section and the quasi-elastic barrier distribution, $D_{\text{qel}}(E) = d[\sigma_{\text{qel}}/\sigma_{\text{R}}]/dE$ at $\theta_{\text{cm}} = 170^\circ$. E_{eff} is the effective energy defined by Eq. (3.47), which takes into account the centrifugal energy for the Rutherford trajectory. The meaning of each line is the same as in Fig. 5.2. The solid lines are shifted in energy with the same amount as in the fusion calculation. The experimental data are taken from Ref. [23].

One can observe that the change in the barrier distribution due to the noncollective excitations is similar to the fusion calculation. That is, the main effect of the noncollective excitations is the barrier renormalization without changing the shape of the distribution, although they smear the

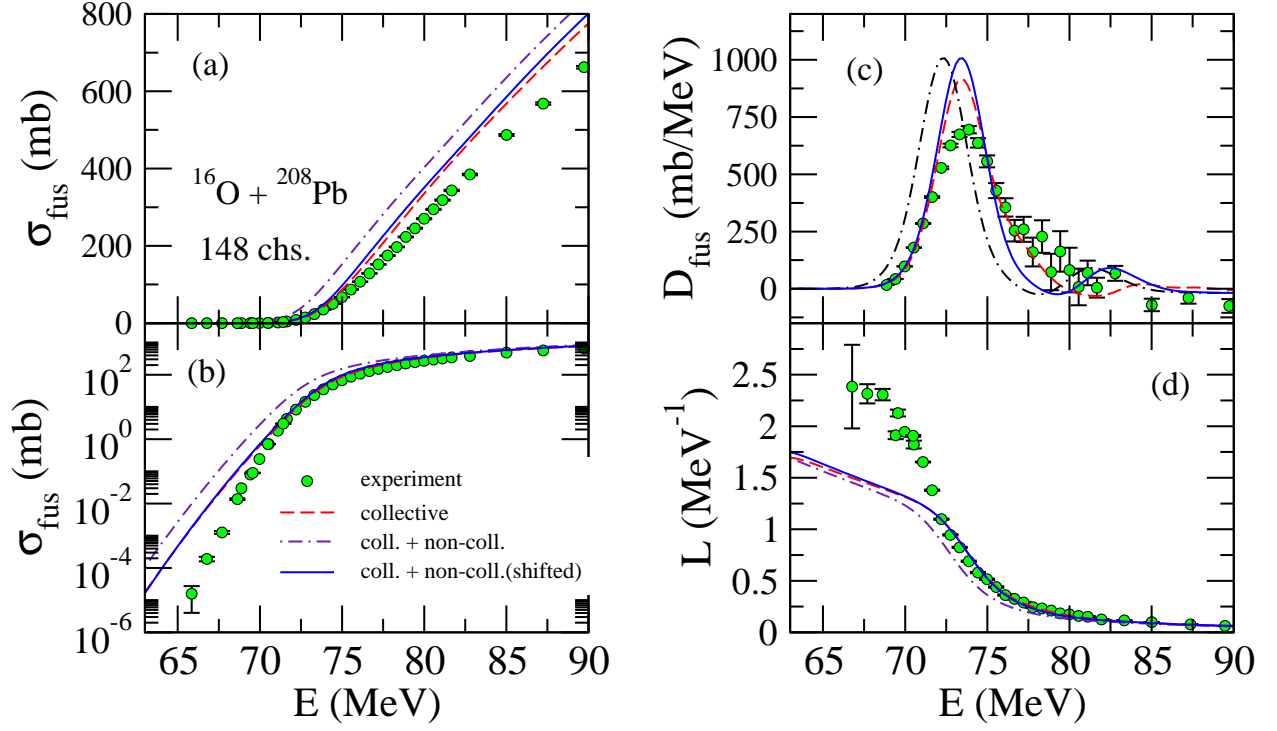


Figure 5.4: Same as Fig. 5.2, but with the double octupole phonon excitations.

barrier distributions at relatively higher energies. The agreement with the experimental data around $E_{\text{eff}} = 75$ MeV is not improved by the noncollective excitations.

5.2.2 Double phonon calculation

We next show the results for the calculations with the double octupole phonon excitations in ^{208}Pb . In this case, the number of channels included amounts to 148. The double octupole phonon states in ^{208}Pb have been experimentally investigated in Refs. [58, 59, 60, 61, 62] and candidates for the double phonon have been identified. In the present calculation we assume, for simplicity, that all four double octupole phonon states are degenerate with $E=5.23$ MeV, that is, twice the energy of the single-phonon state.

In Figs. 5.4 and 5.5, we show the calculations for the fusion reaction and quasi-elastic scattering, respectively. One sees that the double phonon excitations leads only to a minor improvement both for fusion and quasi-elastic scattering. The effects of the noncollective excitations are similar to those in the single-phonon case presented in the previous subsection. That is, the barrier distribution is smeared above the barrier while the shape of the lower peak is almost unchanged.

5.2.3 Anharmonicity of octupole phonon state in ^{208}Pb

We have also investigated the role of anharmonicity of the octupole phonon excitations of ^{208}Pb [9, 10], together with the noncollective excitations. We assume that the physical octupole phonon state

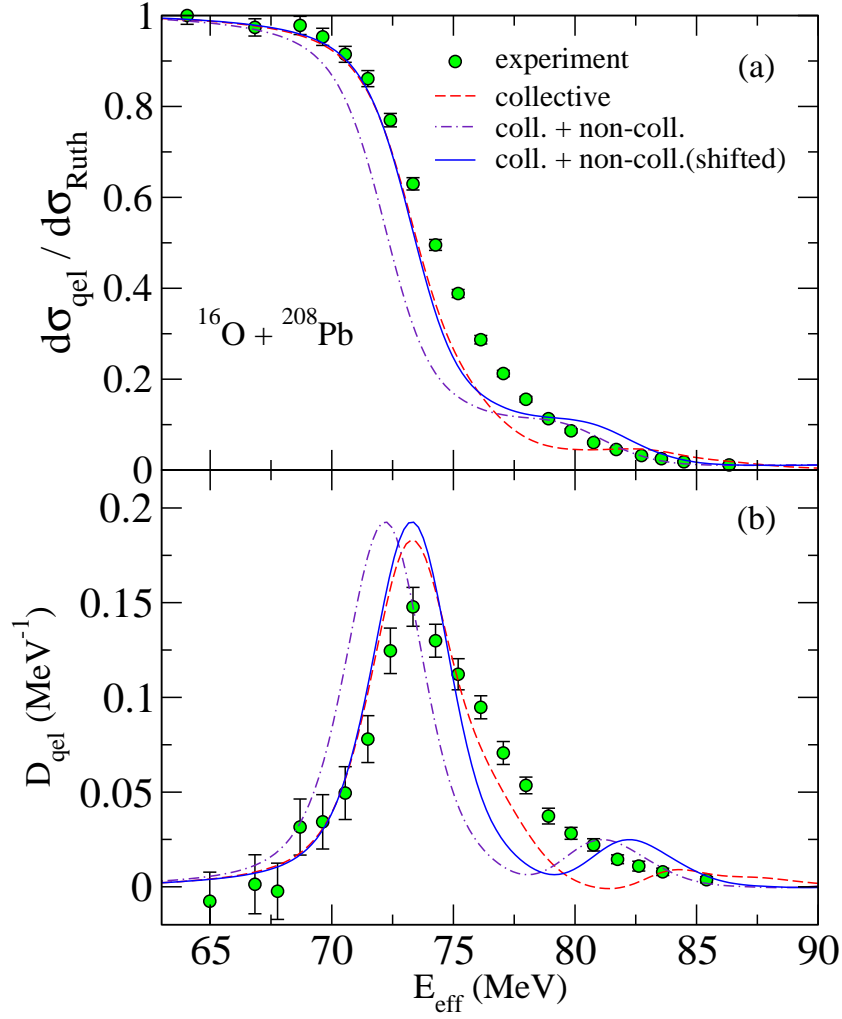


Figure 5.5: Same as Fig. 5.3, but with the double octupole phonon excitations.

at $E = 2.615$ MeV is made from the harmonic octupole and quadrupole phonons, that is,

$$|3^-\rangle = \frac{1}{\sqrt{1+\alpha^2}} \left(a_{30}^\dagger + \alpha [a_2^\dagger a_3^\dagger]^{(30)} \right) |0\rangle. \quad (5.1)$$

Here, α is a constant and is determined from the quadrupole moment of the octupole phonon state.

The quadrupole moment is calculated as

$$Q_2(3^-) = \sqrt{\frac{16\pi}{5}} \langle 33 | Q_{20} | 33 \rangle = \frac{3}{15\pi} e Z_T R_T^2 \beta_2 \alpha \quad (5.2)$$

or

$$\alpha = \frac{\sqrt{15\pi}}{3e Z_T R_T^2 \beta_2} Q_2(3^-). \quad (5.3)$$

The quadrupole moment $Q_2(3^-)$ has been measured experimentally to be $Q_2(3^-) = -34 \pm 15 e \text{ fm}^2$ [52, 53]. With $\beta_2 = 0.058$, α is then calculated with Eq. (5.3) to be -0.37 .

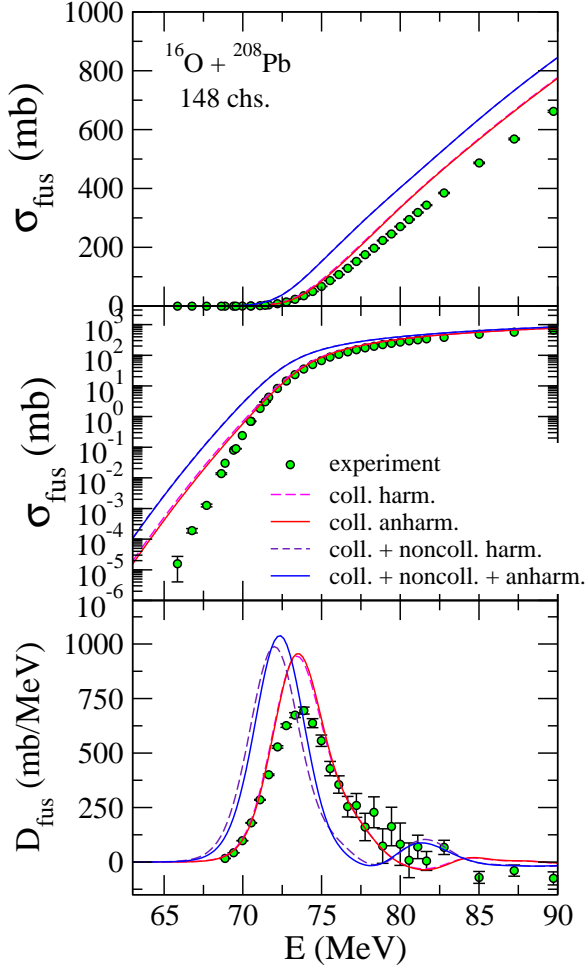


Figure 5.6: Fusion cross section and barrier distribution for $^{16}\text{O} + ^{208}\text{Pb}$ system. The dashed lines are the results in the harmonic limit, while the solid lines take into account anharmonicity. The pink and the red lines include only the collective excitations and the purple and the blue lines include the noncollective excitations.

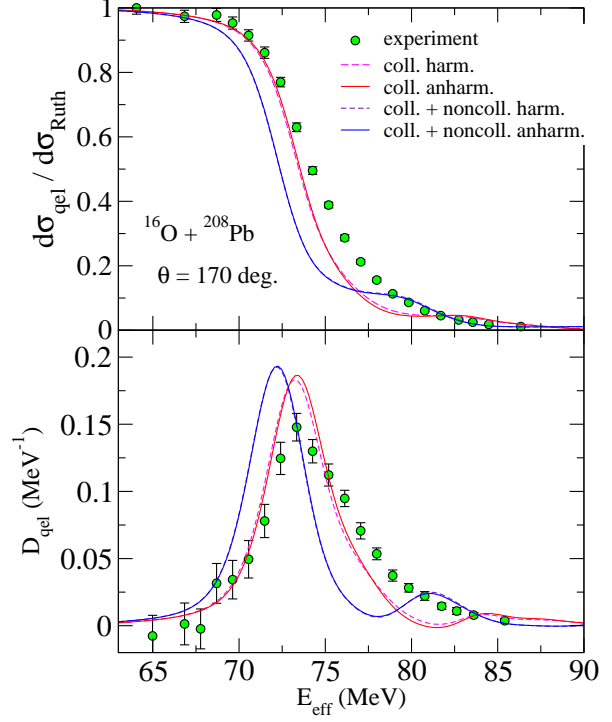


Figure 5.7: Same as Fig. 5.6, but for quasi-elastic scattering.

In the presence of the anharmonicity, 3^- state can couple to 2^+ state and 3^- state itself (reorientation) even in the linear order in β_λ . In fact, the matrix elements of \hat{O} defined in (3.93) is given by

$$\langle 2^+ | \hat{O} | 3^- \rangle = \frac{\alpha}{\sqrt{1 + \alpha^2}} \frac{R_T \beta_3}{\sqrt{4\pi}} \langle 2030 | 30 \rangle \quad (5.4)$$

$$\langle 3^- | \hat{O} | 3^- \rangle = \frac{2\alpha}{1 + \alpha^2} \frac{R_T \beta_2}{\sqrt{4\pi}} \langle 2030 | 30 \rangle. \quad (5.5)$$

In Figs. 5.6 and 5.7, the results for the fusion reaction and the quasi-elastic scattering are shown respectively. These calculations correspond to the double phonon calculation. The pink and the red lines include only the collective excitations and the purple and the blue lines take into

account the noncollective excitations in addition to the collective excitations. The dashed lines are the results in the harmonic limit, and thus the same as Figs. 5.4, and 5.5. The solid lines take into account the anharmonicity. We can see that the effect of the anharmonicity is quite subtle both in the fusion reaction and the quasi-elastic scattering cases, regardless of the presence of the noncollective excitations. Hence the improvement of the agreement with the data is not obtained with the effect of anharmonicity.

5.2.4 Q-value distribution

Measurements of the Q-value distribution for backward-angle quasi-elastic scattering have been performed for this system [25, 26], in which the experimental data indicate that the contribution from the noncollective excitations increases as the incident energy increases. A big advantage of our method is that the Q-value distribution can be computed easily because we explicitly take into account the noncollective excitations in our coupled-channels calculations.

Figure 5.8 shows the Q-value distributions at $\theta_{\text{cm}} = 170^\circ$ at six different incident energies, corresponding to the double phonon calculations shown in Sec. 5.2.2. The spectra shown by the dashed lines correspond to the collective excitations while those by the solid lines correspond to the noncollective excitations. The envelope of the spectra is obtained by smearing with a gaussian function,

$$F(E^*) = \sum_n \frac{d\sigma_n}{d\Omega} \frac{1}{\sqrt{2\pi}\Delta} e^{-\frac{(E^* - \epsilon_n)^2}{2\Delta^2}}, \quad (5.6)$$

with $\Delta = 0.2$ MeV.

Note that we include the noncollective states of ^{208}Pb up to 7.382 MeV. Thus the spectra above this energy correspond to mutual excitations of the ^{208}Pb and ^{16}O nuclei. One can see that, at the lowest incident energy shown in the figure, the contribution from the collective channels is dominant. With increasing energy, the contribution from the noncollective excitations becomes more and more important. This behaviour is qualitatively consistent with the experimental Q-value distribution for this system [25, 26].

Note that this energy dependence is also related to how the noncollective excitations modify the energy dependence of the barrier distribution. Namely, at low energies where the contribution from the noncollective excitations is not important, a change in the barrier distribution is not observed. On the other hand, at higher energies where the contribution from the noncollective excitations is important, the barrier distribution is smeared due to the noncollective excitations.

5.2.5 Mass-number dependence of the effect of noncollective excitations

Finally, we investigate how the effect of noncollective excitations depends on the mass number of the projectile nucleus. For this purpose, we solve the coupled-channels equations for the $^{32}\text{S} + ^{208}\text{Pb}$

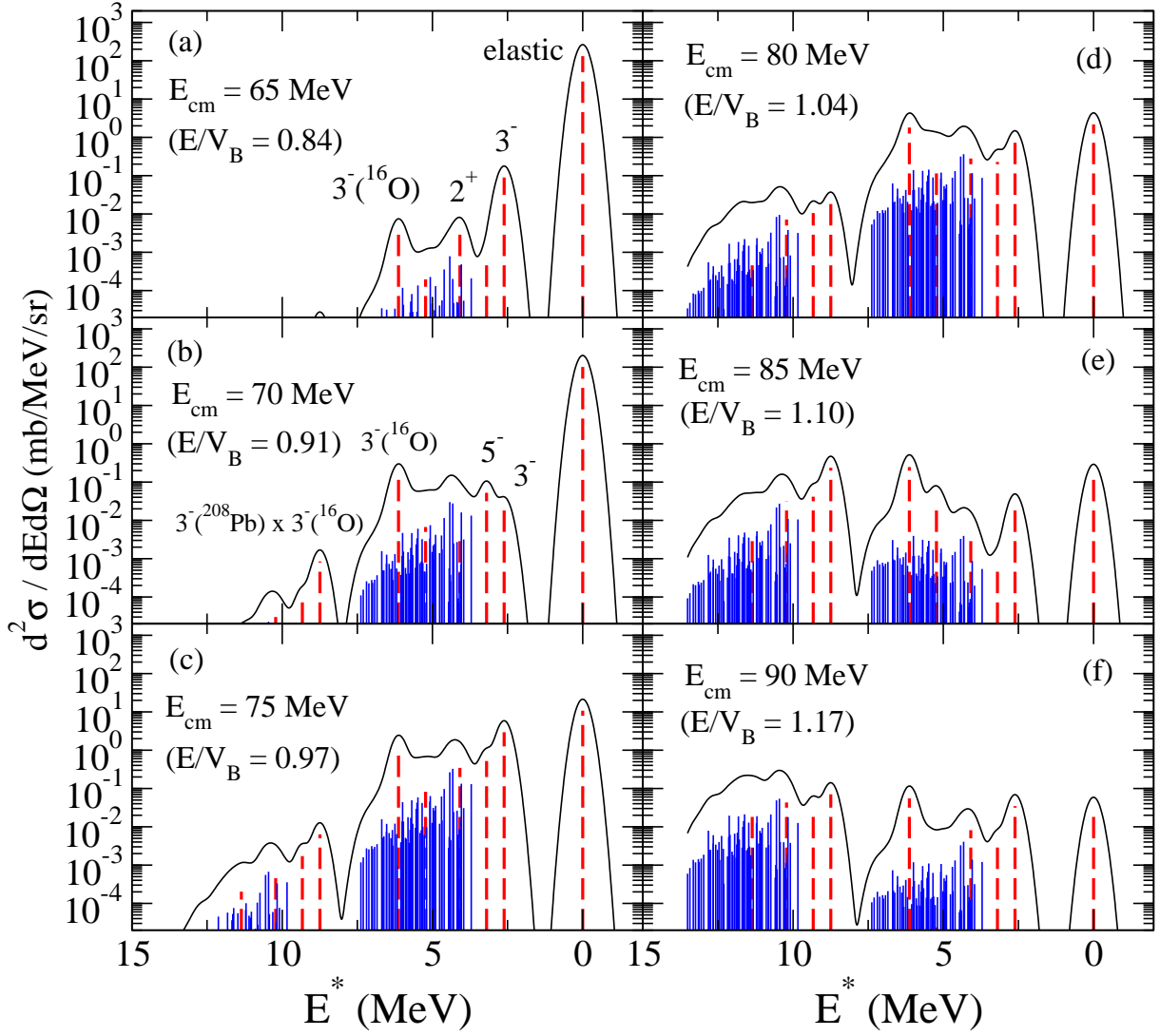


Figure 5.8: The Q-value spectra for the quasi-elastic scattering at $\theta_{c.m.}=170^\circ$ for the $^{16}\text{O} + ^{208}\text{Pb}$ system for six different incident energies. The dashed peaks correspond to the collective excitations while the solid peaks correspond to the noncollective excitations. The solid line is obtained by smearing the peaks with a gaussian function.

and $^{40}\text{Ca} + ^{208}\text{Pb}$ systems. For the nuclear potential, we use the Akyüz-Winther potential [89]. We include the same excited states in the ^{208}Pb nucleus as those in the calculation for the $^{16}\text{O} + ^{208}\text{Pb}$ system discussed in the previous subsections.

We first discuss the $^{32}\text{S} + ^{208}\text{Pb}$ reaction. For the excitations of ^{32}S , we take into account the quadrupole vibration up to the double phonon states. The excitation energy and the deformation parameter are taken from Ref. [90]. Figure 5.9 shows the calculated fusion cross section and fusion barrier distribution. The meaning of each line is the same as in Fig. 5.2. The experimental data are taken from Ref. [23]. One can see that the effect of the noncollective excitations is qualitatively similar to that in the $^{16}\text{O} + ^{208}\text{Pb}$ reaction. That is, the barrier is shifted towards lower energy and the higher part of the barrier distribution is smeared. However, the smearing is stronger than that in the $^{16}\text{O} + ^{208}\text{Pb}$ system, because an effective coupling strength is in general approximately

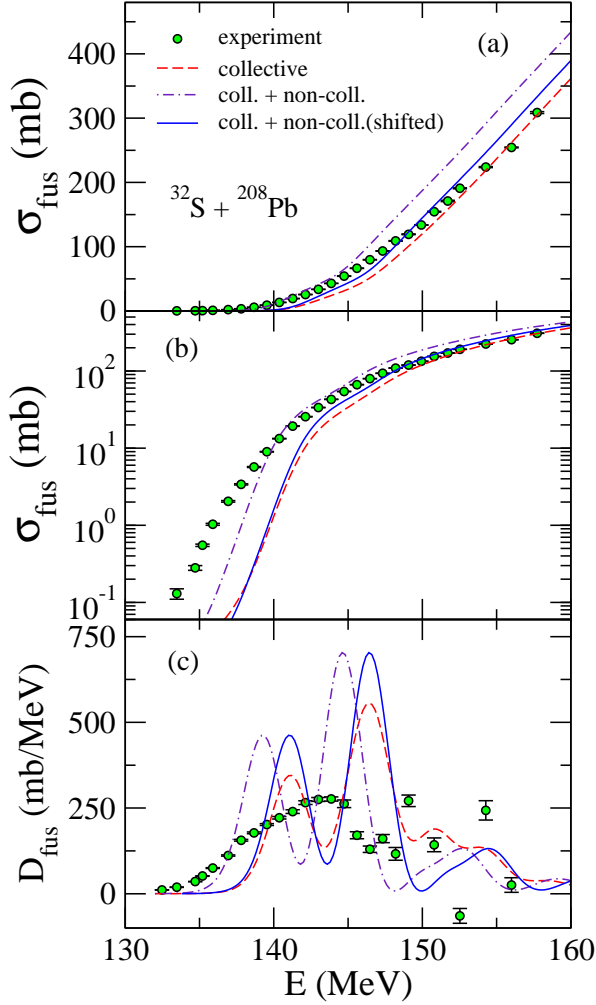


Figure 5.9: Fusion cross section and fusion barrier distribution for the $^{32}\text{S} + ^{208}\text{Pb}$ system. The meaning of each line is the same as in Fig. 5.2. The experimental data are taken from Ref. [23].

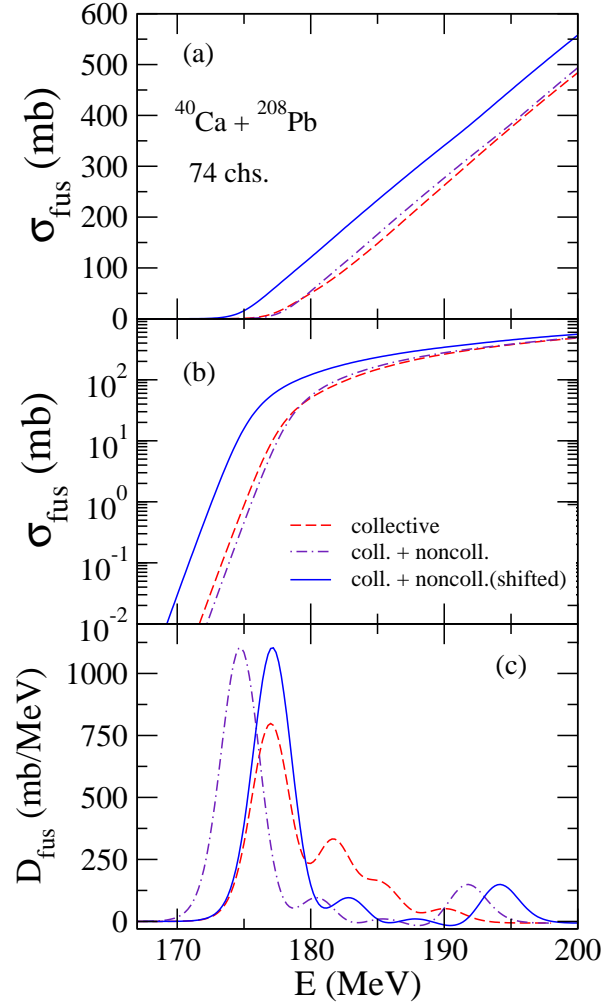


Figure 5.10: Fusion cross section and fusion barrier distribution for the $^{40}\text{Ca} + ^{208}\text{Pb}$ system. The meaning of each line is the same as in Fig. 5.2.

proportional to the charge product of the colliding nuclei [6], and thus the noncollective excitations are effectively stronger for heavier systems. One can also see that the two low-energy peaks in the barrier distribution are sharpened due to the noncollective excitations, while the separation between the peaks is not altered much. The calculations do not reproduce the experimental data, and this might be attributed to the role of transfer reactions.

Figure 5.10 shows the fusion cross section and the fusion barrier distribution for the $^{40}\text{Ca} + ^{208}\text{Pb}$ reaction. For this system, we assume that ^{40}Ca is inert and take into account only the excitations of ^{208}Pb . As the charge product is larger, the effect of the noncollective excitations is stronger than that in the $^{16}\text{O} + ^{208}\text{Pb}$ and $^{32}\text{S} + ^{208}\text{Pb}$ reactions. It smears the higher part of the barrier distribution while the lower main peak is sharpened.

As we have shown, while the effect of noncollective excitations is not large for the $^{16}\text{O} + ^{208}\text{Pb}$

system, the effect becomes increasingly important for heavier systems, such as $^{40}\text{Ca}+^{208}\text{Pb}$. This suggests that the conventional coupled-channels approach, that neglects the noncollective excitations, is well justified for relatively light systems, but the noncollective excitations have to be included explicitly in coupled-channels calculations for heavy-systems, for example, those relevant to a synthesis of superheavy elements.

Chapter 6

Noncollective excitations in $^{20}\text{Ne} + ^{90,92}\text{Zr}$ reaction

In this chapter, we investigate the role of noncollective excitations in the quasi-elastic scattering for $^{20}\text{Ne} + ^{90,92}\text{Zr}$ systems. We employ the random matrix model to describe the noncollective excitation in coupled-channels calculation. The effect on the quasi-elastic barrier distribution is discussed.

6.1 Quasi-elastic scattering for $^{20}\text{Ne} + ^{90,92}\text{Zr}$ systems

For $^{20}\text{Ne} + ^{90,92}\text{Zr}$ systems, quasi-elastic scattering experiments were performed at energies around the Coulomb barrier[19]. From the measured quasi-elastic scattering cross sections, the quasi-elastic barrier distribution has been extracted, as has been shown in Fig. 1.2. The obtained quasi-elastic scattering barrier distributions show a different behavior between the two systems, that is, the barrier distribution for $^{20}\text{Ne} + ^{92}\text{Zr}$ is much more smeared compared to that of $^{20}\text{Ne} + ^{90}\text{Zr}$ system. The dashed line in Fig.??(a) shows the barrier distribution obtained with a coupled-channels calculation which takes into account the collective excitations of ^{20}Ne and ^{90}Zr , that is, the rotational excitations of ^{20}Ne and the vibrational excitations of ^{90}Zr . The calculation reproduces the peak structure of the barrier distribution, while it yields somewhat broader separation of the peaks, which is probably due to the treatment of separation vector in nuclear potential[91, 92]. On the other hand, the calculated barrier distribution for the $^{20}\text{Ne} + ^{92}\text{Zr}$ system shows the similar behavior to that of the $^{20}\text{Ne} + ^{90}\text{Zr}$ system, and does not exhibit a smeared behavior observed in the experimental barrier distribution. This similarity in the barrier distributions of the two systems is because the deformation of ^{20}Ne is so large that the difference in the vibrational excitations of Zr isotopes plays a minor role for the barrier distribution. Thus, the conventional coupled-channels calculation cannot reproduce the barrier distribution for both the systems simultaneously.

As has been discussed in Chap. 1, the difference in the barrier distributions between the two systems has been conjectured to arise from noncollective excitations that are not taken into account

explicitly in the coupled-channels calculations. In this chapter, we take into account the noncollective excitations of Zr isotopes in the calculations for $^{20}\text{Ne} + ^{90,92}\text{Zr}$ reactions and see whether the difference in the quasi-elastic barrier distributions can be explained by the noncollective excitations. See Fig. 1.3 for the energy spectra for the Zr isotopes.

6.2 Random matrix model

In the previous chapter, we investigated the effects of the noncollective excitations in $^{16}\text{O} + ^{208}\text{Pb}$ reaction. In that calculation, the description of the noncollective excitations is based on the experimental information of the noncollective states. Especially, the deformation parameter β_λ , which gives the transition strength to the noncollective states, has been experimentally known for most of low-lying noncollective states in ^{208}Pb . For $^{90,92}\text{Zr}$, however, the information on the deformation parameter is rather limited compared to that for ^{208}Pb . That is, even though the energy and the spin are experimentally known for many noncollective states[22], basically nothing is known for the coupling strength to the ground state. Therefore, one has to resort to a different approach to describe the noncollective excitations in $^{20}\text{Ne} + ^{90,92}\text{Zr}$ reactions. For this purpose, we employ the random matrix model discussed in Sec. 4.5. In this model, we consider the ensemble of the coupling matrix elements and assume the ensemble to make a gaussian orthogonal ensemble(GOE) in the random matrix theory. This model was originally applied to the calculations for deep inelastic collisions by Weidenmüller and his collaborators in the 1970's[44, 45, 47, 48, 49, 50]. We show in appendix B an application of the random matrix model to a one-dimensional barrier penetration problem. The work presented in this chapter can be considered as an extension of this one-dimensional problem to a three-dimensional realistic problem.

We construct the coupling matrix for the noncollective states as follows. The coupling Hamiltonian is expanded in multipoles as

$$V_{\text{coup}}(\mathbf{r}, \boldsymbol{\xi}) = \sum_{\lambda} F_{\lambda}(\mathbf{r}) \cdot T_{\lambda}(\boldsymbol{\xi}), \quad (6.1)$$

with

$$\begin{cases} F_{\lambda\mu}(\mathbf{r}) = f_{\lambda}(r) Y_{\lambda\mu}(\hat{\mathbf{r}}) \\ T_{\lambda\mu}(\boldsymbol{\xi}) = t_{\lambda}(\xi) Y_{\lambda\mu}(\hat{\boldsymbol{\xi}}). \end{cases} \quad (6.2)$$

Then, the coupling Hamiltonian in the iso-centrifugal approximation is obtained by transforming to the rotating frame as

$$V_{\text{coup}}(r, \boldsymbol{\xi}) = \sum_{\lambda} f_{\lambda}(r) Y_{\lambda}^*(\hat{\mathbf{r}} = 0) \cdot T_{\lambda}(\boldsymbol{\xi}) = \sum_{\lambda} \sqrt{\frac{2\lambda+1}{4\pi}} f_{\lambda}(r) T_{\lambda 0}(\boldsymbol{\xi}). \quad (6.3)$$

Using the Wigner-Eckart theorem, the coupling matrix element reads

$$\begin{aligned} V_{nn'}^{II'}(r) &= \langle \phi_{nI} | V_{\text{coup}}(r) | \phi_{n'I'} \rangle \\ &= \sum_{\lambda} \sqrt{\frac{4\pi}{2\lambda+1}} (-1)^I \begin{pmatrix} I & \lambda & I' \\ 0 & 0 & 0 \end{pmatrix} \langle nI || V_{\lambda}(r) Y_{\lambda} || n'I' \rangle \end{aligned} \quad (6.4)$$

with

$$V_{\lambda}(r, \xi) = \frac{2\lambda+1}{4\pi} f_{\lambda}(r) t_{\lambda}(\xi). \quad (6.5)$$

Following Weidenmüller *et al.*, we introduce here the statistical assumption of GOE. That is, we require that the ensemble average of the coupling matrix element vanishes, i.e.,

$$\overline{V_{nn'}^{II'}(r)} = 0. \quad (6.6)$$

We also require the reduced matrix elements to satisfy the following equation

$$\begin{aligned} &\overline{\langle nI || V_{\lambda}(r) Y_{\lambda} || n'I' \rangle \langle n''I'' || V_{\lambda'}(r') Y_{\lambda'} || n'''I''' \rangle} \\ &= \sqrt{(2I+1)(2I'+1)} \frac{2\lambda+1}{4\pi} \left\{ \delta_{nn''} \delta_{n'n'''} \delta_{II''} \delta_{I'I'''} + (-1)^{I-I'} \delta_{nn'''} \delta_{n'n''} \delta_{II'''} \delta_{I'I''} \right\} \\ &\quad \times \delta_{\lambda\lambda'} \alpha_{\lambda}(n, n'; I, I'; r, r'), \end{aligned} \quad (6.7)$$

or, in terms of the coupling matrix, we require

$$\begin{aligned} \overline{V_{nn'}^{II'}(r) V_{n'n'''}^{I''I'''}(r')} &= \{ \delta_{nn''} \delta_{n'n'''} \delta_{II''} \delta_{I'I'''} + \delta_{nn'''} \delta_{n'n''} \delta_{II'''} \delta_{I'I''} \} \sqrt{(2I+1)(2I'+1)} \\ &\quad \times \sum_{\lambda} \begin{pmatrix} I & \lambda & I' \\ 0 & 0 & 0 \end{pmatrix}^2 \alpha_{\lambda}(n, n'; I, I'; r, r'). \end{aligned} \quad (6.8)$$

Here, the form factor α_{λ} is given by

$$\alpha_{\lambda}(n, n'; I, I'; r, r') = \frac{w_{\lambda}}{\sqrt{\rho(n, I) \rho(n', I')}} e^{-\frac{(\epsilon_n - \epsilon_{n'})^2}{2\Delta^2}} e^{-\frac{(r-r')^2}{2\sigma^2}} h(r) h(r'), \quad (6.9)$$

where $\rho(n, I)$ is a level density with spin I at excitation energy ϵ_n , $h(r)$ is a some function of r , and $(w_{\lambda}, \Delta, \sigma)$ are parameters. The level density in the denominator of the form factor reflects the complexity of the noncollective states, as we have discussed in Sec. 4.5. We present in appendix C the calculation method of the coupling matrix elements. Concerning the coupling to the noncollective excitations, we consider only the coupling from the ground state. Therefore, one of the level densities entered in the form factor is constant in our calculations. Thus we modify the form factor as

$$\alpha_{\lambda}(n, 0; I, 0; r, r') = \frac{w_{\lambda}}{\sqrt{\rho(n)}} e^{-\frac{\epsilon_n^2}{2\Delta^2}} e^{-\frac{(r-r')^2}{2\sigma^2}} h(r) h(r'), \quad (6.10)$$

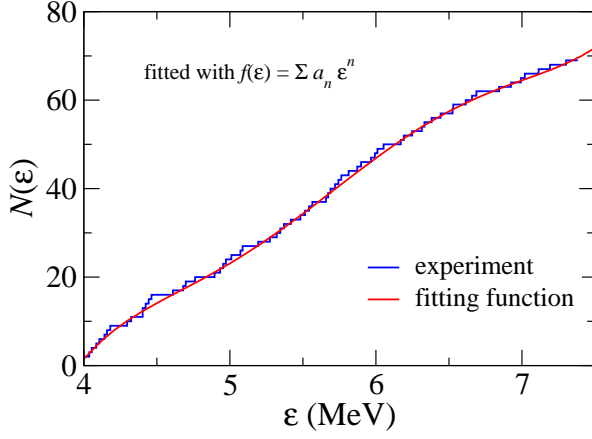


Figure 6.1: The number of levels of ^{208}Pb up to the excitation energy ϵ as a function of ϵ . The dots represents experimental data and the red line is a fitting function.

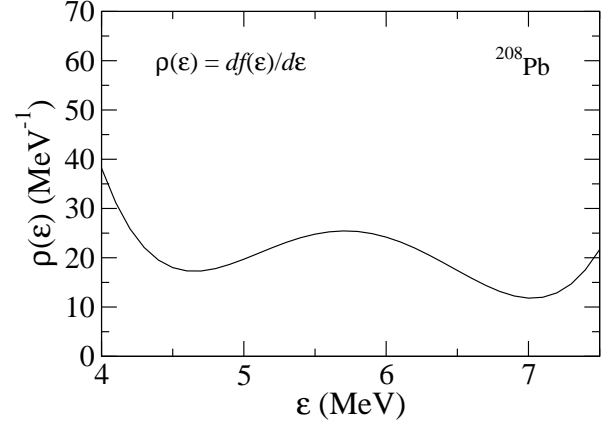


Figure 6.2: Continuous level density obtained as a first derivative of the fitting function $f(\epsilon)$ shown in Fig.6.1.

where, 0 means the ground state. We have also replaced the spin dependent level density by the total level density for the sake of simplicity.

Before applying the model to the reaction of $^{20}\text{Ne} + ^{90,92}\text{Zr}$ systems, we first apply the model to $^{16}\text{O} + ^{208}\text{Pb}$ system in order to study the validity of the model by comparing the results with the more reliable results which use the experimental information on the noncollective states as presented in the previous section.

6.3 Level density and strength distribution

In order to apply the random matrix model to $^{16}\text{O} + ^{208}\text{Pb}$, we first discuss the treatment of the level density $\rho(n)$. The level density is defined by

$$\rho(\epsilon) = \sum_n \delta(\epsilon - \epsilon_n), \quad (6.11)$$

which is a discrete spectrum. From this discrete spectrum, we define a continuous level density, which is used in the calculation of the coupling matrix elements in the random matrix model. To do this, we first define the following function

$$N(\epsilon) = \int_0^\epsilon \rho(\epsilon') d\epsilon'. \quad (6.12)$$

This gives the number of levels up to the excitation energy ϵ . We fit $N(\epsilon)$ with a polynomial function. In Fig. 6.1, we show the fitting result for ^{208}Pb nucleus. We use the $N(\epsilon)$ in the interval between 4 MeV and 7.5 MeV and fitted with a polynomial $f(\epsilon) = \sum_{n=0}^6 a_n \epsilon^n$. The resultant values of a_n are $a_0 = -7479$, $a_1 = 6969$ (MeV^{-1}), $a_2 = -2612$ (MeV^{-2}), $a_3 = 497.5$ (MeV^{-3}), $a_4 = -49.59$

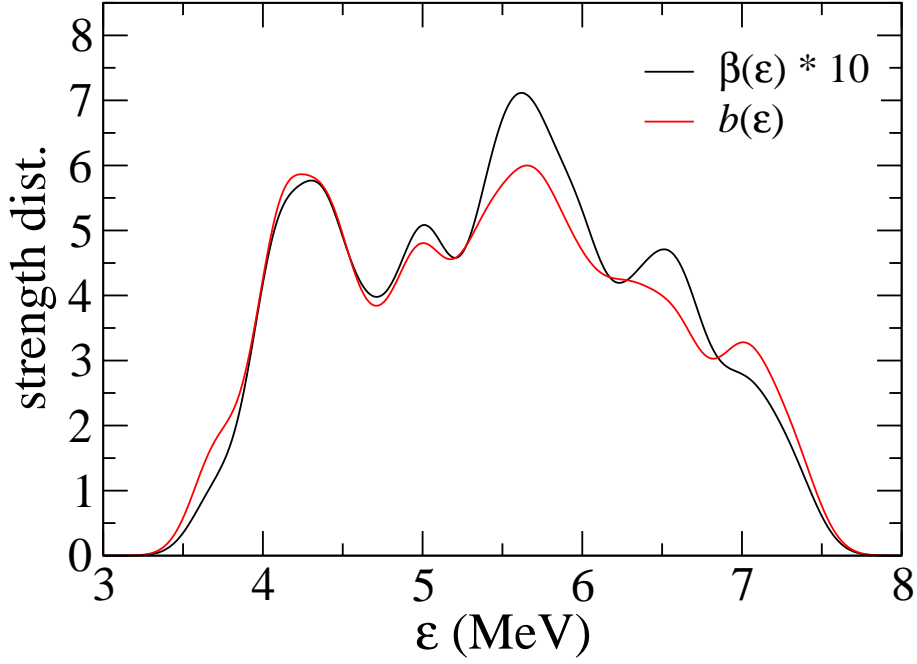


Figure 6.3: Transition strength distributions for ^{208}Pb as a function of excitation energy ϵ . The black line is the distribution of the experimental deformation parameters and the red line is the strength distribution defined in Eq. (6.13) with RMT. Both distributions are smeared with a gaussian function with a width of 0.15 MeV. The black line is scaled by a factor of 10.

(MeV^{-4}), $a_5 = 2.347$ (MeV^{-5}), and $a_6 = -0.03632$ (MeV^{-6}). The continuous level density is then defined by the first derivative of $f(\epsilon)$, that is, $df(\epsilon)/d\epsilon$, which is shown in Fig. 6.2.

Using this level density, we calculate the strength distribution which we define by (see Eqs. (6.9) and (6.10))

$$b_I = \sqrt{\sum_{\lambda} \begin{pmatrix} 0 & \lambda & I \\ 0 & 0 & 0 \end{pmatrix}^2} \sqrt{\frac{2I+1}{\rho(\epsilon)}} e^{-\frac{\epsilon^2}{2\Delta^2}} \quad (6.13)$$

(w_{λ} is omitted in the definition by assuming $w_{\lambda} = w$ for all λ). This quantity corresponds to the distribution of the deformation parameter β_I , since, in the linear coupling approximation, the coupling matrix elements are given by

$$V_{0n}(r) = -\beta_I R_T \frac{dV_N}{dr}. \quad (6.14)$$

Fig.6.3 shows a comparison of experimental deformation parameter, β_I , and the strength distribution in RMT, b_I , as a function of excitation energy. The parameter Δ in (6.13) is chosen to be 7 MeV. Both distributions are smeared with a gaussian function whose width is 0.15 MeV. The deformation parameter is scaled by a factor of 10 because the dimension of β_I and b_I is not taken to be the same, while the both quantities determine the coupling strength to each excited state. Although the small deficiency of the strength can be seen for peaks between 5.5 MeV and 7 MeV, the overall

peak structure of the strength distribution is reasonably reproduced by the random matrix model.

6.4 Test of random matrix model with $^{16}\text{O} + ^{208}\text{Pb}$ reaction

In this section, we apply the random matrix model to $^{16}\text{O} + ^{208}\text{Pb}$ reaction in order to see whether the random matrix model works well for the description of the noncollective excitations in low-energy heavy-ion reactions.

For the function $h(r)$ in the form factor (6.10), we adopt the following form

$$h(r) = \frac{e^{(r-R_n)/a}}{[1 + e^{(r-R_n)/a}]^2}, \quad (6.15)$$

which is the same functional form as the derivative of the Woods Saxon potential. Thus, the coupling matrix elements become similar to that of the vibrational coupling in the linear coupling approximation. For the parameters in Eq. (6.10), we use $w = 38000 \text{ MeV}^{3/2}$, $\Delta = 7 \text{ MeV}$, and $\sigma = 4.0 \text{ fm}$. The value of Δ is chosen so that all the considered excited states up to 7.382 MeV have a chance to be excited. The values of Δ and σ are the same as those used in Refs. [49, 50]. The value of w is chosen so that the random matrix model reproduces the results obtained with the experimental β_I .

In Fig.6.4, we show the comparison for fusion cross sections. The potential has the same geometry as that used in the previous chapter, while the potential depth is set to be 550 MeV , because in these calculation, we do not take into account the excitation of ^{16}O for simplicity. The red lines show the results using the experimental deformation parameters. This calculation is similar to that in the previous chapter, while the linear coupling approximation is employed in the present calculation. The blue lines are the results using the random matrix model for the description of the noncollective excitations. For comparison, the calculation which takes into account only the collective excitations are show by the black dashed lines. By choosing an appropriate parameter w , we can see that the random matrix model nicely reproduces the results which use the experimental deformation parameters. Therefore, we conclude that the random matrix model is applicable to the description of the noncollective excitations by choosing appropriate parameters in the model.

6.5 Application to $^{20}\text{Ne} + ^{90,92}\text{Zr}$ systems

6.5.1 Parameters

Encouraged by the comparative study presented in the previous section, we now apply the random matrix model to the $^{20}\text{Ne} + ^{90,92}\text{Zr}$ reactions. We use the same parameters as those used in Ref.[19], that is, the surface diffuseness parameter of $a = 0.63 \text{ fm}$, the radius parameter of $r_0 = 1.2 \text{ fm}$, and the potential depth parameter of $V_0 = 59.9 \text{ MeV}$. For this potential, the height of the Coulomb

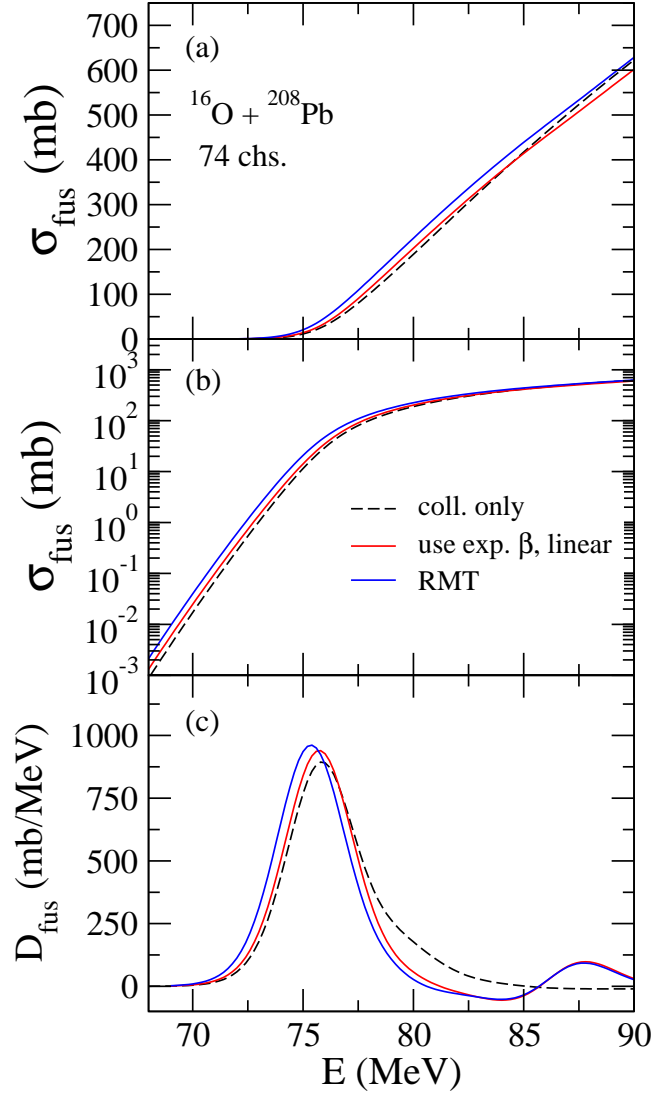


Figure 6.4: The fusion cross sections((a) and (b)) and the fusion barrier distributions((c)) for $^{16}\text{O} + ^{208}\text{Pb}$ system. The red lines are the results obtained with the experimental deformation parameter. The blue lines are the results of the calculation based on the random matrix model. The black dashed lines are the results of the calculation with only the collective excitations.

barrier becomes $V_B = 51.76$ MeV.

As for the coupling to ^{20}Ne , we take into account the rotational states in the ground band up to 6^+ state with the deformation parameters $\beta_2 = 0.46$ and $\beta_4 = 0.27$. The octupole phonon state at 5.62 MeV is also considered with $\beta_3 = 0.39$. For the coupling to collective states in ^{90}Zr nucleus, we take into account the vibrational 2^+ state at 2.18 MeV with $\beta_2 = 0.089$ and 3^- state at 2.75 MeV with $\beta_3 = 0.211$ [93]. For ^{92}Zr , we take into account the vibrational 2^+ state at 0.93 MeV with $\beta_2^{(N)} = 0.144$ and $\beta_2^{(C)} = 0.103$ as well as 3^- state at 2.34 MeV with $\beta_3 = 0.17$ [94]. These phonon excitations in Zr isotopes are taken into account up to the two-phonon state, while the mutual excitations of quadrupole and octupole phonon states are not included.

For the coupling to the noncollective states, we use the experimental data for the excitation

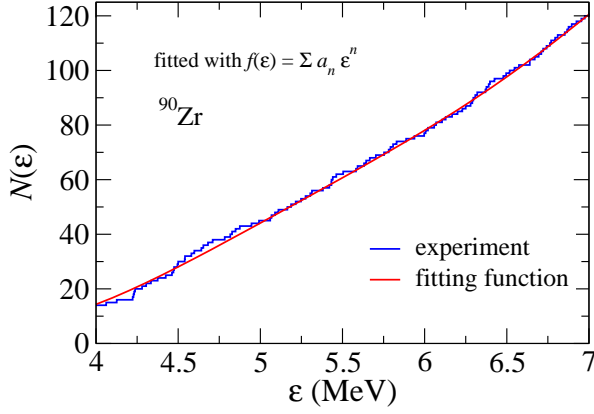


Figure 6.5: Same as Fig. 6.1, but for ^{90}Zr .

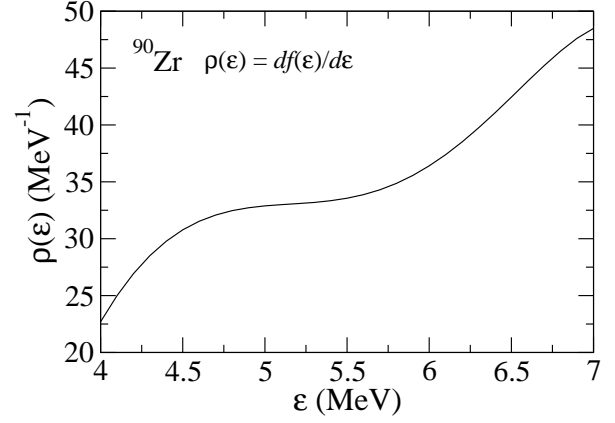


Figure 6.6: Same as Fig. 6.2, but for ^{90}Zr .

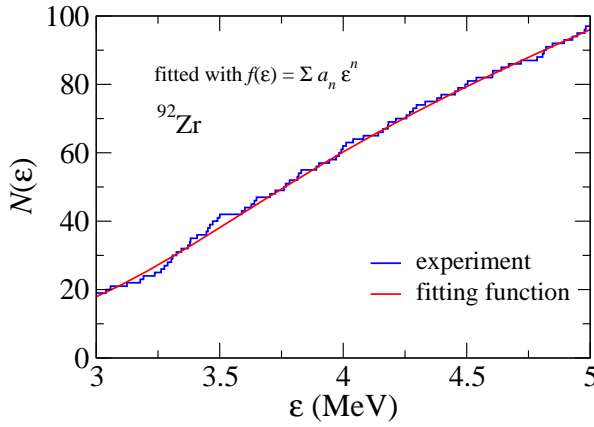


Figure 6.7: Same as Fig. 6.1, but for ^{92}Zr .

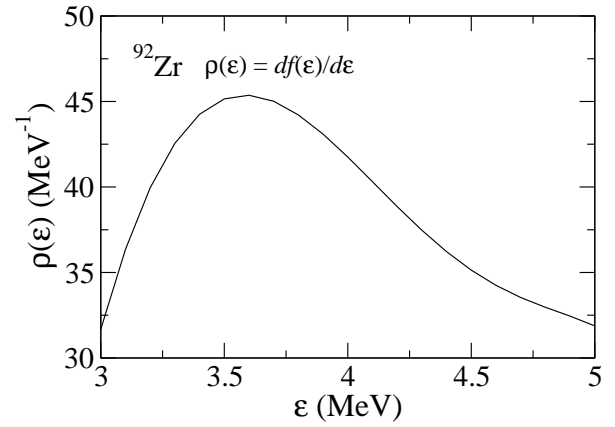


Figure 6.8: Same as Fig. 6.2, but for ^{92}Zr .

energies and spins. The coupling matrix elements themselves are calculated by the random matrix model. Among the noncollective states, we take into account only the natural parity states, because the unnatural parity states are not probable to be excited compared to the natural parity states in the collision of even-even nuclei. The noncollective states are assumed to be coupled only to the ground state for simplicity, which corresponds to the linear coupling approximation. For the parameters in the random matrix model, we employ $\Delta = 7$ MeV, $\sigma = 4$ fm, and $w = 200$ MeV $^{3/2}$. The values of Δ and σ are the same as in the calculations for $^{16}\text{O} + ^{208}\text{Pb}$ reaction, and the value of w is determined so that the calculated barrier distribution for the $^{20}\text{Ne} + ^{92}\text{Zr}$ system agrees with the experimental barrier distribution as well as possible. The same parameters are then used for the calculations for $^{20}\text{Ne} + ^{90}\text{Zr}$ reaction. The level density is constructed in the same way as that in the case of $^{16}\text{O} + ^{208}\text{Pb}$ calculation, as we show in Figs. 6.5 and 6.6 for ^{90}Zr and in Figs. 6.7 and 6.8 for ^{92}Zr . For ^{90}Zr , $N(\epsilon)$ defined by Eq. (6.12) is fitted in the interval between 3 MeV and 8 MeV with a polynomial $f(\epsilon) = \sum_{n=0}^6 a_n \epsilon^n$. The resultant parameters are $a_0 = 199.2$, $a_1 = 182.5$ (MeV $^{-1}$), $a_2 = -286.5$ (MeV $^{-2}$), $a_3 = 119.7$ (MeV $^{-3}$), $a_4 = -22.65$ (MeV $^{-4}$), $a_5 = 2.057$ (MeV $^{-5}$), and $a_6 = -0.07278$ (MeV $^{-6}$). For ^{92}Zr , $N(\epsilon)$ is fitted in the interval between 2.5 MeV and 6 MeV and

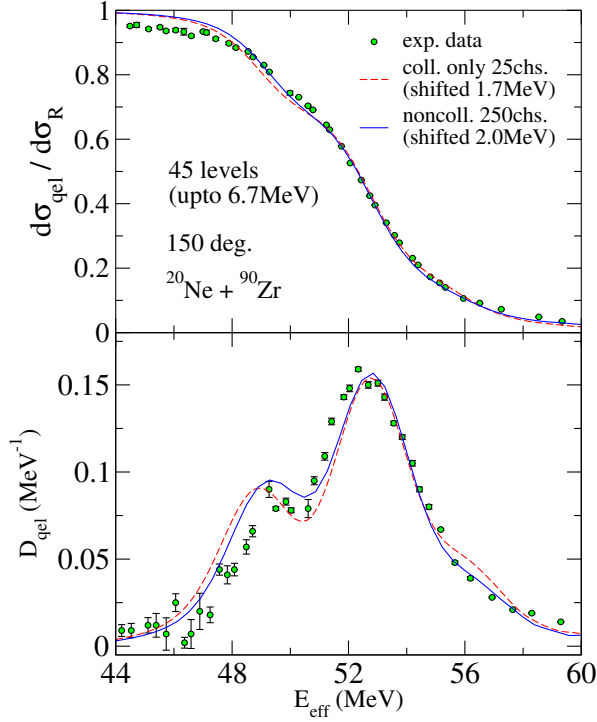


Figure 6.9: Quasi-elastic cross sections (upper panel) and quasi-elastic barrier distribution (lower panel) for $^{20}\text{Ne} + ^{90}\text{Zr}$ system at 150° . The red dashed lines are the results with only the collective excitations, while the blue lines are the results which include the noncollective excitations in addition to the collective excitations.

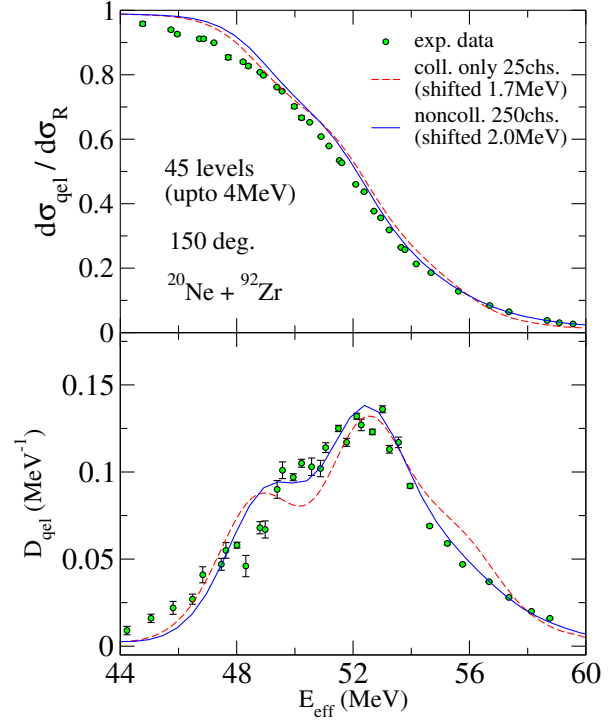


Figure 6.10: Same as Fig.6.9, but for $^{20}\text{Ne} + ^{92}\text{Zr}$ system.

the resultant parameters are $a_0 = 63.79$, $a_1 = 540.7$ (MeV^{-1}), $a_2 = -737.2$ (MeV^{-2}), $a_3 = 366.7$ (MeV^{-3}), $a_4 = -87.00$ (MeV^{-4}), $a_5 = 10.07$ (MeV^{-5}), and $a_6 = -0.4589$ (MeV^{-6}). We take into account the mutual excitations of ^{20}Ne and $^{90,92}\text{Zr}$.

6.5.2 Results

Quasi-elastic scattering cross sections and barrier distribution

We first show the results obtained by including 45 noncollective levels both in ^{90}Zr and ^{92}Zr nuclei. Inclusion of 45 noncollective levels corresponds to taking into account excited states up to 6.7 MeV for ^{90}Zr and 4.0 MeV for ^{92}Zr . Figs.6.9 and 6.10 show the quasi-elastic scattering cross section and quasi-elastic barrier distribution for $^{20}\text{Ne} + ^{90}\text{Zr}$ and $^{20}\text{Ne} + ^{92}\text{Zr}$ reactions, respectively. For both figures, the dots represent the experimental data[19] at the scattering angle $\theta_{\text{lab}} = 150^\circ$, the red dashed lines represent the results which take into account only the collective excitations, and blue solid lines represent the results which take into account the noncollective excitations in addition to the collective excitations. In Figs.6.9, 6.10 the red and the blue lines are shifted in energy by

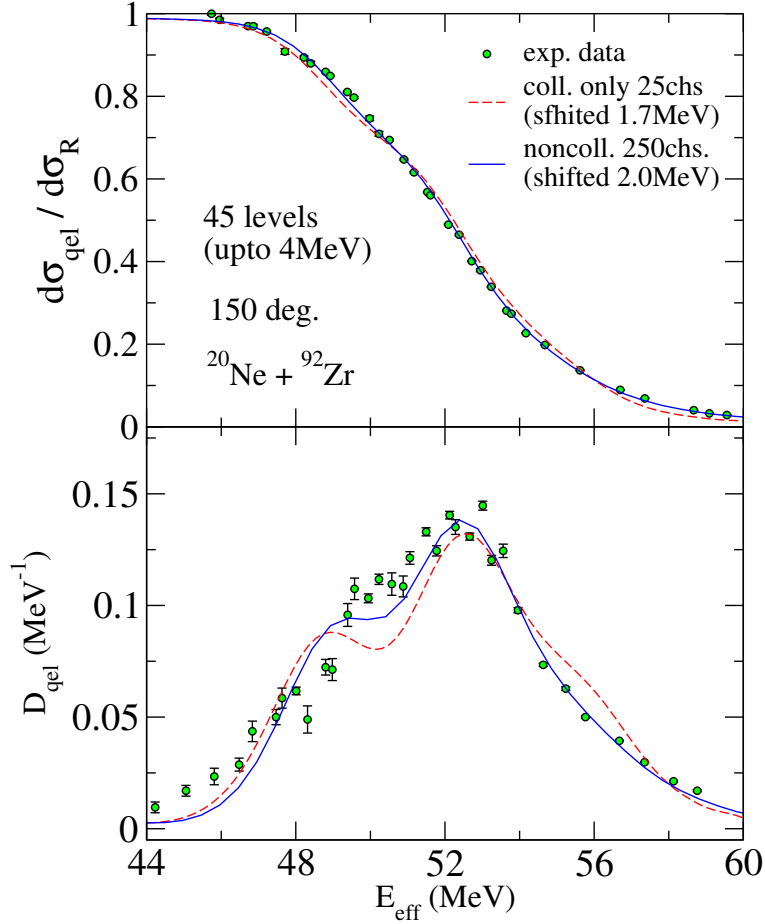


Figure 6.11: Same as Fig.6.10, but with a scaling of the experimental data by a factor of 0.94.

1.7 MeV and 2.0 MeV, respectively, in order to adjust the barrier height. The difference in the amount of shifts between the red dashed line and the blue solid line originates from the potential renormalization due to the high excitation energy of the noncollective states as has been discussed in the reaction of $^{16}\text{O} + ^{208}\text{Pb}$ in the previous chapter. For $^{20}\text{Ne} + ^{90}\text{Zr}$ reaction, we can see that even when we include the noncollective excitations, they do not alter the barrier distribution in a significant way with the present parameters, although the ditch between the two peaks is somewhat filled. Thus, the noncollective excitations do not deteriorate the agreement with the data for $^{20}\text{Ne} + ^{90}\text{Zr}$ quasi-elastic scattering. On the other hand, for $^{20}\text{Ne} + ^{92}\text{Zr}$ reaction, the noncollective excitations fill the ditch between the peaks and the peak structure is thus considerably smeared. As a consequence, the agreement with the experimental barrier distribution is much improved for the $^{20}\text{Ne} + ^{92}\text{Zr}$ system. In these calculations, the same parameters in the random matrix model are used both for $^{20}\text{Ne} + ^{90}\text{Zr}$ and $^{20}\text{Ne} + ^{92}\text{Zr}$ reactions. Therefore, the difference of the effects of the noncollective excitations comes from the level density in the form factor Eq. (6.9) and the level structure between ^{90}Zr and ^{92}Zr nuclei, that is, a large number of noncollective states at a relatively low excitation energy region in ^{92}Zr . We also notice that the agreement at the high energy tail of the barrier distribution is also improved due to the noncollective excitations.

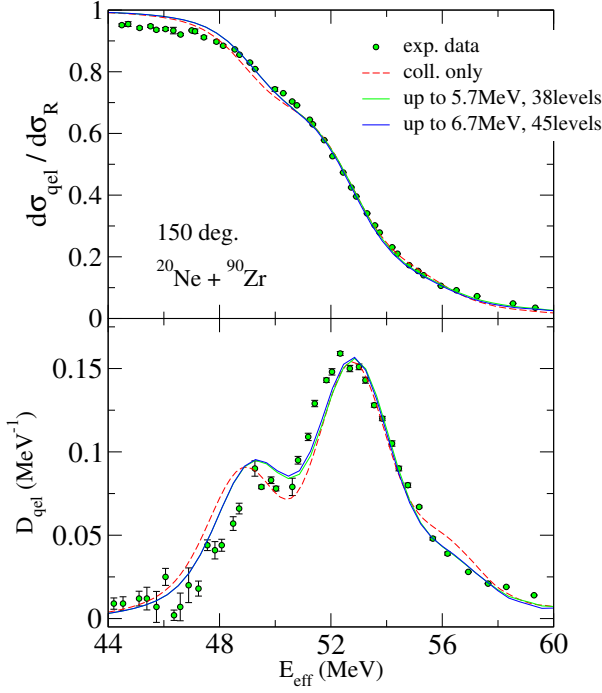


Figure 6.12: Convergence of the coupled-channels calculation for $^{20}\text{Ne} + ^{90}\text{Zr}$ with respect to the truncation of excited states of ^{90}Zr . The red dashed and the blue solid lines are the same as in Fig.6.9. The green lines includes the noncollective levels up to 5.7 MeV.

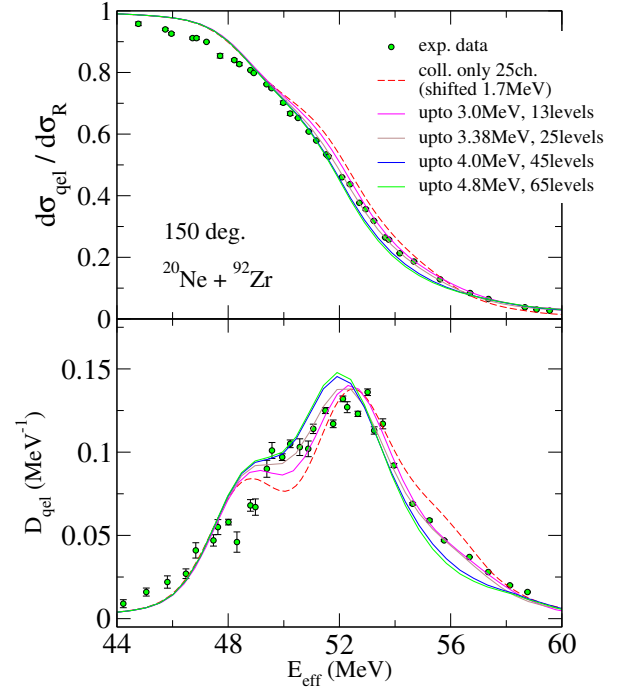


Figure 6.13: Convergence of the coupled-channels calculation for $^{20}\text{Ne} + ^{92}\text{Zr}$ with respect to the truncation of excited states of ^{92}Zr . The energy truncation is changed from 3.0 MeV to 4.8 MeV. The red dashed and the blue solid lines are the same as in Fig.6.10.

Although the barrier distributions are well reproduced by including the noncollective excitations, the agreement of the quasi-elastic scattering cross sections becomes worse. This may be due to the treatment of the normalization of the experimental cross sections. In fact, if we divide the experimental data by 0.94, the agreement for cross sections is improved as is shown in Fig. 6.11 for the $^{20}\text{Ne} + ^{92}\text{Zr}$ system. Notice that the shape of barrier distribution does not change by this overall scaling. In the experiment, the scattering cross sections are measured at a forward angle ($\theta_{\text{lab}} = 35^\circ$) as well as backward angles. Assuming the Rutherford cross sections for the measured cross sections at the forward angle, the corresponding scattering cross sections at backward angles are obtained, with which the experimental $\sigma_{\text{qel}}/\sigma_{\text{R}}$ is constructed. The data is further normalized by setting the cross section to be unity at the lowest incident energy in the measurement. The data shown in Fig. 6.11 correspond to those normalized at $E = 44$ MeV, rather than at the lowest energy.

Convergence of calculated results

We next discuss the convergence of the calculations with respect to the energy truncation. In Fig.6.12, we show the calculation for $^{20}\text{Ne} + ^{90}\text{Zr}$ scattering. The red and the blue lines are the same as those in Fig.6.9. The green solid lines take into account the noncollective excitations up to excitation energy 5.7 MeV, while up to 6.7 MeV for the blue lines. The number of the noncollective

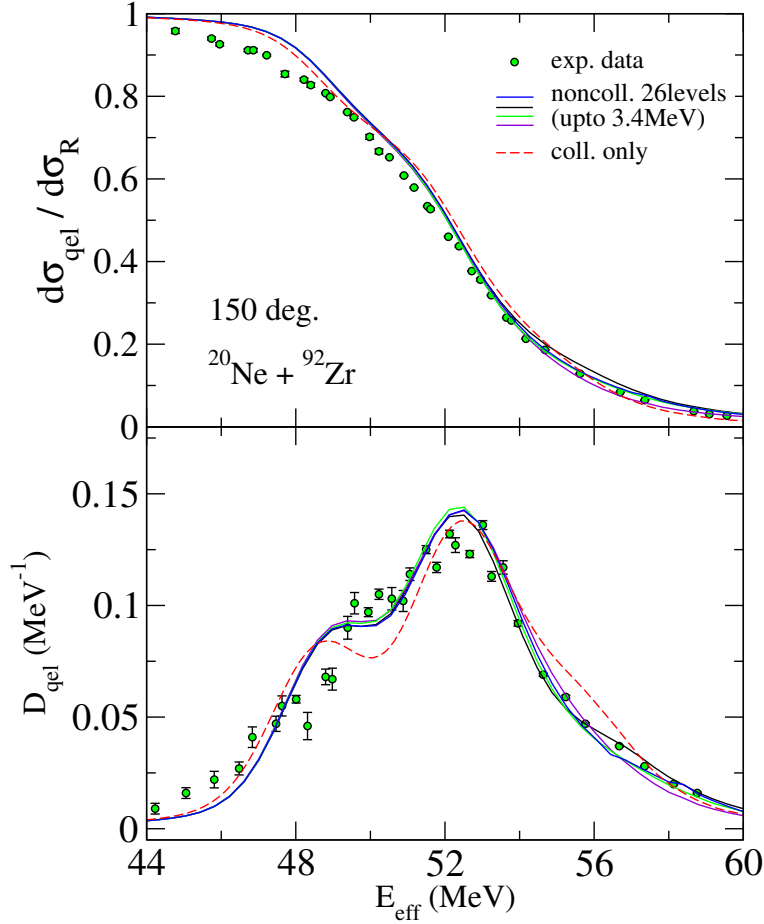


Figure 6.14: Calculations with four differently generated coupling matrices in the random matrix model (the solid lines). The red dashed lines include only the collective excitations.

levels up to 5.7 MeV is 38. We can see that the green and the blue lines are almost the same, that is, the convergence is already obtained if one includes 25 levels for ^{90}Zr nucleus. In Fig.6.13, we show the calculation for $^{20}\text{Ne} + ^{92}\text{Zr}$ system with several truncations of the noncollective excitations ranging from 3.0 MeV to 4.8 MeV. The red and the blue lines are the same as those in Fig.6.10. We can see the gradual increase of the effects of noncollective excitations and that the convergence is obtained if one includes the excited states up to 4.0 MeV. In Fig. 6.13, all the calculations are shifted by 1.7 MeV. We can see that the lower energy tail of the barrier distribution is hardly altered by the noncollective excitations, while the higher region is shifted towards the low-energy side. We can understand this behavior from the energy dependence of the Q-value distribution discussed in the next subsection.

In the random matrix model, the meaningful quantity is the ensemble averaged quantity. The calculated results shown above are not ensemble averaged. In order to see the dispersion due to the random matrix, we show in Fig.6.14 the four calculations with differently generated coupling matrices by the solid lines (these calculations take into account only 26 noncollective levels in order to reduce the computational effort). For comparison, we show the calculation with only the

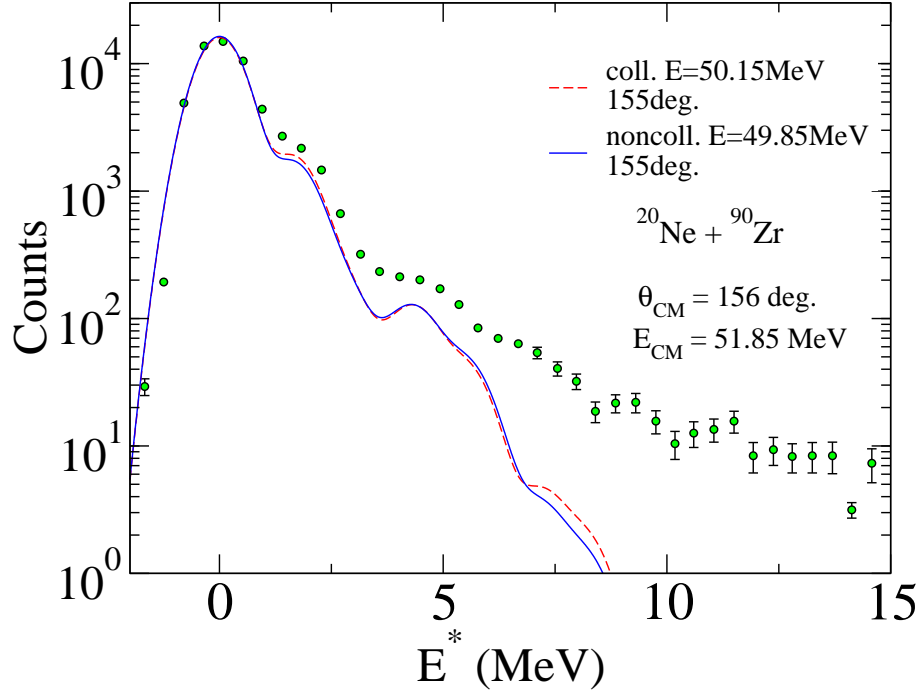


Figure 6.15: Q-value distributions for $^{20}\text{Ne} + ^{90}\text{Zr}$ system. The experimental data are taken at CM angle 156° and CM energy of 51.85 MeV[19]. The red dashed line includes only the collective excitations and the blue solid line includes the noncollective excitations as well. The calculations are taken at different energies corresponding to the shift in the barrier distribution due to the potential renormalization.

collective excitations by the red dashed line. We can see that the dispersion due to the different random matrices is sufficiently small compared to the change due to the noncollective excitations. This justifies the use of the non-averaged results in the discussion of the noncollective effects.

Q-value distribution

We next present the calculation for a Q-value distribution in Figs.6.15 and 6.16 for $^{20}\text{Ne} + ^{90}\text{Zr}$ and $^{20}\text{Ne} + ^{92}\text{Zr}$ systems, respectively. In the figures, the dots represent the experimental data, the red dashed lines represent the calculation with only the collective excitations and the blue solid lines represent the calculation with the noncollective excitations in addition to the collective excitations. (The experimental data for $^{20}\text{Ne} + ^{92}\text{Zr}$ shown in Fig. 5 in Ref. [19] has been found to be wrong[99]. The correct data are shown in Fig. 6.16.) The experimental data are taken at $\theta_{\text{CM}} = 156^\circ$ and $E_{\text{CM}} = 51.85$ MeV and do not include the transfer processes. The calculations shown in the figures are taken at different energies corresponding to the shift in the barrier distribution due to the potential renormalization. These are smeared with a gaussian function Eq. (5.6) with a width of $\Delta = 0.5$ MeV to adjust the width of the elastic peak of the data, and are normalized to the height of the elastic peak. We can see that in both systems, the noncollective excitations have a small effect on the Q-value distribution at this incident energy. For $^{20}\text{Ne} + ^{90}\text{Zr}$ system, the calculation reasonably reproduces the data up to about 5 MeV, while above 5 MeV, it underestimates the data.

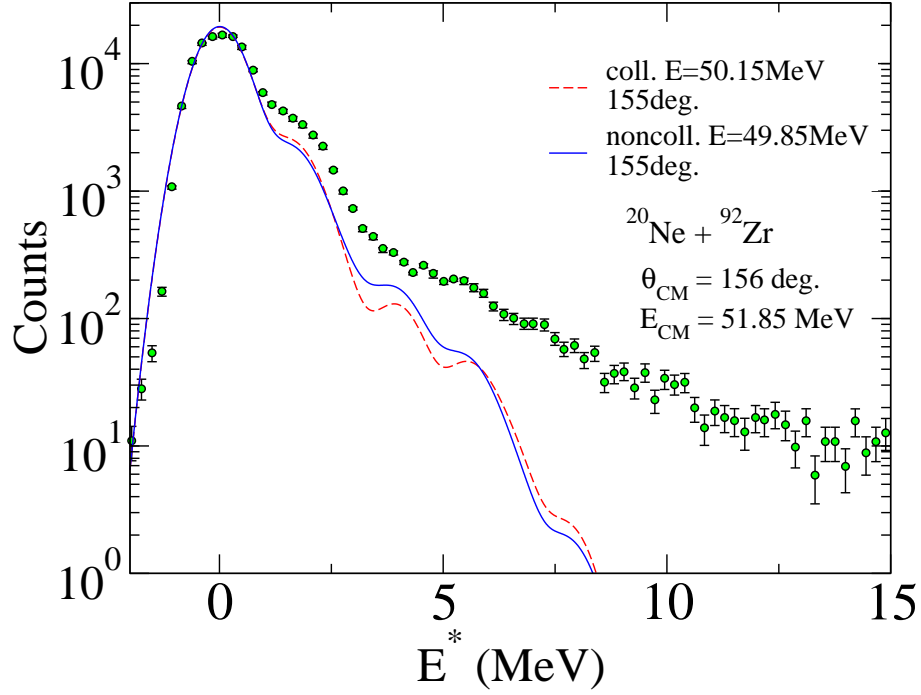


Figure 6.16: Q-value distributions for $^{20}\text{Ne} + ^{92}\text{Zr}$ system. The meaning of each line is the same as Fig.6.15. The experimental data are taken from Ref. [99].

For $^{20}\text{Ne} + ^{92}\text{Zr}$ system, the noncollective excitations enhance the contribution from the inelastic channels between about 3 to 6 MeV, and the data is reasonably reproduced up to 4 MeV. Above 4 MeV, the present calculation does not reproduce the data as in the case of ^{90}Zr . We compare the results of the two systems in Fig. 6.17. The blue ones are the experimental data and the calculation for $^{20}\text{Ne} + ^{90}\text{Zr}$ system, and the red ones are those for $^{20}\text{Ne} + ^{92}\text{Zr}$ system. They are normalized at the height of the elastic peak. We can see that the data show almost the same Q-value distribution between the two systems. This suggests that the difference in the number of the noncollective states between ^{90}Zr and ^{92}Zr nuclei (see Fig. 1.3) does not affect the Q-value distribution at this energy. This is consistent with our calculation shown in the figure, and thus, we conclude that our calculation accounts for the data qualitatively well.

However, this does not mean that the noncollective excitations are not important in the Q-value distribution. We have seen that the contribution from the noncollective excitation becomes important as the incident energy increases for the reaction of $^{16}\text{O} + ^{208}\text{Pb}$ system. In fact, the same tendency is observed for $^{20}\text{Ne} + ^{90,92}\text{Zr}$ systems as shown in Figs. 6.18 and 6.19. These figures show the Q-value distribution at different incident energies from 40 MeV to 60 MeV. The solid red spectra show the contribution from the collective channels, the blue spectra show the contribution from the noncollective channels, and the envelope shows the Q-value distribution smeared with a gaussian function with a width of 0.2 MeV. For both systems, the contribution from the collective excitations is dominant below the barrier (about 52 MeV), while the contribution from the noncollective excitations becomes important as the incident energy increases. However, the peak

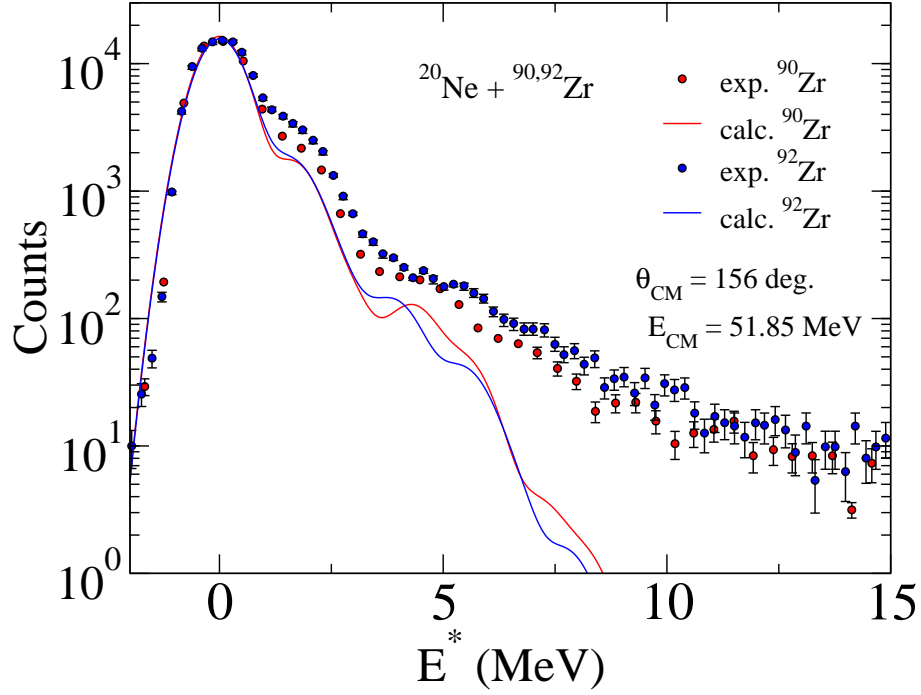


Figure 6.17: Comparison of the Q-value distributions between $^{20}\text{Ne} + ^{92}\text{Zr}$ and $^{20}\text{Ne} + ^{90}\text{Zr}$ systems.

structure of the Q-value distribution is mainly constructed by the collective excitations for $^{20}\text{Ne} + ^{90}\text{Zr}$ system even above the Coulomb barrier. On the other hand, for $^{20}\text{Ne} + ^{92}\text{Zr}$ system, the noncollective excitations also contribute to the construction of a peak structure. Since the contribution from the noncollective excitations is important at larger (above barrier) energies, the potential renormalization can be observed in the high energy region in Fig. 6.13.

In order to observe the effect of the noncollective excitations on the Q-value distribution, it will be necessary to measure the data above the barrier energies and see the energy dependence.

Reactions with different projectiles

We have shown that the noncollective excitations of $^{90,92}\text{Zr}$ nuclei improve the calculations for $^{20}\text{Ne} + ^{90,92}\text{Zr}$ reactions. In order to see whether our description of the noncollective excitations works for other reactions, we apply the model to $^{16}\text{O} + ^{92}\text{Zr}$ and $^{28}\text{Si} + ^{92}\text{Zr}$ fusion reactions, where the fusion cross sections are experimentally obtained and coupled-channels analyses have been performed[94]. Figs.6.20 and 6.21 show the results for $^{16}\text{O} + ^{92}\text{Zr}$ and $^{28}\text{Si} + ^{92}\text{Zr}$ systems, respectively. In both figures, the dots represent the experimental data[94], the red lines represent the calculation with only the collective excitations, and the blue lines represent the calculation with the noncollective excitations in addition to the collective excitations. The upper and the middle panels show the fusion cross sections in the linear and logarithmic scales, respectively, while the bottom panel shows the fusion barrier distribution. For the ^{16}O projectile, we take into account the vibrational 3^- state at 6.13 MeV as in the reaction for $^{16}\text{O} + ^{208}\text{Pb}$ system discussed in the previous chapter. The potential parameters in the Woods-Saxon potential are $V_0 = 55.16$ MeV

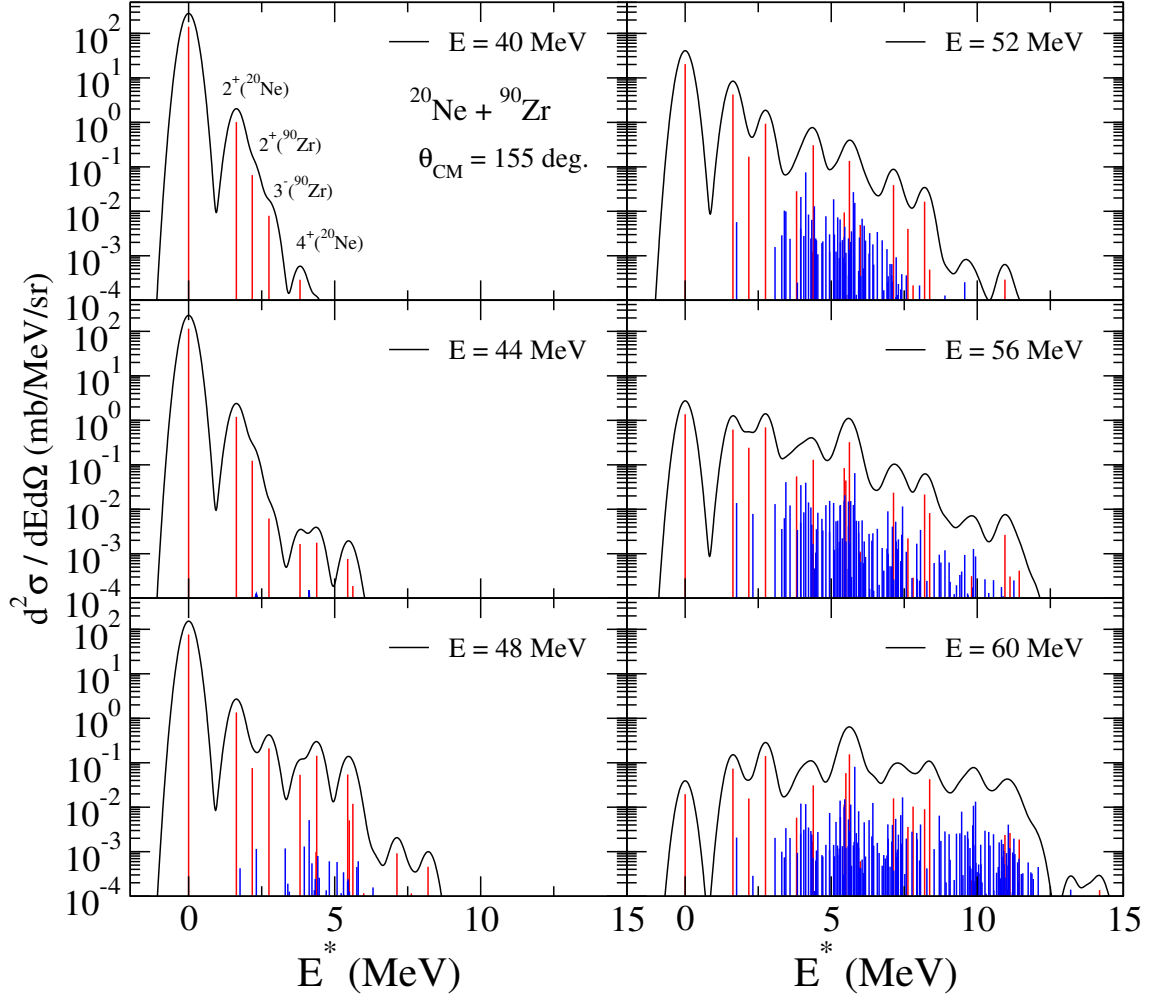


Figure 6.18: The energy dependence of the Q-value distribution for $^{20}\text{Ne} + ^{90}\text{Zr}$ system. The red and the blue spectra show the contribution from the collective and the noncollective channels, respectively. The black lines are obtained by smearing the spectra with a gaussian function with a width of 0.2 MeV.

for the potential depth, $r_0 = 1.17$ fm for the radius parameter, and $a = 0.60$ fm for the surface diffuseness parameter. These parameters are chosen so that the calculation reproduces the height of the Coulomb barrier. We can see that the noncollective excitations hardly affect the barrier distribution. For this system, the barrier distribution has almost a single peak structure even in the absence of the noncollective excitations. This is because the vibrational excitations of ^{92}Zr are not so strong to yield a well structured barrier distribution and the octupole phonon state in ^{16}O only renormalizes the potential barrier. Therefore, the smearing due to the noncollective excitations does not change the shape of the barrier structure. In addition to this, the smaller charge product of the projectile and the target also makes the effect of the noncollective excitations small compared to that in the $^{20}\text{Ne} + ^{92}\text{Zr}$ system.

For the ^{28}Si projectile, we take into account the rotational excitations with $\epsilon_2 = 1.779$ MeV and $\beta_2 = -0.407$ up to the 6^+ state, and the octupole one-phonon state with $\epsilon_3 = 6.88$ MeV and $\beta_3 = 0.280$. The potential parameters in the Woods-Saxon potential are $V_0 = 60.25$ MeV, $r_0 = 1.18$

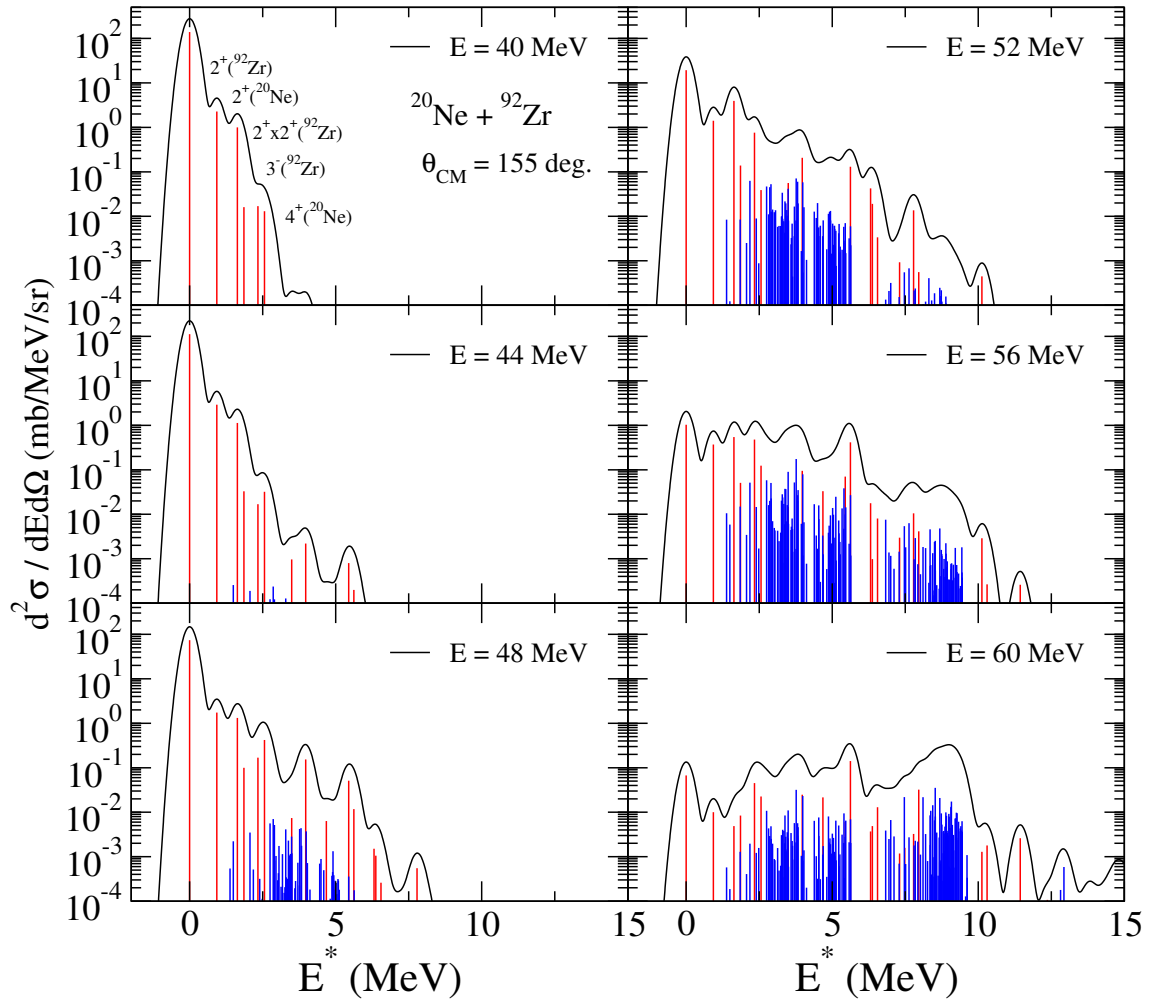


Figure 6.19: Same as Fig.6.18, but for $^{20}\text{Ne} + ^{92}\text{Zr}$ system.

fm, and $a = 0.63$ fm. We can see that the barrier distribution is smeared due to the noncollective excitations and the peak structure becomes unclear. This calculation is also consistent with the data, although it is not clear whether the non-collective excitations lead to an improvement due to the large error bars. The slope of the fusion cross sections at energies above the barrier becomes steeper by the noncollective excitations and the agreement with the data is worsened. However, this is not a serious problem because one can adjust the surface diffuseness parameter a in the nuclear potential so that the slope is consistent with the experimental data.

We have also performed a coupled-channels calculation for $^{28}\text{Si} + ^{90}\text{Zr}$ system to see the effect of the noncollective excitations of ^{90}Zr in different system. We have found that the noncollective excitations of ^{90}Zr nucleus have a minor effect on the barrier distribution as in the case of $^{20}\text{Ne} + ^{90}\text{Zr}$ scattering. That is, it smears the peak structure of the barrier distribution only slightly.

From these considerations, we argue that the noncollective excitations described in this model does not lead to an inconsistency with the previous analyses for the systems studied in this subsection.

In this subsection, we have investigated the effect of the noncollective excitations in systems

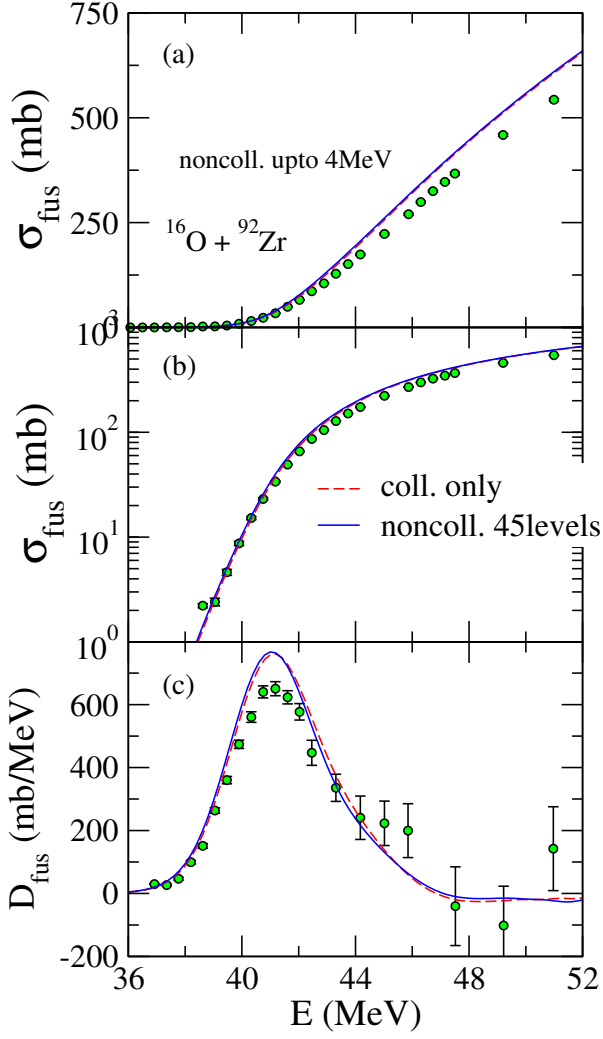


Figure 6.20: Fusion cross sections and the fusion barrier distribution for $^{16}\text{O} + ^{92}\text{Zr}$ system. The meaning of each line is the same as in the calculation for $^{20}\text{Ne} + ^{92}\text{Zr}$ system. The experimental data are taken from Ref. [94].

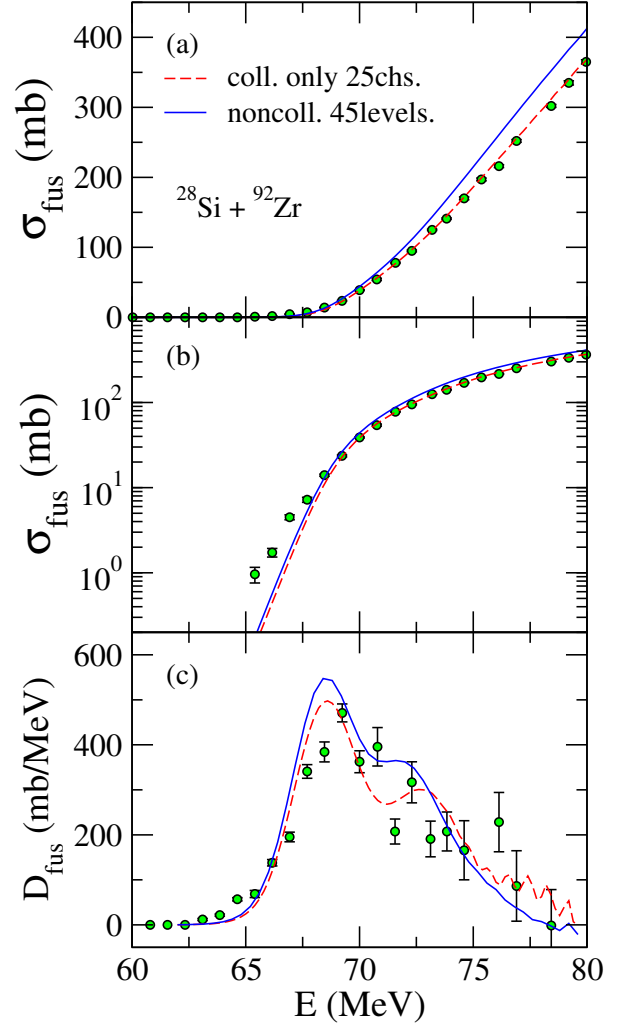


Figure 6.21: Same as Fig.6.20, but for $^{28}\text{Si} + ^{92}\text{Zr}$ system. The experimental data are taken from Ref. [94].

with different projectiles. We have seen that, depending on the type of the collective excitations in the projectile, the noncollective excitations affect the barrier distribution in a different way. In App. D, we present the study of the interplay of the collective and the noncollective excitations using a schematic model. This study shows that the noncollective excitations tend to shrink the distance between peaks of the barrier distribution, if the collective excitations, which dominates the barrier structure, are rotational excitations associated with a prolate deformation.

6.6 Prediction for $^{24}\text{Mg} + ^{90,92}\text{Zr}$ reaction

Before we close this chapter, we present the theoretical prediction for $^{24}\text{Mg} + ^{90,92}\text{Zr}$ reactions. The reason why we choose this system is that the ^{24}Mg is a strongly deformed nucleus with prolate

shape ($\beta_2 = 0.505$) and thus the similar noncollective effect on the barrier distribution can be expected as in the $^{20}\text{Ne} + ^{90,92}\text{Zr}$ system. In Figs.6.22 and 6.23, we show the fusion calculation for $^{24}\text{Mg} + ^{90,92}\text{Zr}$ systems. The meaning of the red dashed lines and the blue solid lines is the same as in Fig. 6.9. For the coupling to ^{24}Mg nucleus, we include the rotational states up to 6^+ state. For the nuclear potential, we use the Akyüz-Winther potential[89]. In the presence of only the collective excitations, the barrier distributions for the $^{24}\text{Mg} + ^{90,92}\text{Zr}$ systems exhibit similar behavior to those for the $^{20}\text{Ne} + ^{90,92}\text{Zr}$ systems. We can see that for $^{24}\text{Mg} + ^{90}\text{Zr}$ reaction, the effect of the noncollective excitations is not significantly large. It steepens the shoulder of the high energy part of the barrier distribution and fills the dip around 59 MeV. On the other hand, the noncollective excitations drastically change the behavior of the barrier distribution for $^{24}\text{Mg} + ^{92}\text{Zr}$ system. The effect of the noncollective excitations is similar to that in the $^{20}\text{Ne} + ^{92}\text{Zr}$ system, but stronger. This is because the charge product of $^{24}\text{Mg} + ^{92}\text{Zr}$ system and the deformation parameter β_2 of the projectile are larger than those of $^{20}\text{Ne} + ^{92}\text{Zr}$ system. If the fusion or quasi-elastic barrier distribution was measured for this system and the smeared structure was found for $^{24}\text{Mg} + ^{92}\text{Zr}$ system, the validity of our scenario would become clearer. However, the transfer processes may affect the barrier distribution for $^{24}\text{Mg} + ^{90,92}\text{Zr}$ differently, and in that case one should consider their effects as well.

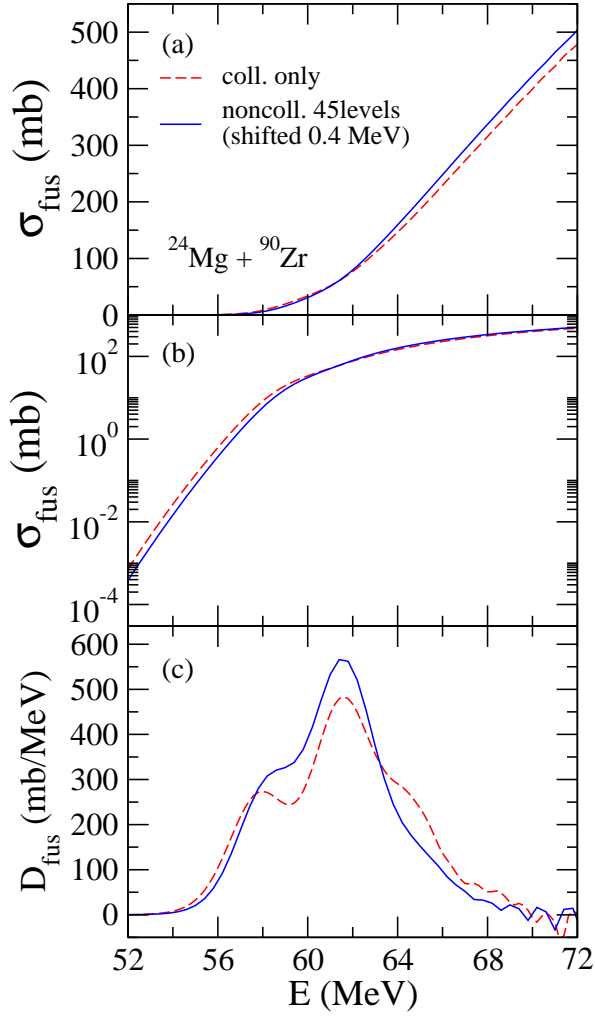


Figure 6.22: Fusion cross sections and fusion barrier distribution for $^{24}\text{Mg} + ^{90}\text{Zr}$ system. The meaning of each line is the same as in Fig.6.9.

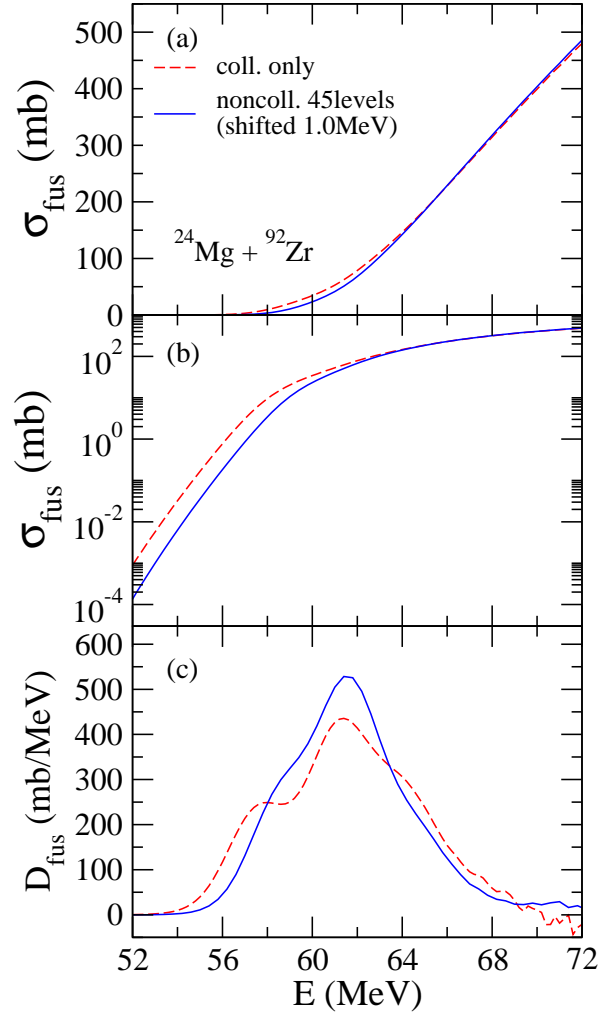


Figure 6.23: Same as Fig.6.22, but for $^{24}\text{Mg} + ^{92}\text{Zr}$ system.

Chapter 7

Summary and concluding remarks

We have investigated the role of noncollective excitations in heavy-ion fusion reaction and quasi-elastic scattering by explicitly taking into account the noncollective states in coupled-channels calculations. In chapter 5, we considered $^{16}\text{O} + ^{208}\text{Pb}$ system because this system has been studied both from the experimental and theoretical sides, and almost all the excited states of ^{208}Pb up to about 7 MeV have been identified by high precision proton inelastic scattering experiments. We used the experimentally obtained excitation energy, multipolarity, and deformation parameter of the excited states in ^{208}Pb to describe the noncollective excitations in $^{16}\text{O} + ^{208}\text{Pb}$ reaction.

Our results show that the barrier distribution for the fusion reaction and the quasi-elastic scattering are changed in a similar manner due to the noncollective excitations at energies above the Coulomb barrier. The energy dependence of the cross sections, on the other hand, is not affected much by the noncollective excitations and the degree of agreement with the experimental barrier distribution remains the same. The effect of anharmonicity of vibrational states in ^{208}Pb is also investigated. It has been found that the effect of anharmonicity plays a minor role regardless of the presence of the noncollective excitations.

The fusion calculations are also performed for the $^{32}\text{S} + ^{208}\text{Pb}$ and $^{40}\text{Ca} + ^{208}\text{Pb}$ systems in order to investigate the projectile mass-number dependence of the effect of the noncollective excitations. We have shown that the effect of the noncollective excitations becomes stronger as the mass number of the projectile nucleus increases. This result can be considered to justify the conventional coupled-channels calculation which neglects the noncollective excitations for relatively light systems. However, it also shows that the noncollective excitations should be considered in the calculation for heavy systems, for example, those relevant to a synthesis of superheavy elements.

For the $^{32}\text{S} + ^{208}\text{Pb}$ system, the coupled-channels calculations with only the inelastic excitations of the colliding nuclei do not account for the experimental data. That is, the subbarrier fusion cross sections are significantly underestimated for this system and the experimental barrier distribution is much more smeared than that obtained by the coupled-channels calculation. The transfer process should be taken into account for this system simultaneously with the noncollective excitations in order to improve the agreement with the data.

We have also calculated the energy dependence of the Q-value distribution for the $^{16}\text{O} + ^{208}\text{Pb}$ system and found that the contribution from the noncollective excitations becomes more and more important as the incident energy increases. This behaviour is qualitatively consistent with the experimental Q-value distribution for the same system. The experiment data also indicate the contribution from transfer channels in this system[27]. Therefore, it will be an interesting future work to study the contribution from the transfer channels to the Q-value distribution and compare with the experimental data in a quantitative way.

In chapter 6, we investigated quasi-elastic scattering for $^{20}\text{Ne} + ^{90,92}\text{Zr}$ systems where the conventional coupled-channels calculation fails to account for the experimental data. Although the experimental information on the noncollective states, especially deformation parameter, is available for ^{208}Pb nucleus, the information on the noncollective states for $^{90,92}\text{Zr}$ nuclei has not been sufficiently obtained. Thus, we employed the random matrix theory to describe the noncollective excitations in the coupled-channels calculation.

Our calculations show that the noncollective excitations fill the dip between the two peaks in the barrier distribution for $^{20}\text{Ne} + ^{92}\text{Zr}$ system and hence the peak structure is smeared. On the other hand, there is only a minor effect of the noncollective excitations for $^{20}\text{Ne} + ^{90}\text{Zr}$ system. As a consequence, the calculations simultaneously reproduce the experimental data for both systems. In these calculations, the parameters in the random matrix model, which determine the transition strength, are taken to be the same between the two systems. Therefore, the difference of the noncollective effect arises from the difference in the level density for the low-lying states which enters into the form factor in the coupling matrix elements in the random matrix model.

We also calculated the Q-value distribution for $^{20}\text{Ne} + ^{90,92}\text{Zr}$ scattering and compared with the experimental data taken at $E_{\text{CM}} = 51.85$ MeV. Our results show that the contribution from the noncollective excitations is so small in this energy that the calculated Q-value distribution is almost unchanged. We compared the Q-value distributions for $^{20}\text{Ne} + ^{90,92}\text{Zr}$ systems, and found that both the experimental data and the calculation indicate that the Q-value distributions at this energy do not differ much between the two systems. We also calculated the energy dependence of the Q-value distribution around the Coulomb barrier energy, and found that it shows the similar behavior to the $^{16}\text{O} + ^{208}\text{Pb}$ system. That is, while at energies below the Coulomb barrier, the contribution from the elastic and the collective channels is dominant, the contribution from the noncollective channels becomes more and more important as the incident energy increases. For $^{20}\text{Ne} + ^{92}\text{Zr}$ system, the noncollective excitations also contribute to construct a peak structure in the Q-value distribution at above barrier energies. Therefore, in order to see the effect of the noncollective excitations of Zr isotopes on the Q-value distribution, it will be necessary to measure the data above at barrier energies and see the energy dependence.

In order to see the effect of the noncollective excitations of ^{92}Zr on other reactions, we investigated $^{16}\text{O} + ^{92}\text{Zr}$ and ^{28}Si systems. For the $^{16}\text{O} + ^{92}\text{Zr}$ system, the noncollective excitations have

minor effect on the barrier distribution. For this system, the barrier distribution is not structured even in the absence of the noncollective excitations. Thus, the smearing due to the noncollective excitations does not change the shape of the barrier distribution. For the $^{28}\text{Si} + ^{92}\text{Zr}$ system, the noncollective excitations smear the barrier distribution. Although it seems to somewhat deteriorate the agreement with the experimental data, it will be more or less cured by readjusting the potential parameters, and thus we conclude that our calculations are not inconsistent with the previously measured data .

We finally investigated the $^{24}\text{Mg} + ^{90,92}\text{Zr}$ systems since ^{24}Mg is a prolately deformed nucleus, and a similar noncollective effect to $^{20}\text{Ne} + ^{90,92}\text{Zr}$ can be expected. That is, our calculation indicates a similar smearing effect for $^{24}\text{Mg} + ^{92}\text{Zr}$ system, while the barrier distribution for $^{24}\text{Mg} + ^{90}\text{Zr}$ system is not significantly changed by the noncollective excitations. Since the barrier distributions has not been obtained experimentally for this system, our calculation gives a prediction. If the experimental barrier distribution exhibits the smeared structure for $^{24}\text{Mg} + ^{92}\text{Zr}$ system, the importance of the noncollective excitations will become robust.

In this thesis, we have investigated the role of noncollective excitations in heavy-ion reactions for specific systems. We have seen that noncollective excitations often smear the barrier distribution. Our results show that in some systems, the effect of the noncollective excitations is important, e.g. $^{20}\text{Ne} + ^{92}\text{Zr}$ and $^{24}\text{Mg} + ^{92}\text{Zr}$ systems, while in other systems, e.g. in $^{16}\text{O} + ^{208}\text{Pb}$ and $^{20}\text{Ne} + ^{90}\text{Zr}$ systems, it is less important. It will be an interesting question to clarify a general criterion for a need to take into account the noncollective excitations. In this respect, we have clarified several conditions. The first is that the noncollective excitations should be taken into account for heavy systems such as those relevant to a synthesis of superheavy elements. This is because the coupling effect becomes effectively strong as the charge product of projectile and target becomes large. The second is that the noncollective excitations are important for systems with large number of levels or large level density at relatively low excitation energy region. This has been clarified from the comparison of $^{20}\text{Ne} + ^{90}\text{Zr}$ and $^{20}\text{Ne} + ^{92}\text{Zr}$ systems. And the third point is the properties of coexisting collective excitations which dominate the barrier structure. As in the case of $^{16}\text{O} + ^{92}\text{Zr}$ reaction, if the collective excitations do not yield a clear structure in the barrier distribution, the noncollective excitations do not significantly alter the barrier distribution. In order to proceed this study, it will be necessary to investigate systems where the effect of the noncollective excitations shows up in a different way, as in the case of $^{90,92}\text{Zr}$ targets.

We employed random matrix model to describe the noncollective excitations of $^{90,92}\text{Zr}$ because the experimental information on the noncollective states are limited. Another possible description of the noncollective excitations will be to calculate the excited states microscopically and use the theoretical transition probabilities. In such calculations, it will be necessary to take into account the paring effect for ^{92}Zr nucleus.

In our calculations for the $^{20}\text{Ne} + ^{90,92}\text{Zr}$ systems, we have not taken into account transfer reac-

tions because the experimental total transfer cross sections have been found to be almost the same between the two systems. However, if one looks at the cross sections for each transfer processes separately, they are different between these systems, which may affect the barrier distribution in a different way. Therefore, it is a challenging future work to study the effect of transfer processes as well as noncollective excitations. It will be also interesting to investigate the transfer effect on the Q-value distribution which has been suggested in the experiment for $^{16}\text{O} + ^{208}\text{Pb}$ system[27].

Acknowledgment

I would like to thank my supervisor Prof. Kouichi Hagino for his continuous support of my research throughout the period of graduate school. His suggestions and advices on my research were indispensable for me to reach a certain goal of this project. Daily discussion about nuclear physics had been very useful for proceeding my research. I would like to thank him also for many instructive advices after seminars, conferences and so on.

I would like to thank Prof. Shoichi Sasaki for fruitful discussions. I am very grateful for his advices on physics and seeking for my jobs. I would like to thank Dr. Akira Ono for consultation about computation. His advices on parallelization technique and computational troubles were indispensable for pursuing actual calculations. I thank all the other members of the nuclear theory group for daily discussions on various topics. These discussions were greatly instructed me and useful for my study and research activities.

This work was supported by the Global COE Program “Weaving Science Web beyond Particle-Matter Hierarchy” at Tohoku University.

Appendix A

Classical expression for fusion cross section and the Wong formula

In this appendix, we derive the classical expression for the fusion cross section and introduce the Wong formula, which is the fusion cross section for a parabolic potential.

The fusion cross section is given by the sum of penetrabilities for each partial wave as

$$\sigma_{\text{fus}}(E) = \frac{\pi}{k^2} \sum_{\ell=0}^{\infty} (2\ell + 1) P_{\ell}(E). \quad (\text{A.1})$$

In the classical limit, the penetrability is given by

$$\sigma_{\text{fus}}^{cl}(E) = \frac{\pi}{k^2} \sum_{\ell=0}^{\ell_c} (2\ell + 1) \theta(E - V_B) \quad (\text{A.2})$$

where ℓ_c is defined by

$$V_B + \frac{\ell_c(\ell_c + 1)\hbar^2}{2\mu R_B^2} = E. \quad (\text{A.3})$$

The step function enters into the expression because if $E < V_B$, there is no partial wave ℓ_c which satisfies Eq.(A.3) and the fusion cross section must be zero. By performing the sum, the fusion cross section reads

$$\begin{aligned} \sigma_{\text{fus}}^{cl}(E) &= \frac{\pi}{k^2} \ell_c(\ell_c + 2) \theta(E - V_B) \\ &\approx \frac{\pi}{k^2} \frac{2\mu R_B^2}{\hbar^2} (E - V_B) \theta(E - V_B) \\ &= \pi R_B^2 \left(1 - \frac{V_B}{E}\right) \theta(E - V_B). \end{aligned} \quad (\text{A.4})$$

In quantum mechanics, the fusion occurs even at subbarrier energies due to the quantum tun-

neling effect. If the potential can be approximated by a parabolic curve

$$V_\ell(r) \approx V_B - \frac{1}{2}\mu\Omega^2(r - R_B)^2 + \frac{\ell(\ell+1)\hbar^2}{2\mu R_B^2}, \quad (\text{A.5})$$

the penetration coefficient is given by[95]

$$t_n^\ell = \frac{1}{2} \left(e^{2i\phi_{n\ell}^I} - e^{2i\phi_{n\ell}^R} \right), \quad (\text{A.6})$$

where $\phi_{n\ell}^I$ and $\phi_{n\ell}^R$ are defined by

$$\phi_{n\ell}^I = \arg\Gamma\left(\frac{3}{4} - \frac{1}{2}ib_n^\ell\right) - \frac{3}{8}\pi \quad (\text{A.7})$$

$$\phi_{n\ell}^R = \arg\Gamma\left(\frac{1}{4} - \frac{1}{2}ib_n^\ell\right) - \frac{1}{8}\pi \quad (\text{A.8})$$

$$b_n^\ell = \frac{E - V_B^\ell}{\hbar\Omega} \quad (\text{A.9})$$

$$V_B^\ell = V_B + \frac{\ell(\ell+1)\hbar^2}{2\mu R_B^2}. \quad (\text{A.10})$$

Here, $\Gamma(z)$ is a gamma function. The penetrability is, as is well known, given by

$$P(E) = |t_{n\ell}|^2 = \frac{1}{1 + \exp\left(\frac{2\pi(V_B^\ell - E)}{\hbar\Omega}\right)}. \quad (\text{A.11})$$

The fusion cross section is then calculated as

$$\begin{aligned} \sigma_{\text{fus}}(E) &= \frac{\pi}{k^2} \sum_{\ell=0}^{\infty} (2\ell+1) P_\ell(E) \\ &\approx \frac{\pi}{k^2} \int_0^{\infty} d\ell (2\ell+1) P_\ell(E) \\ &= \frac{\hbar\Omega}{2E} R_B^2 \ln \left[1 + \exp\left(\frac{2\pi}{\hbar\Omega}(E - V_B)\right) \right]. \end{aligned} \quad (\text{A.12})$$

This expression was derived by Wong[64], and the fusion barrier distribution is given by

$$\frac{1}{\pi R_B^2} \frac{d^2(E\sigma_{\text{fus}})}{dE^2} = \frac{2\pi}{\hbar\Omega} \frac{\exp\left(\frac{2\pi}{\hbar\Omega}(E - V_B)\right)}{\left[1 + \exp\left(\frac{2\pi}{\hbar\Omega}(E - V_B)\right)\right]^2}. \quad (\text{A.13})$$

For this barrier distribution, the FWHM is given by $0.56\hbar\Omega$. If one considers a classical limit $\hbar \rightarrow 0$, Eq. (A.12) becomes

$$\begin{aligned} \sigma_{\text{fus}}(E) &\approx \frac{\hbar\Omega}{2E} R_B^2 \ln \left[\exp\left(\frac{2\pi}{\hbar\Omega}(E - V_B)\right) \right] \\ &= \pi R_B^2 \left(1 - \frac{V_B}{E} \right) \end{aligned} \quad (\text{A.14})$$

for $E > V_B$ and

$$\begin{aligned}\sigma_{\text{fus}}(E) &\approx \frac{\hbar\Omega}{2E} R_B^2 \ln 1 \\ &= 0\end{aligned}\tag{A.15}$$

for $E < V_B$. This is nothing but the classical expression Eq. (A.4). Notice that the classical limit, Eq. (A.14), can be achieved also when $E \gg V_B$.

We show a comparison of the exact calculation and the Wong formula for $^{20}\text{Ne} + ^{90}\text{Zr}$ system. For the nuclear potential, we use a Woods-Saxon potential

$$V(r) = -\frac{V_0}{1 + \exp((r - R_n)/a)}.\tag{A.16}$$

The curvature of the parabolic potential is calculated according to

$$\Omega = \sqrt{-\frac{1}{\mu} \frac{d^2 V}{dr^2} \Big|_{r=R_B}}\tag{A.17}$$

$$= -\frac{1}{\mu} \left(\frac{V_0}{a^2} \frac{e^x}{[1 + e^x]^2} - \frac{2V_0}{a^2} \frac{e^{2x}}{[1 + e^x]^3} + \frac{2Z_P Z_T e^2}{r^3} \right),\tag{A.18}$$

where $x = (r - R_B)/a$.

In Fig. A.1, we show the resulting Coulomb barrier and its parabolic approximation by the blue solid and the red dashed lines, respectively. We can see that the exact potential exhibits moderate slope on the right hand side of the barrier due to the Coulomb potential. In Fig. A.2, we show the fusion cross section in the upper panel and the corresponding fusion barrier distribution in the lower panel. In calculating the barrier distribution, we have replaced the differentiation with a finite difference of 2 MeV. We show the exact results by the blue solid lines and the results from the Wong formula by the red lines. For comparison, we show the classical fusion cross section by the black dotted line. We can see that at above barrier energies, the quantum mechanical calculations almost coincide with the classical cross sections. Below the barrier, the Wong formula overestimates the exact calculation. This reflects the smaller width of the parabolic potential barrier. The corresponding barrier distributions show almost the same behavior since the width of the barrier distribution is almost determined by the barrier curvature for which the Wong formula has the same value as the exact potential.

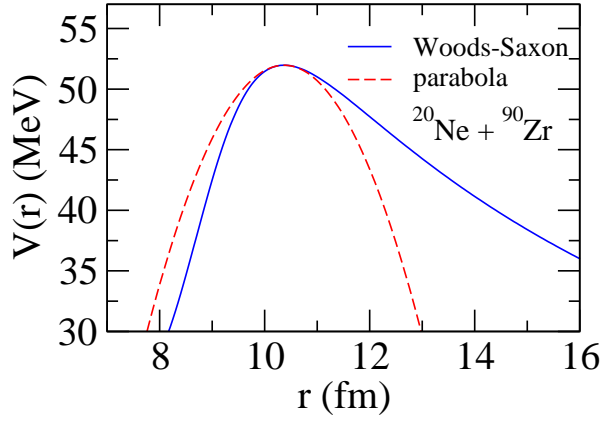


Figure A.1: Potential barrier for $^{20}\text{Ne} + ^{90}\text{Zr}$ system (the blue solid line) and the parabolic curve (the red dashed line) which approximates the exact potential barrier.

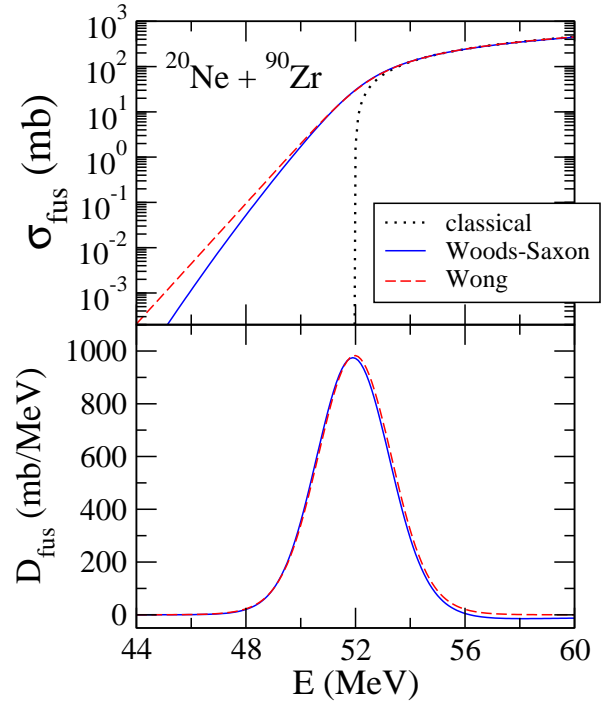


Figure A.2: The upper panel: Exact fusion cross sections for $^{20}\text{Ne} + ^{90}\text{Zr}$ system (the blue solid curve) and fusion cross sections from the Wong formula (the red dashed curve). The black dotted line is the classical fusion cross sections. The lower panel: Corresponding fusion barrier distributions.

Appendix B

Role of noncollective excitations in one-dimensional barrier penetration problem

In this appendix, we apply the random matrix model to a one-dimensional barrier penetration problem and discuss the role of noncollective excitations[88].

B.1 Random matrix model for one-dimensional coupled-channels equations

We consider the following coupled-channels equations

$$\left\{ -\frac{\hbar^2}{2\mu} \frac{d^2}{dx^2} + V_{\text{rel}}(x) + \epsilon_n - E \right\} \psi_n(x) + \sum_m V_{nm}(x) \psi_m(x) = 0. \quad (\text{B.1})$$

Here, μ is the reduced mass, $V_{\text{rel}}(x)$ is a potential for the relative motion, and ϵ_n is an excitation energy for the n th channel.

We impose the following boundary condition

$$\psi_n(x) \rightarrow \delta_{n,0} e^{-ik_0 x} + r_n e^{ik_n x} \quad \text{for } x \rightarrow +\infty \quad (\text{B.2})$$

$$\rightarrow t_n e^{-ik_n x} \quad \text{for } x \rightarrow -\infty, \quad (\text{B.3})$$

where $k_n = \sqrt{2\mu(E - \epsilon_n)/\hbar^2}$ is the wave number for the n th channel, and 0 represents the entrance channel. We have assumed that the projectile is incident from the right hand side of the potential barrier. With the transmission coefficients t_n , the penetration probability for the inclusive process is calculated as

$$P(E) = \sum_n P_n(E) = \sum_n \frac{k_n}{k_0} |t_n|^2. \quad (\text{B.4})$$

The barrier distribution is obtained by taking the energy derivative of $P(E)$, that is, $dP(E)/dE$ [65].

We solve the coupled-channels equations Eq. (B.1) using the constant coupling approximation by including both collective and noncollective excitations. For the collective excitation, we assume the vibrational coupling, whose matrix element is given by

$$(V_{nm}) = F \begin{pmatrix} 0 & 1 \\ 1 & 0 \end{pmatrix}, \quad (\text{B.5})$$

where F is a constant.

For the noncollective excitations, we consider an ensemble of coupling matrix elements based on the random matrix theory [47, 48, 49]. We assume that the matrix elements are uncorrelated random numbers obeying a Gaussian distribution with zero mean. That is, we require that the first and the second moments of the coupling matrix elements satisfy the following equations [44]

$$\overline{V_{nm}(x)} = 0 \quad (\text{B.6})$$

$$\overline{V_{rs} V_{nm}} = (\delta_{r,n} \delta_{s,m} + \delta_{r,m} \delta_{s,n}) g_{nm} \quad (\text{B.7})$$

$$g_{nm} = \frac{w_0}{\sqrt{\rho(\epsilon_n) \rho(\epsilon_m)}} e^{-\frac{(\epsilon_n - \epsilon_m)^2}{2\Delta^2}}, \quad (\text{B.8})$$

where the overline denotes an ensemble average and $\rho(\epsilon)$ is the nuclear level density. Here, we have assumed the coordinate independent matrix elements according to the constant coupling approximation.

For the noncollective excitations, we generate the coupling matrix elements according to these equations many times. For each coupling matrix, we do not vary the matrix elements for the collective excitations, which are uniquely determined once the coupling is specified. For each coupling matrix, we solve the coupled-channels equations and calculate the penetrability and the reflection probability. The physical results are then obtained by taking an average of these quantities.

B.2 Results

In solving the coupled-channels equations, we assume that there is a collective vibrational state at 1 MeV, whose coupling to the ground state is given by Eq. (B.5) with $F = 2$ MeV. For the noncollective states, we consider a level density given by $\rho(\epsilon) = \rho_0 e^{2\sqrt{a\epsilon}}$ with $\rho_0 = 0.039 \text{ MeV}^{-1}$ and $a = 29/8 \text{ MeV}^{-1}$, starting from 2 MeV. The value of ρ_0 was determined so that the number of noncollective levels is 200 up to 5 MeV. For the parameters for the couplings in Eq. (B.8), we follow Ref. [44] to use $\Delta = 7$ MeV. We arbitrarily choose the coupling strength to be $w_0 = 0.005$ MeV. The energy spectrum for this model is shown in Fig.B.1. For the potential for the relative motion, $V_{\text{rel}}(x)$, we use a Gaussian function

$$V_{\text{rel}}(x) = V_B e^{-\frac{x^2}{2x_0^2}}, \quad (\text{B.9})$$

with $V_B = 100$ MeV and $s_0 = 3$ fm [5]. The reduced mass μ is taken to be $29m_N$, m_N being the nucleon mass.

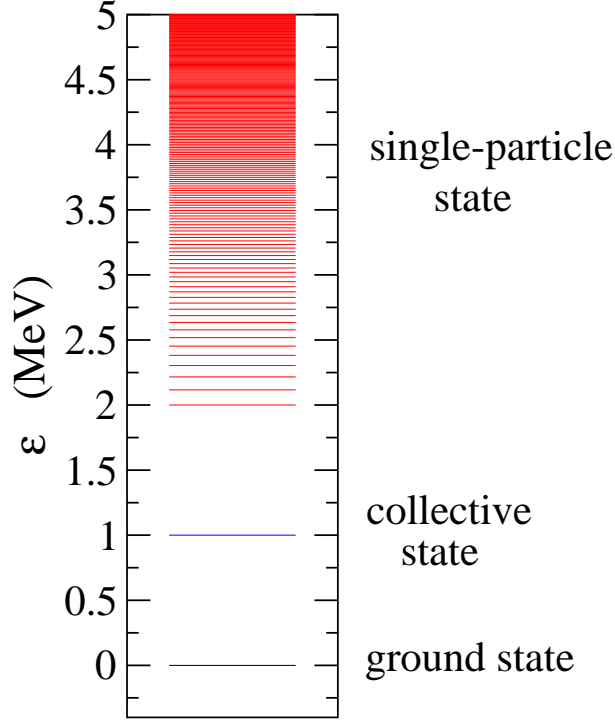


Figure B.1: The energy spectrum for the model calculation which we employ. There is a collective vibrational state at 1 MeV, while noncollective states exist from 2 MeV with an exponentially increasing level density.

Figure B.2 shows the penetrabilities thus obtained. The corresponding barrier distributions are shown in Fig. B.3. The dotted and the dashed lines show the results without the channel couplings and those only with the collective excitation, respectively. The solid line shows the results with both the noncollective excitations and the collective excitation. We include the noncollective states up to $\epsilon_{\max} = 23$ MeV with energy spacing of $\Delta\epsilon = 0.02$ MeV. This result is obtained by generating the coupling matrix elements 30 times to take an ensemble average.

The collective excitation leads to a double peaked structure of barrier distribution. One can see that the noncollective excitations suppress the penetrability at energies above the barrier, and at the same time smear the higher energy peak in the barrier distribution, although the main structure of the barrier distribution is still determined by the collective excitation. The noncollective excitations also lower the barrier and thus increase the penetrability at energies below the barrier, due to the potential renormalization discussed in chapter 3.

The Q -value distribution for the reflected flux is shown in Fig. B.4 at four incident energies indicated in the figure. For a presentation purpose, we fold the discrete distribution with a Lorentz

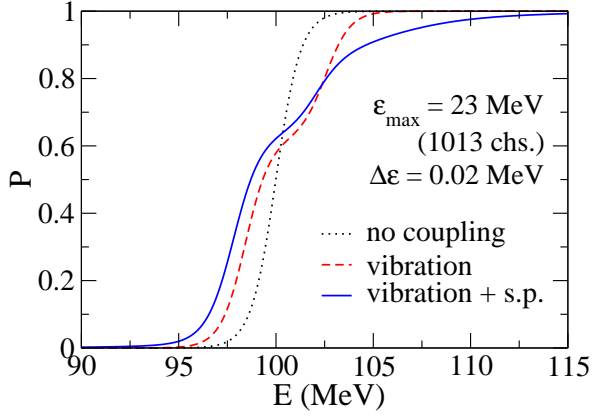


Figure B.2: The potential penetrability obtained with several methods. The dotted line is obtained without channel coupling, while the dashed line takes into account only the collective vibrational excitation. The solid line shows the result with both the collective and the noncollective excitations.

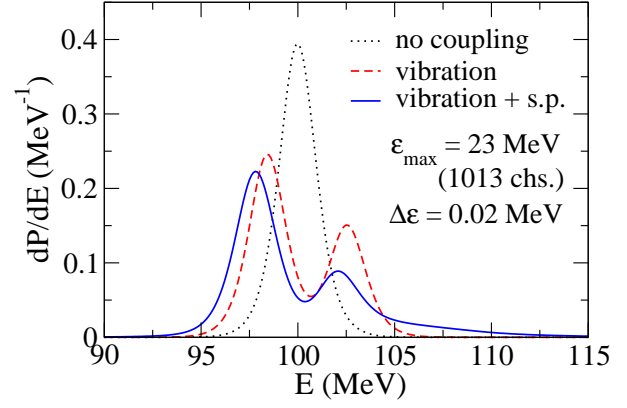


Figure B.3: The barrier distribution defined by the first derivative of the penetrability. The meaning of each line is the same as in Fig.B.2.

function,

$$f(\epsilon) = \frac{1}{\pi} \frac{\eta}{\epsilon^2 + \eta^2}, \quad (\text{B.10})$$

with the width of $\eta = 0.2$ MeV. In the figure, the peaks at $E^* = 0$ MeV and $E^* = 1$ MeV correspond to the elastic channel and the collective excitation channel, respectively. One can see that at energies well below the barrier the elastic and the collective peaks dominate in the distribution. As the energy increases, the single-particle excitations become more and more important. This behaviour is consistent with the experimental Q -value distribution observed for $^{16}\text{O} + ^{208}\text{Pb}$ [25, 26] and $^{16}\text{O} + ^{184}\text{W}$ [26] reactions. At energies above the barrier, the noncollective contribution is even larger than the contribution of the elastic and the collective peaks.

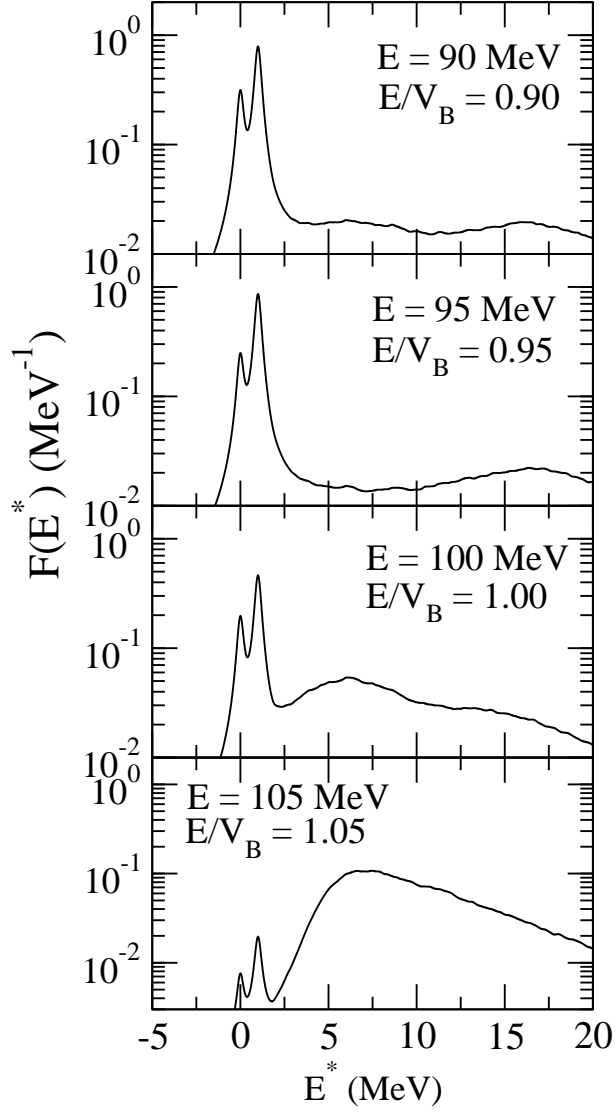


Figure B.4: The Q -value distribution for the reflected flux at four energies as indicated in the figure. It is obtained by smearing the discrete distribution with a Lorentzian function with the width of 0.2 MeV. The peaks at $E^*=0$ MeV and 1 MeV correspond to the elastic and the collective excitation channels, respectively.

Appendix C

Calculation of gaussian orthogonal ensemble(GOE)

In this appendix, we present a calculation method for the coupling matrix elements according to the random matrix theory[96]. The second moment of the coupling matrix elements is assumed to be given by Eq. (6.9) as

$$\begin{aligned} \overline{V_{nn'}^{II'}(r)V_{n'n''}^{I'I''}(r')} &= \{\delta_{nn''}\delta_{n'n'''}\delta_{II''}\delta_{I'I'''} + \delta_{nn'''}\delta_{n'n''}\delta_{II'''}\delta_{I'I''}\} \sqrt{(2I+1)(2I'+1)} \\ &\times \sum_{\lambda} \begin{pmatrix} I & \lambda & I' \\ 0 & 0 & 0 \end{pmatrix}^2 \alpha_{\lambda}(n, n'; I, I'; r, r') \end{aligned} \quad (\text{C.1})$$

with the form factor

$$\alpha_{\lambda}(n, n'; I, I'; r, r') = \frac{w_{\lambda}}{\sqrt{\rho(n, I)\rho(n', I')}} e^{-\frac{(\epsilon_n - \epsilon_{n'})^2}{2\Delta^2}} e^{-\frac{(r-r')^2}{2\sigma^2}} h(r)h(r'). \quad (\text{C.2})$$

In order to construct $V_{nn'}^{II'}(r)$ which satisfies Eq. (C.1), we define the following function

$$g_{nn'}^{II'}(r, r') = \sqrt{\sum_{\lambda} \begin{pmatrix} I & \lambda & I' \\ 0 & 0 & 0 \end{pmatrix}^2 w_{\lambda} \sqrt{\frac{(2I+1)(2I'+1)}{\rho(n, I)\rho(n', I')}}} e^{-\frac{(\epsilon_n - \epsilon_{n'})^2}{4\Delta^2}} h(r) \left(\frac{2}{\pi\sigma^2}\right)^{1/4} e^{-\frac{(r-r')^2}{\sigma^2}}, \quad (\text{C.3})$$

which corresponds to the "square root" of the form factor α_{λ} . Using this function, the coupling matrix element is calculated as

$$V_{nn'}^{II'}(r) = \int dr' g_{nn'}^{II'}(r, r') w_{nn'}^{II'}(r'), \quad (\text{C.4})$$

where $w_{nn'}(r)$ is a gaussian random number which satisfies

$$\overline{w_{n_1 n_2}(r)w_{n_3 n_4}(r')} = (\delta_{n_1 n_3}\delta_{n_2 n_4} + \delta_{n_1 n_4}\delta_{n_2 n_3})\delta(r - r'). \quad (\text{C.5})$$

The gaussian random numbers can be generated from uniform random numbers distributed in the interval (0, 1] by, for instance, the Box-Muller method. That is, from the independent random

numbers x_1 and x_2 uniformly distributed in the interval $(0, 1]$, the independent random numbers y_1 and y_2 with a gaussian distribution are generated by the following equations[97]

$$y_1 = \sqrt{-2\ln x_1} \cos(2\pi x_2) \quad (\text{C.6})$$

$$y_2 = \sqrt{-2\ln x_1} \sin(2\pi x_2). \quad (\text{C.7})$$

It is a straightforward task to verify that the coupling matrix element defined by Eq. (C.4) satisfies Eq. (C.1).

Appendix D

Interplay of collective and noncollective excitations

In this appendix, we discuss the interplay of collective and noncollective excitations by using a schematic model. Depending on the type of the collective excitations which dominate the barrier structure, the effect of the noncollective excitations on the barrier distribution appears differently. In order to investigate this difference, we consider three cases where the collective excitations are vibration, rotation associated with a prolate deformation, and rotation associated with an oblate deformation. We also use the perturbation theory to give an interpretation for the effect of the noncollective excitations on the barrier distribution. The purpose of this appendix is to gain an insight of the smearing effect of the noncollective excitations observed in the $^{20}\text{Ne} + ^{92}\text{Zr}$ system, where the rotational excitations with prolate deformation dominate the barrier structure. To this end, we use a constant coupling approximation and work in the eigenchannel representation, which makes an interpretation of the noncollective effects transparent. In this representation, we shall see whether the shrinkage of the peaks in the barrier distribution, which leads to the smearing of the barrier structure, occurs due to the noncollective excitations. Although we consider the collision of $^{20}\text{Ne} + ^{92}\text{Zr}$ system, the collective excitation channels are artificially modified for ^{92}Zr nucleus, while the realistic noncollective states of ^{92}Zr are included in the same way as in the calculations shown in chapter 6. ^{20}Ne is assumed to be inert.

We first consider the rotational excitations. We set the excited states with the excitation energy $\epsilon_2 = 0.4$ MeV and the deformation parameter $\beta_2 = \pm 0.25$. The potential parameters are the same as in the previous calculations for $^{20}\text{Ne} + ^{92}\text{Zr}$ system. We show the fusion barrier distributions for the case of prolate deformation ($\beta_2 > 0$) in Figs. D.1(a) and D.2(a) and oblate deformation ($\beta_2 < 0$) in Figs. D.3(a) and D.4(a). The red lines include only the collective excitations and the blue lines include the noncollective excitations in addition to the collective excitations. Fig. D.1 shows the results when the rotational states are truncated at the 2^+ state and Fig. D.2 takes into account up to the 4^+ state. As mentioned in chapter 3, we can introduce the eigenchannel representation when the constant coupling approximation is employed. The magenta and the cyan spectra represent

eigenbarriers respectively for the red and the blue calculations. In Fig.D.1(a), the difference of the height of the two eigenbarriers is $\Delta\lambda = 5.14$ MeV as indicated in the figure. If we take into account the noncollective excitations, the difference decreases and becomes $\Delta\lambda = 4.71$ MeV. This is also the case if one include the rotational 4^+ states in addition, that is, the distance between the lowest two eigenbarriers decreases.

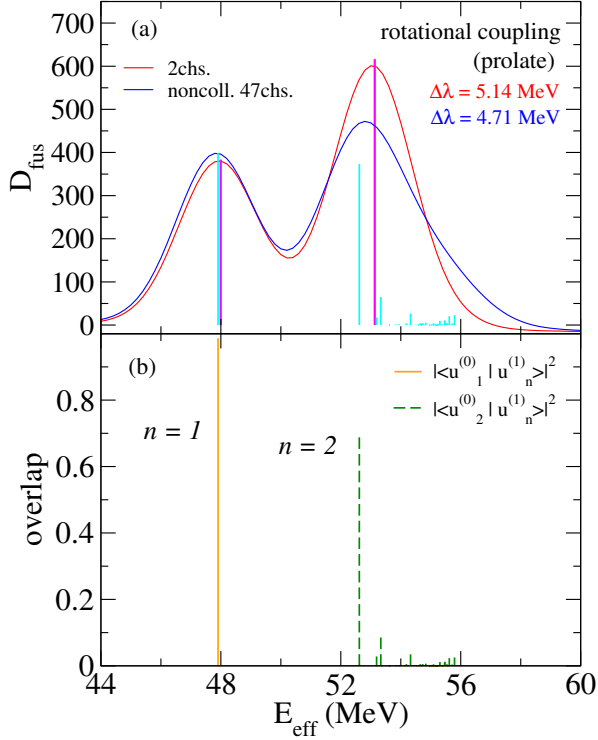


Figure D.1: The upper panel: Fusion barrier distributions for a rotational coupling associated with a prolate deformation. The rotational states are included up to the 2^+ state. The red line includes only the collective excitations while the blue one includes also the noncollective excitations. The pink and the cyan spectra represent the position of the eigenbarriers corresponding to the red and the blue lines, respectively. The lower panel: The overlap of the perturbed and the unperturbed eigenvectors for a prolate rotational coupling. The orange and the purple lines represent the overlap with the eigenvector belonging to the lowest and the second lowest unperturbed eigenvalues, respectively.

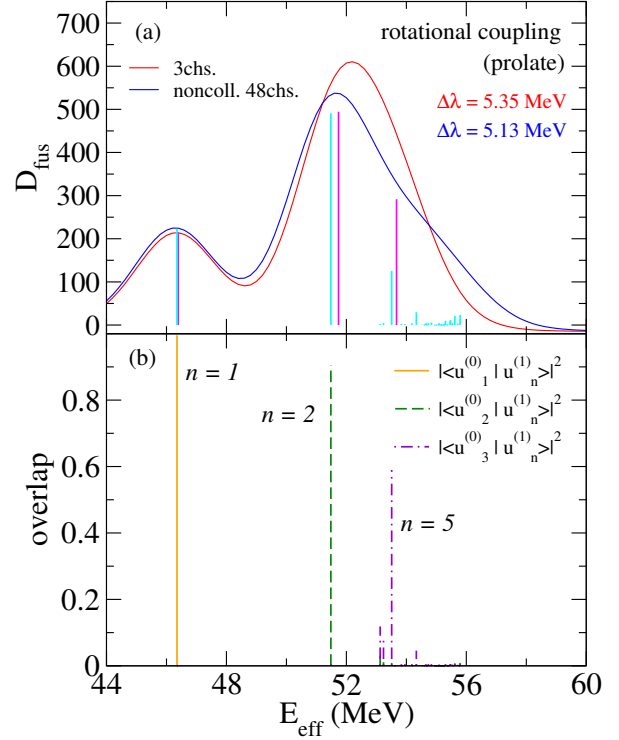


Figure D.2: Same as Fig. D.1, but with the 4^+ state in the rotational coupling. The green lines in the lower panel represent the overlap with the eigenvector belonging to the third lowest unperturbed eigenvalues.

We show the overlap spectra for prolate deformation case in Figs. D.1(b) and D.2(b) and oblate deformation cases in Figs. D.3(b) and D.4(b). The orange, the green, and the purple (only in Figs. D.2(b) and D.4(b)) lines are the overlap between the unperturbed (in the absence of the noncollec-

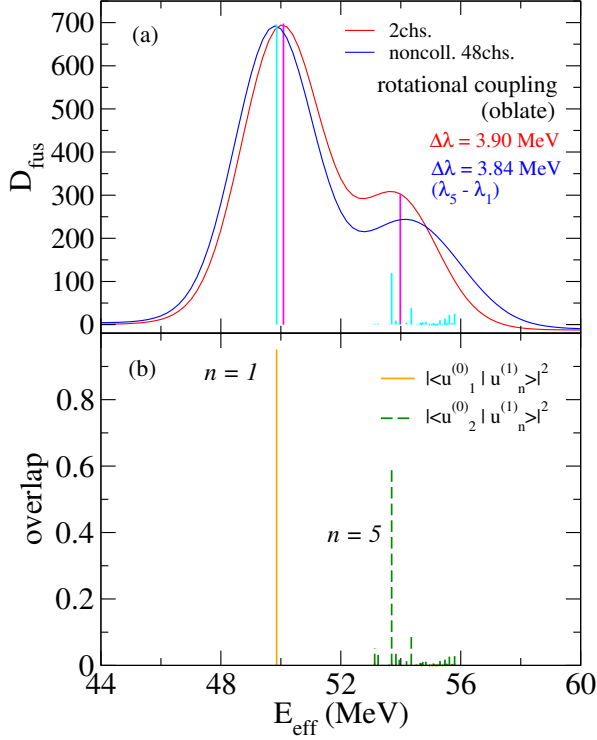


Figure D.3: Same as Fig.D.1, but for an oblate deformation.

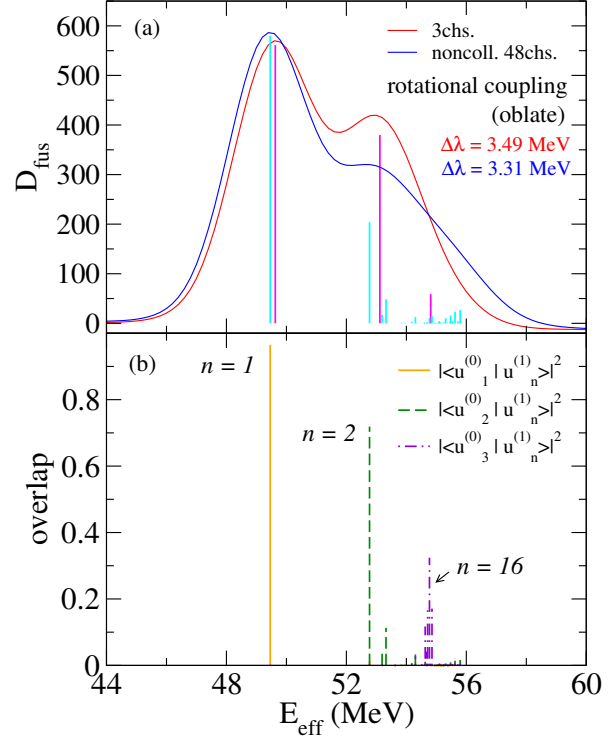


Figure D.4: Same as Fig.D.2, but with an oblate deformation.

tive excitations) and the perturbed (in the presence of the noncollective excitations) eigenvectors. The horizontal axis represents the height of the eigenbarriers in the presence of the noncollective excitations. We can see that the unperturbed eigenvector for the lowest eigenbarrier has largest overlap with the perturbed eigenvector for $n = 1$, that is, the lowest eigenbarrier. Similarly, the unperturbed eigenvector for the second lowest eigenbarrier has the largest overlap with the perturbed eigenvector for $n = 2$.

For an oblate deformation with the 0^+ and 2^+ states, we can see that by including the noncollective excitations, the distance between the eigenbarriers becomes slightly smaller. On the other hand, including the rotational states up to the 4^+ state, the higher peak is fragmented and the distance of the peaks in the barrier distribution appears to be broadened by including the noncollective excitations, in contrast to the prolate case. A similar behavior can be observed for the vibrational coupling case. In Figs. D.5 and D.6, we show the same calculation for the vibrational coupling case. We assume that the vibrational 2^+ state is located at $\epsilon_2 = 1.0$ MeV in ^{92}Zr nucleus with a deformation parameter of $\beta_2 = 0.25$. Fig. D.5 includes only one phonon state for the vibrational coupling and Fig. D.6 includes the two phonon state in addition to the one phonon state. The meaning of each line is the same as the rotational case. Although the distance between the eigenbarriers becomes smaller (4.18 MeV to 3.91 MeV) by including the noncollective excitations, the peak distance of the barrier distribution appears to be broadened. The highest eigenbarrier gains a relatively large weight both for the rotational coupling with oblate deformation and vibrational

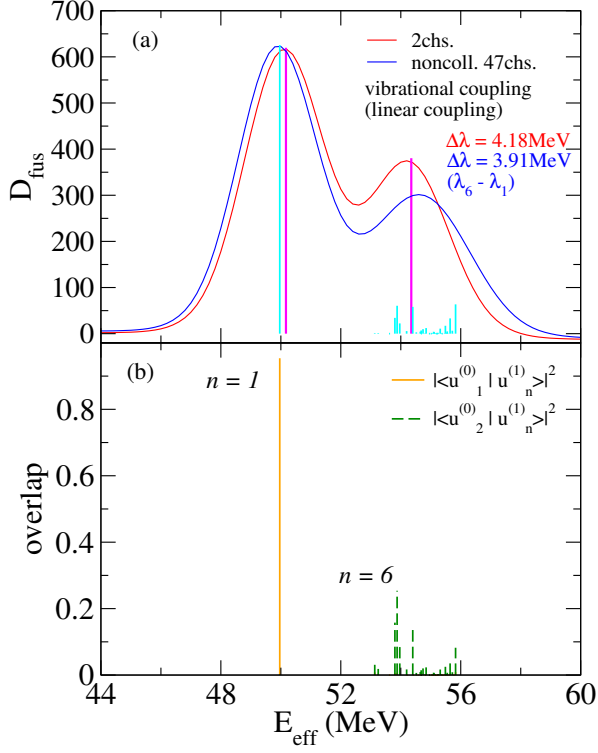


Figure D.5: Same as Fig. D.1, but with a vibrational coupling.

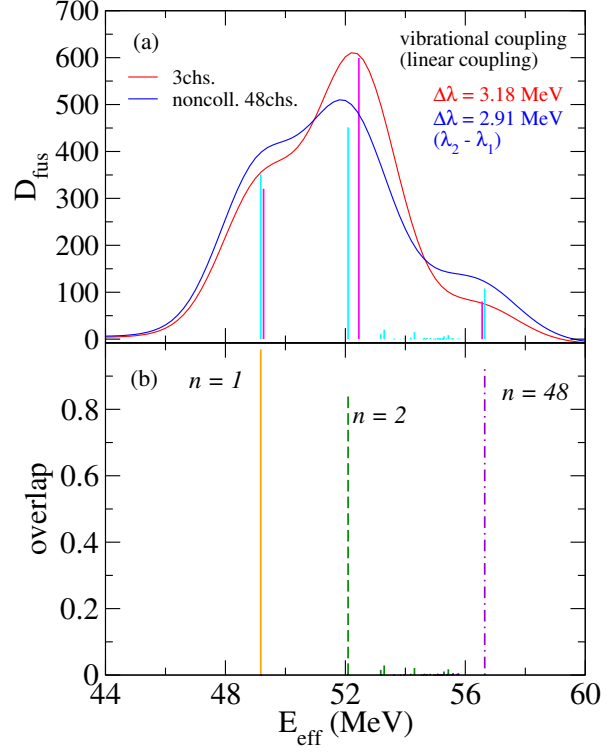


Figure D.6: Same as Fig. D.2, but with a vibrational coupling.

coupling cases, and this makes the peak distance broad. However, for the rotational coupling with a prolate deformation, the highest eigenbarrier does not broaden the main peaks. This is because in the prolate deformation case, the higher eigenbarrier has a larger weight in the unperturbed calculation, and the highest eigenbarrier which appears in the perturbed calculation only smear the higher peak of the barrier distribution and does not broaden the peak distance.

We can give some explanation to the shrinkage of the peak distance for the rotational coupling with a prolate deformation according to the perturbation theory. The coupling matrix in the present calculation has the following form

$$V = (V_{\text{coll}} + \epsilon) + V_{\text{RMT}} \quad (\text{D.1})$$

with

$$V_{\text{coll}} + \epsilon = \begin{pmatrix} 0 & f & 0 & 0 & \cdots \\ f & g & 0 & 0 & \cdots \\ 0 & 0 & \epsilon_3 & 0 & \cdots \\ 0 & 0 & 0 & \epsilon_4 & \cdots \\ \vdots & \vdots & \vdots & \vdots & \ddots \end{pmatrix} \quad (\text{D.2})$$

and

$$V_{\text{RMT}} = \begin{pmatrix} 0 & 0 & c_3 & c_4 & \cdots \\ 0 & 0 & 0 & 0 & \cdots \\ c_3 & 0 & 0 & 0 & \cdots \\ c_4 & 0 & 0 & 0 & \cdots \\ \vdots & \vdots & \vdots & \vdots & \ddots \end{pmatrix}. \quad (\text{D.3})$$

The first matrix represents the coupling matrix related to the collective excitation plus excitation energy (the unperturbed part), and the second matrix represents the coupling matrix related to the noncollective excitations (the perturbed part). The numbers f, g, c_3, c_4, \dots represent the coupling strength (g includes the excitation energy of the collective state ϵ_2), and $\epsilon_3, \epsilon_4, \dots$ represents the excitation energies of the noncollective states. One can diagonalize the unperturbed coupling matrix by some unitary matrix U as

$$U \{V_{\text{coll}} + \epsilon\} U^\dagger = \begin{pmatrix} \lambda_1^{(0)} & 0 & 0 & \cdots \\ 0 & \lambda_2^{(0)} & 0 & \cdots \\ 0 & 0 & \lambda_3^{(0)} & \cdots \\ \vdots & \vdots & \vdots & \ddots \end{pmatrix}, \quad (\text{D.4})$$

and the unitary matrix U has the form

$$U = (u_1^{(0)}, u_2^{(0)}, u_3^{(0)}, \dots) = \begin{pmatrix} u_{11}^{(0)} & u_{12}^{(0)} & 0 & 0 & \cdots \\ u_{21}^{(0)} & u_{22}^{(0)} & 0 & 0 & \cdots \\ 0 & 0 & 1 & 0 & \cdots \\ 0 & 0 & 0 & 1 & \cdots \\ \vdots & \vdots & \vdots & \vdots & \ddots \end{pmatrix}. \quad (\text{D.5})$$

Note that $\lambda_m^{(0)} = \epsilon_m$ for $m \geq 3$. Here, we make an assumption that $\lambda_2^{(0)} \leq \lambda_m^{(0)} (m \geq 3)$. The first order perturbation theory gives zero and the second order perturbation gives

$$\lambda'_n = \lambda_n^{(0)} + \sum_{m \neq n} \frac{|\langle u_n^{(0)} | V_{\text{RMT}} | u_m^{(0)} \rangle|^2}{\lambda_n^{(0)} - \lambda_m^{(0)}}. \quad (\text{D.6})$$

We consider the difference of λ'_1 and λ'_2 . It is given by

$$\lambda'_2 - \lambda'_1 = \lambda_2^{(0)} - \lambda_1^{(0)} + \sum_{m \geq 3} \frac{\lambda_1^{(0)} - \lambda_m^{(0)} + (2\lambda_m^{(0)} - \lambda_1^{(0)} - \lambda_2^{(0)}) u_{11}^{(0)2}}{(\lambda_1^{(0)} - \lambda_m^{(0)})(\lambda_2^{(0)} - \lambda_m^{(0)})} c_m^2 \quad (\text{D.7})$$

From this equation, we can say that if

$$u_{11}^{(0)2} \leq \frac{\lambda_m^{(0)} - \lambda_1^{(0)}}{2\lambda_m^{(0)} - \lambda_1^{(0)} - \lambda_2^{(0)}} \quad (\text{D.8})$$

is satisfied for at least all $m \geq 3$, then

$$\lambda'_2 - \lambda'_1 \leq \lambda_2^{(0)} - \lambda_1^{(0)}, \quad (\text{D.9})$$

that is, the distance of the eigenbarrier becomes smaller. Notice that the left hand side of the condition (D.8) is the weight factor for the lowest eigenbarrier. In the case of a rotational coupling with a prolate deformation considered above, the assumption with respect to the ordering of $\lambda_n^{(0)}$ is satisfied. In addition, from

$$\frac{\lambda_m^{(0)} - \lambda_1^{(0)}}{2\lambda_m^{(0)} - \lambda_1^{(0)} - \lambda_2^{(0)}} \geq \frac{\lambda_m^{(0)} - \lambda_1^{(0)}}{2(\lambda_m^{(0)} - \lambda_1^{(0)})} = \frac{1}{2}, \quad (\text{D.10})$$

and the fact that the lower eigenbarrier has a smaller weight factor than that of the higher one in the case of prolate deformation, the condition (D.8) is satisfied. Thus, the perturbation theory predicts the shrinkage of the distance between the eigenbarriers, and as we have seen above, this is the case. For the case of a rotational coupling with an oblate deformation and a vibrational coupling, the lower eigenbarrier has a larger weight factor and the condition (D.8) is not necessarily satisfied, even if the assumption with respect to the ordering of the eigenbarriers is satisfied. Thus, we cannot draw a definite conclusion in contrast to the prolate deformation case.

Generally speaking from the discussion in this sections, it is clear that the shrinkage of the peak distance due to the noncollective excitations, which leads to the smearing of the peak structure, tends to be occurred for the reaction with the rotational coupling associated with prolate deformation.

Bibliography

- [1] A. O. Caldeira and A. J. Leggett, Phys. Rev. Lett. **46**, 211(1981).
- [2] A. O. Caldeira and A. J. Leggett, Ann. of Phys. **149**, 374(1983).
- [3] M. Dasgupta, D.J. Hinde, N. Rowley, and A.M. Stefanini, Annu. Rev. Nucl. Part. Sci. **48**, 401(1998).
- [4] L. R. Leigh, M. Dasgupta, D. J. Hinde, J. C. Mein, C. R. Morton, R. C. Lemmon, J. P. Lestone, J. O. Newton, H. Timmers, J. X. Wei, and N. Rowley, Phys. Rev. C **52**, 3151(1995).
- [5] C. H. Dasso, S. Landowne, and A. Winther, Nucl. Phys. **A405**, 381 (1983); **A407**, 221 (1983).
- [6] N. Rowley, G. R. Satchler and P. H. Stelson, Phys. Lett. **B254** 25, (1991).
- [7] H. Timmers, J.R. Leigh, M. Dasgupta, D.J. Hinde, R.C. Lemmon, J.C. Mein, C.R. Morton, J.O. Newton, and N. Rowley, Nucl. Phys. **A584**, 190 (1995).
- [8] K. Hagino and N. Rowley, Phys. Rev.C **69**, 054610(2004).
- [9] K. Hagino, N. Takigawa, and S. Kuyucak, Phys. Rev. Lett. **79**, 2943 (1997); K. Hagino, S. Kuyucak, and N. Takigawa, Phys. Rev. C **57**, 1349 (1998).
- [10] Muhammad Zamrun F. and K. Hagino, Phys. Rev. C **77**, 014606 (2008).
- [11] A. B. Balantekin and N. Takigawa, Rev. Mod. Phys. **70**, 77(1998).
- [12] J. R. Leigh, N. Rowley, R. C. Lemmon, D. J. Hinde, J. O. Newton, J. X. Wei, J. C. Mein, C. R. Morton, S. Kuyucak, and A. T. Kruppa, Phys. Rev. C **47**, R437(1993).
- [13] A. Mukherjee, D. J. Hinde, M. Dasgupta, K. Hagino, J. O. Newton, and R. D. Butt, Phys. Rev. C **75**, 044608(2007).
- [14] J.O. Newton *et al.*, Phys. Lett. **B586**, 219 (2004); Phys. Rev. C **70**, 024605 (2004).
- [15] C.L. Jiang *et al.*, Phys. Rev. Lett. **89** (2002) 052701; Phys. Rev. C **79** (2009) 044601, and references therein.

- [16] C. L. Jiang *et al.*, Phys. Rev. Lett. **97**, 012701(2004).
- [17] M. Dasgupta, D. J. Hinde, A. Diaz-Torres, B. Bouriquet, Catherine I. Low, G. J. Milburn, and J. O. Newton, Phys. Rev. Lett. **99**, 192701(2007).
- [18] A.M. Stefanini *et al.*, Phys. Rev. C **78** (2008) 044607; Phys. Lett. **B679** (2009) 95.
- [19] E. Piasecki, Ł. Świdorski, W. Gawlikowicz, J. Jastrzebski, N. Keeley, M. Kisieliński, S. Kliczewski, A. Kordyasz, M. Kowalczyk, S. Khlebnikov, E. Koshchiy, E. Kozulin, T. Krogulski, T. Loktev, M. Mutterer, K. Piasecki, A. Piórkowska, K. Rusek, A. Staudt, M. Sillanpää, S. Smirnov, I. Strojek, G. Tiourin, W. H. Trzaska, A. Trzcińska, K. Hagino, and N. Rowley, Phys. Rev. C **80**, 054613 (2009).
- [20] H. Timmers, L. Corradi, A.M. Stefanini, D. Ackermann, J.H. He, S. Beghini, G. Montagnoli, F. Scarlassara, G.F. Segato, N. Rowley, Phys. Lett. B **399**, 25 (1997).
- [21] H. Timmers, D. Ackermann, S. Beghini, L. Corradi, J. H. He, G. Montagnoli, F. Scarlassara, A. M. Stefanini, and N. Rowley, Nucl. Phys. A **633**, 421(1998).
- [22] Brookhaven National Laboratory, Evaluated Nuclear Structure Data File, <http://www.nndc.bnl.gov/ensdf/>. See references therein.
- [23] H. Timmers, Ph. D. thesis, Australian National University, 1996.
- [24] H. Timmers *et al.*, J. of Phys. G **23**, 1175 (1997).
- [25] M. Evers, M. Dasgupta, D.J. Hinde, L.R. Gasques, M.L. Brown, R. Rafiei, and R.G. Thomas, Phys. Rev. C **78**, 034614 (2008).
- [26] C.J. Lin, H.M. Jia, H.Q. Zhang, F. Yang, X.X. Xu, F. Jia, Z.H. Liu, and K. Hagino, Phys. Rev. C **79**, 064603 (2009).
- [27] M. Evers, M. Dasgupta, D. J. Hinde, D. H. Luong, R. Rafiei, and R. du. Rietz, Phys. Rev. C **84**, 054614(2011).
- [28] C. R. Morton, A. C. Berriman, M. Dasgupta, D. J. Hinde, and J. O. Newton, K. Hagino, and I. J. Thompson, Phys. Rev. C **60**, 044608(1999).
- [29] H. Esbensen and S. Misicu, Phys. Rev. C **76**, 054609 (2007).
- [30] R. Lindsay and N. Rowley, J. Phys. G **10**, 805 (1984).
- [31] M.A. Nagarajan, N. Rowley, and R. Lindsay, J. Phys. **G12**, 529 (1986).
- [32] M.A. Nagarajan, A.B. Balantekin, and N. Takigawa, Phys. Rev. C **34**, 894 (1986).

- [33] H. Esbensen, S. Landowne, and C. Price, Phys. Rev. C **36**, 1216 (1987); C **36**, 2359 (1987).
- [34] O. Tanimura, Phys. Rev. C **35**, 1600 (1987); Z. Phys. **A327**, 413 (1987).
- [35] N. Takigawa, F. Michel, A.B. Balantekin, and G. Reidemeister, Phys. Rev. C **44**, 477 (1991).
- [36] N. Takigawa, Y. Alhassid, and A. B. Balantekin, Phys. Rev. C **45**, 1850(1992).
- [37] Y. Alhassid and H. Attias, Nucl. Phys. **A577**, 709 (1994).
- [38] J. Gomez-Camacho, M.V. Andres, and M.A. Nagarajan, Nucl. Phys. **A580**, 156 (1994).
- [39] K. Hagino, N. Takigawa, A. B. Balantekin, and J. R. Bennett, Phys. Rev. C **52**, 286(1995).
- [40] N. Takigawa, K. Hagino, M. Abe, and A.B. Balantekin, Phys. Rev. C **49**, 2630 (1994).
- [41] K. Hagino, N. Rowley, A.T. Kruppa, Compt. Phys. Comm. **123**, 143 (1999).
- [42] W. T. Wagner, G. M. Crawley, G. R. Hammerstein, and H. McManus, Phys. Rev. Ca **12**, 757(1975).
- [43] M. B. Lewis, F. E. Bertrand, and C. B. Fulmer, Phys. Rev. C **7**, 1966(1973).
- [44] C.M. Ko, H. J. Pirner, and H.A. Weidenmüller, Phys. Lett. **62B**, 248(1976).
- [45] D. Agassi, H.A. Weidenmüller, and C.M. Ko, Phys. Lett. **73B**, 284(1978).
- [46] B. R. Barrett, S. Shlomo, and H.A. Weidenmüller, Phys. Rev. C **17**, 17(1978).
- [47] D. Agassi, C.M. Ko, and H.A. Weidenmüller, Ann. Phys. **107**, 140(1977).
- [48] C.M. Ko, D. Agassi, and H.A. Weidenmüller, Ann. Phys. **117**, 237(1979).
- [49] D. Agassi, C.M. Ko, and H.A. Weidenmüller, Ann. Phys. **117**, 435 (1979).
- [50] D. Agassi, C.M. Ko, and H.A. Weidenmüller, Phys. Rev. C **18**, 223(1978).
- [51] S. Yusa, K. Hagino, N. Rowley, Phys. Rev. C **85**, 054601(2012).
- [52] A. M. R. Joye, A. M. Baxter, and M. P. Fewell, Phys. Rev. Lett. **38**, 807(1977).
- [53] R. H. Spear, W. J. Vermeer, M. T. Esat, J.A. Kuehner, A. M. Baxter, and S. Hinds, Phys. Lett. B **128**, 29(1983).
- [54] B. R. Fulton and I. J. Thompson, Nucl. Phys. **A517**, 193(1990).
- [55] P. Ring and P. Schuck, *The nuclear many body problem* (Springer-Verlag, New York, 1980).

- [56] A.Bohr and B.Mottelson, *Nuclear Structure* (Benjamin, New York), Vol.1(1969).
- [57] A.Bohr and B.Mottelson, *Nuclear Structure* (Benjamin, New York), Vol.2(1975).
- [58] Minfang Yeh, P. E. Garrett, C. A. McGrath, S. W. Yates, and T. Belgia, Phys. Rev. Lett. **76**, 1208 (1996).
- [59] K. Vetter *et al.*, Phys. Rev. C **56**, 2316 (1997).
- [60] Minfang Yeh, M. Kadi, P. E. Garrett, C. A. McGrath, S. W. Yates, and T. Belgia, Phys. Rev. C **57** R2085 (1998).
- [61] K. Vetter *et al.*, Phys. Rev. C **58**, R2631 (1998).
- [62] B. D. Valnion, V. Yu. Ponomarev, Y. Eisermann, A. Gollwitzer, R. Hertenberger, A. Metz, P. Schiemenz, and G. Graw, Phys. Rev. C **63**, 024318 (2001).
- [63] M. E. Rose, *Elementary theory of angular momentum*, (Dover, 2011).
- [64] C. Y. Wong, Phys. Rev. Lett. **31**, 766(1973).
- [65] K. Hagino, N. Takigawa, and A.B. Balantekin, Phys. Rev. C **56**, 2104 (1997).
- [66] A. T. Kruppa, P. Romain, M. A. Nagarajan, and, N. Rowley, Nucl. Phys. A **560**, 845(1993).
- [67] S.G. Rohoziński and A. Sobiczewski, Acta Phys. Polonica **B12**(1981).
- [68] K. Hagino, N. Takigawa, M. Dasgupta, D. J. Hinde, and J. R. Leigh, Phys. Rev. C **55**, 276(1997).
- [69] T. Papenbrock and H. A. Weidenmüller, Rev. Mod. Phys. **79**, 997(2007).
- [70] H.A.Weidenmüller, G.E.Mitchell, Rev. Mod. Phys. **81**, 539(2009).
- [71] E. Fermi, E. Amaldi, O. D’Agostino, F. Rasetti, and E. Segre, Proc. R. Soc. Lond. A **146**, 483(1934).
- [72] E. Amaldi, O. D’Agostino, E. Fermi, B. Pontecorvo, F. Rasetti, and E. Segre, Proc. R. Soc. Lond. A **149**, 522(1935).
- [73] N.Bohr, Nature **137**, 344(1936).
- [74] C.E.Poter, *Statistical Theories of Spectra: Fluctuations*(Academic, New York)(1965).
- [75] T.Guhr, A.Muüller-Groeling, and H.A.Weidenmüller, Phys.Rep. **299**, 189(1998).
- [76] S. Mizutori and S. Åberg, Phys. Rev. E **97**, 6311(1997).

- [77] O. Bohigas, M. J. Giannoni, and C. Schmit, Phys. Rev. Lett. **52**, 1(1984).
- [78] G. Hackenbroich and H. A. Weidenmüller, Phys. Rev. Lett. **74**, 4118(1995).
- [79] C. E. Porter and N. Rosenzweig, Suomalaisen Tiedeakatemian Toimituksia A VI, No. 44(1960).
- [80] M. L. Mehta and M. Gaudin, Nucl. Phys. **18**, 420(1960).
- [81] G. Hackenbroich and H. A. Weidenmüller, Phys. Rev. Lett. **74**, 4118(1995).
- [82] T. A. Brody, J. Flores, J. B. French, P. A. Mello, A. Pandey, and S. S. M. Wong, Rev. Mod. Phys. **53**, 385(1981).
- [83] F. J. Dyson and M. L. Mehta, J. Math. Phys. **4**, 701(1963).
- [84] O. Bohigas, R. U. Haq, and A. Pandey, 1983, in *Nuclear Data for Science and Technology*, edited by K.H.Böckhoff(Reidel, Dordercht), p.809.
- [85] R. U. Haq, A. Pandey, and O. Bohigas, Phys. Rev. Lett. **48**, 1086(1982).
- [86] A. Bulgac, G. D. Dang, and D. Kusnezov, Phys. Rev. E **54**, 3468(1996).
- [87] T. Ichikawa, K. Hagino, and A. Iwamoto, Phys. Rev. Lett. **103**, 202701 (2009).
- [88] S. Yusa, K. Hagino, and N. Rowley, Phys. Rev. C **82**, 024606(2010).
- [89] O. Akyüz and A. Winther, in Proc. of the Enrico Fermi School of Physics, 1979, Course on *Nuclear Structure and Heavy-Ions Reactions*, Editors R. A. Broglia, C. H. Dasso, and R. Ricci (North Holland, Amsterdam, 1981).
- [90] S. Raman, C. W. Nestor Jr., and P. Tikkanen, At. Data Nucl. Data Tables **78**, 1 (2001).
- [91] A. J. Balts, B. F. Bayman, Phys. Rev. C **26**, 26(1982).
- [92] D. L. Hendrie, Phys. Rev. Lett. **31**, 478(1973).
- [93] S. Kalkal *et. al.*, Phys. Rev. C **81**, 044610(2010).
- [94] J. O. Newton, C. R. Morton, M. Dasgupta, J. R. Leight, J. C. Mein, D. J. Hinde, and H. Timmers, and K. Hagino, Phys. Rev. C **64**, 064608(2001).
- [95] G.H.Rawitscher, Nucl.Phys. **83**, 259(1966).
- [96] A. Bulgac, G.D. Dang, and D. Kusnezov, Ann. of Phys. **242**, 1(1995).

- [97] W. H. Press, S. A. Teukolsky, W. T. Vetterling, and B. P. Flannery, *Numerical Recipes 3rd Edition*, (Cambridge University Press, 2007).
- [98] L. D. Landau and E. M. Lifshitz, *Mechanics*(Butterworth-Heinemann, 1982).
- [99] E. Piasecki, *private communication*.